

AN INTEGRATED PICTURE OF STAR FORMATION, METALLICITY EVOLUTION, AND GALACTIC STELLAR MASS ASSEMBLY¹

L. L. COWIE², A. J. BARGER^{3,4,2}

Accepted to The Astrophysical Journal

ABSTRACT

We present an integrated study of star formation and galactic stellar mass assembly from $z = 0.05 - 1.5$ and galactic metallicity evolution from $z = 0.05 - 0.9$ using a very large and highly spectroscopically complete sample selected by rest-frame NIR bolometric flux. Our NIR (rest-frame $0.8 - 2.4 \mu\text{m}$) sample consists of 2634 galaxies with fluxes in excess of $2 \times 10^{-15} \text{ ergs cm}^{-2} \text{ s}^{-1}$ in the GOODS-N field. It probes to a complete mass limit of $10^{10} M_{\odot}$ for $z = 0.05 - 0.9$ and includes all Milky Way mass galaxies for $z = 0.05 - 1.5$. We have spectroscopic redshifts and high-quality spectra from $4500 - 10000 \text{ \AA}$ for 2020 (77%) of the galaxies. Our 13-band photometric redshift estimates show that most of the spectroscopically unidentified sources in the above redshift ranges are early-type galaxies. We assume a Salpeter IMF and fit Bruzual & Charlot (2003) models to the data to compute the galactic stellar masses and extinctions. We calibrate the star formation diagnostics internally using our $z = 0.05 - 0.475$ sample. We then derive the galactic stellar mass assembly and star formation histories. We compare our extinction corrected UV-based star formation rate densities with the combination of the star formation rate densities that we compute from the $24 \mu\text{m}$ fluxes and the extinction uncorrected [O II] luminosities. We determine the expected formed stellar mass density growth rates produced by star formation and compare them with the growth rates measured from the formed stellar mass functions by mass interval. We show that the growth rates match if the IMF is slightly increased from the Salpeter IMF at intermediate masses ($\sim 10 M_{\odot}$). We investigate the evolution of galaxy color, spectral type, and morphology with mass and redshift and the evolution of mass with environment. We find that applying extinction corrections is critical when analyzing the galaxy colors. As an example, prior to correcting for extinction, nearly all of the galaxies in the green valley are $24 \mu\text{m}$ sources, but after correcting for extinction, the bulk of the $24 \mu\text{m}$ sources lie in the blue cloud. We also compute the metallicities of the sources between $z = 0.05 - 0.9$ that have well-detected H β , [O II] $\lambda 3727$, and [O III] $\lambda 5007$ emission lines using the R23 diagnostic ratio. At $z < 0.475$ we use the R23, [N II]/[O II], and [N II]/H α diagnostic ratios. We find an evolution of the metallicity-mass relation corresponding to a decrease of 0.21 ± 0.03 dex between the local value and the value at $z = 0.77$ in the $10^{10} - 10^{11} M_{\odot}$ range. We use the metallicity evolution to estimate the gas mass of the galaxies, which we compare with the galactic stellar mass assembly and star formation histories. Overall, our measurements are consistent with a galaxy evolution process dominated by episodic bursts of star formation and where star formation in the most massive galaxies ($\gtrsim 10^{11} M_{\odot}$) ceases at $z < 1.5$ because of gas starvation.

Subject headings: cosmology: observations — galaxies: distances and redshifts — galaxies: active — X-rays: galaxies — galaxies: formation — galaxies: evolution

1. INTRODUCTION

One of the fundamental goals of modern cosmology is to understand the formation and evolution of the galaxy population as a whole. We shall refer to this as the cosmic galaxy formation problem. There has been spectacular progress in addressing the cosmic galaxy formation problem over the last twenty years, beginning with the determination of the star formation history (e.g., Cowie et al. 1995; Lilly et al. 1996; Madau et al. 1996; Steidel et al. 1999; Haarsma et al. 2000; Barger et al. 2000; Le Floch et al. 2005; Pérez-González et al. 2005; Hopkins & Beacom 2006; Wang et al. 2006; Reddy et al. 2008). This has been followed more recently by efforts to measure the galactic stellar mass assembly history (e.g., Brinchmann &

Ellis 2000; Cole et al. 2001; Bell et al. 2003, 2007; Pérez-González et al. 2003, 2008; Dickinson et al. 2003; Rudnick et al. 2003, 2006; Fontana et al. 2003, 2004, 2006; Drory et al. 2004, 2005; Bundy et al. 2005, 2006; Conselice et al. 2005, 2007; Borch et al. 2006; Pannella et al. 2006; Elsner et al. 2008) and the evolution of metallicity with galaxy mass and redshift (e.g., Kobulnicky et al. 2003; Lilly et al. 2003; Kobulnicky & Kewley 2004; Tremonti et al. 2004; Liang et al. 2004; Savaglio et al. 2005). However, ideally what one wants is a comprehensive analysis of the history of star formation, the growth of galactic stellar mass and metals content, and the changes in morphology with redshift, galaxy mass, and the environment for a large, mass-selected galaxy sample that could be compared in

¹Based in part on data obtained at the W. M. Keck Observatory, which is operated as a scientific partnership among the California Institute of Technology, the University of California, and NASA and was made possible by the generous financial support of the W. M. Keck Foundation.

²Institute for Astronomy, University of Hawaii, 2680 Woodlawn Drive, Honolulu, HI 96822.

³Department of Astronomy, University of Wisconsin-Madison, 475 North Charter Street, Madison, WI 53706.

⁴Department of Physics and Astronomy, University of Hawaii, 2505 Correa Road, Honolulu, HI 96822.

detail with local galaxy properties and cosmological simulations of galaxy evolution. In particular, such an analysis could yield clear explanations for the migration of star formation to lower mass galaxies at later cosmic times and the simultaneous quenching of star formation in the most massive galaxies (the downsizing of Cowie et al. 1996), as well as for the color bimodality of galaxy populations (e.g., Strateva et al. 2001; Baldry et al. 2004).

Up until now such an analysis has not been possible since existing data sets are either visually selected, have limited color information, and are poorly suited to a metals analysis because of the spectroscopic wavelength coverage (e.g., the DEEP2 survey); mass selected but based on photometric redshifts (e.g., Combo17/GEMS); or mass selected and spectroscopically observed but based on a relatively small sample (e.g., the Gemini Deep Deep Survey).

In this paper we present, for the first time, an integrated, mass-based analysis made possible by the availability of a large, homogeneous, near-infrared (NIR) selected and spectroscopically observed galaxy sample in the Great Observatories Origins Deep Survey-North (GOODS-N; Giavalisco et al. 2004) field. We have obtained extremely deep, wide-field NIR images (Keenan et al. 2008, in preparation) and highly complete spectroscopic identifications of the sources in this field (Barger et al. 2008, in preparation). We are therefore able to use, for the most part, spectroscopic redshifts to make our determinations of the galactic stellar mass assembly and star formation histories, as well as high-quality measurements of line fluxes to obtain the metallicity history.

However, we caution that even with such an excellent data set there are many complicating factors in relating the star formation history to the stellar mass assembly history and the formation of metals in galaxies, even at late cosmic times. (Here we shall take late cosmic times to be $z < 1.5$.) At the conceptual level, methods of measuring star formation rates use diagnostics which are sensitive to the high-mass end of the stellar initial mass function (IMF), while stellar mass measurements are dominated by lower mass stars. Therefore, while the shape of the sub-solar IMF only enters as a normalization factor, the shape of the IMF at higher masses is critical in relating the star formation rates to the stellar masses. Thus, we must be concerned about the uncertainties in the IMF shape and the potential variations in the IMF shape between different types of galaxies. In principle we could minimize this problem by considering the growth of the stellar mass in metals rather than the growth of the total stellar mass, since the metals are produced by the same high-mass stars that are measured by the star formation diagnostics (Cowie 1988). However, even this is subject to uncertainties in the yields and would require the measurement of not only the total stellar mass evolution but also the metals evolution in both stars and gas, which would be very challenging to do.

Measurements of the star formation rates, stellar masses, and metals are also complicated by other factors. Extinction reradiates light from the rest-frame UV to the far-infrared (FIR), and we must determine total star formation rates over a wide range of galaxies with radically different morphologies and dust column densities. Conversions even of NIR light to stellar mass are complicated by ongoing active star formation, and there are still major uncertainties in the stellar modeling of the galaxy popu-

lations. Finally, determinations of the metals throughout the redshift range of interest can only be made for the gaseous baryons in the star-forming galaxies and depend on the notoriously uncertain conversions of the strong oxygen and nitrogen emission lines to metallicities.

Cosmic variance is also a significant issue in a field size as small as the GOODS-N (e.g. Somerville et al. 2004) and can affect our analysis of the evolution of quantities such as the galaxy mass density and the universal star formation rates.

These problems must be borne in mind throughout any work of the present type, and we attempt at all points to work forward as self-consistently as possible from the raw information (NIR luminosities, galaxy line strengths, raw star formation diagnostics, etc.) to inferences about the evolution of derived quantities, such as stellar masses, star formation rates, and metallicities. Also, wherever possible, we have used multiple independent methods to determine the sensitivity of the derived quantities to our underlying assumptions. We attempt to self consistently estimate the effects of cosmic variance within the data set and also to estimate the effects which analytic error estimates of the variance could introduce in our analysis. Finally we compare our results throughout to other recent work using different, and in some cases much larger, fields to check for consistency in these portions of the paper.

The outline of the paper is as follows. In §2 and §3 we describe the basic data and the sample selections. In §4 we fit Bruzual & Charlot (2003) models to the data to determine galactic stellar masses and extinctions in the galaxies. In §5 we measure equivalent widths and line fluxes from the spectra. In §6 we compare measurements of the continuum and line extinctions. In §7 we derive self-consistent calibrations of the various star formation rate diagnostics. In §8 and §9 we derive the metallicities with mass and redshift using various metallicity diagnostics. In §10 we consider the galaxies missing from the metals analysis. This is a long paper, and some readers may wish to skip much of the detail and move to the discussion (§11) and summary (§12), which we have tried to make separately readable and which contain the high-level interpretation of the data, including the derivation of the stellar mass assembly history with redshift, the evolution of the mass-metallicity and mass-morphology relations with redshift and environment, and the use of the metals evolution to derive an estimate of the baryonic gas mass reservoir in the galaxies. We find that all of our measurements provide a broad, self-consistent picture of a galaxy evolution process dominated by episodic bursts of star formation and where star formation in the most massive galaxies is terminated at later cosmic times as a consequence of gas starvation.

We adopt the -1.35 power-law Salpeter IMF (Salpeter 1955) extending from 0.1 to 100 M_{\odot} for ease of comparison with previous results. Most importantly, this allows us to compare directly with the local mass function computed by Cole et al. (2001; hereafter, Cole01) for this IMF. The Salpeter IMF only differs significantly from the current best IMFs (Kroupa 2001; Chabrier 2003) below 1 M_{\odot} , and thus these three IMFs differ only in the normalization of the galactic stellar mass and star formation rate determinations. We can convert the total mass formed into stars prior to stellar mass loss (which we will refer to as

the formed stellar mass to distinguish it from the present stellar mass, which is the stellar mass present at any given time) from the Salpeter IMF to the Chabrier IMF by dividing by 1.39 and to the Kroupa IMF by dividing by 1.31. The exact conversion when considering the present stellar masses rather than the formed stellar masses depends on the average evolutionary stage of the galaxies. However, this dependence is relatively weak, and we may approximately convert the present stellar mass from the Salpeter IMF to the Chabrier IMF by dividing by 1.70 and to the Kroupa IMF by dividing by 1.54. Note that these latter conversion factors have been computed for the distribution of ages in our ensemble of galaxies. The present stellar mass for the Salpeter IMF is roughly 0.74 of the formed stellar mass.

We assume $\Omega_M = 0.3$, $\Omega_\Lambda = 0.7$, and $H_0 = 70 \text{ km s}^{-1} \text{ Mpc}^{-1}$ throughout. All magnitudes are given in the AB magnitude system, where an AB magnitude is defined by $m_{AB} = -2.5 \log f_\nu - 48.60$. Here f_ν is the flux of the source in units of $\text{ergs cm}^{-2} \text{ s}^{-1} \text{ Hz}^{-1}$. We assume a reference value of the solar metallicity of $12 + \log(\text{O}/\text{H}) = 8.66$ and a conversion to the mass fraction of metals of $Z = 0.0126$ (Asplund et al. 2004). This conversion is weakly dependent on the assumed chemical composition relative to the oxygen abundance.

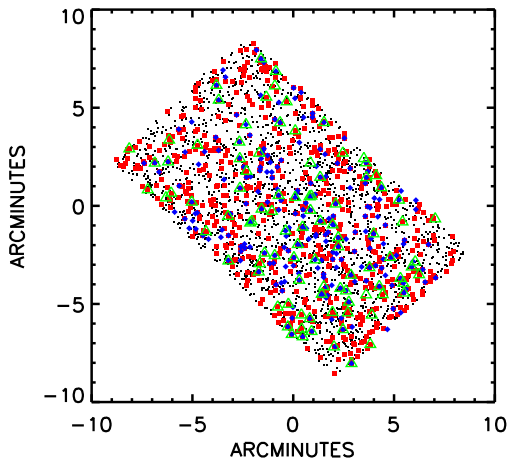


FIG. 1.— The observed area in the GOODS-N. The area is centered on RA(2000) and Dec(2000) coordinates (189.2282, 62.2375) with corners at (189.5435, 62.2749), (188.9137, 62.2000), (189.3090, 62.3824), and (189.1482, 62.0909). The covered area is 145 arcmin^2 ($9'.3$ by $15'.7$). The NIR-selected sample is shown with black dots, the 663 $24 \mu\text{m}$ detected sources with red squares, the 229 X-ray detected sources with blue diamonds, and the 97 20 cm detected sources with green open triangles. The concentration of the X-ray sources to the field center reflects the variation in the sensitivity of the X-ray image over the field.

2. THE NIR BOLOMETRIC FLUX SAMPLE

2.1. Photometric Selection

The GOODS-N field is one of the most intensively studied regions in the sky, and in many bandpasses it has the deepest images ever obtained. Thus, it is nearly ideal for the present study. In this paper we use photometric data taken from existing work. The optical magnitudes are from the Subaru 8.2 m SuprimeCam observations of Capak et al. (2004; U, B, V, R, I, z') and from the *HST* Advanced Camera for Surveys (ACS) observations of Giavalisco et al. (2004; F435W, F606W, F775W, and

F850LP). The NIR magnitudes are from the University of Hawaii 2.2 m ULBCAM (J, H) and CFHT WIRCAM and Subaru 8.2 m MOIRCS (K_s) observations of Keenan et al. (2008, in preparation). To properly match to the optical data, the $3.6, 4.5, 5.8,$ and $8.0 \mu\text{m}$ magnitudes were measured directly from the IRAC images that Wang et al. (2006) produced. Weighting by exposure time, Wang et al. (2006) combined the reduced DR1 and DR2 IRAC superdeep images from the *Spitzer* Legacy first, interim, and second data release products (DR1, DR1+, DR2; Dickinson et al. 2008, in preparation). In all cases, only sources within the well-covered ACS GOODS-N region were included, as summarized in Figure 1. The covered area is 145 arcmin^2 .

For all of the sources we used corrected aperture magnitudes to compute the colors and spectral energy distributions (SEDs). We used $3''$ diameter apertures for the optical and NIR data and $6''$ diameter apertures for the MIR data. We computed the median of the difference between these magnitudes and aperture magnitudes computed in $6''$ diameter apertures for the the optical and $12''$ diameter apertures for the MIR data and used this median to correct the smaller aperture magnitude to an approximate total magnitude. For the brighter extended sources we also computed isophotal magnitudes integrated to 0.01% of the peak surface brightness and used the difference between these and the corrected aperture magnitudes in the K_s band to correct the luminosities and masses. All of the calibrations are independent, so it is important to check that we have fully consistent magnitudes. We will return to this point in §5.1.

We computed a rest-frame NIR bolometric flux for all of the sources in the region which were significantly detected at any of the observed wavelength bands by linearly interpolating the observed magnitudes to form a rest frame SED. We used spectroscopic redshifts, where these were known, or otherwise photometric redshifts, which we calculated as in Wang et al. (2006) using the template method developed by Pérez-González et al. (2005). We computed the flux over the *rest-frame* wavelength range 8000 \AA to $2.4 \mu\text{m}$. We excluded from the sample the spectroscopically identified stars and all of the sources within $3''$ of a brighter object or within $12''$ of the eleven brightest stars, leaving a final sample of 2634 galaxies with fluxes above $2 \times 10^{-15} \text{ ergs cm}^{-2} \text{ s}^{-1}$. We take this as our primary NIR sample. Our exclusion of neighbor sources introduces a small, flux-dependent correction to the area, which we allow for in our determinations of the mass functions, but the correction never exceeds 10%, even at the faintest fluxes.

Our selection by rest frame NIR bolometric flux is compared with the more usual selection by observed NIR magnitude ($K_{s,AB}$) in Figure 2 for sources with $z = 0.05 - 1.5$. The best-fit relation gives

$$K_{s,AB} = -11.87 - 2.40 \log(\text{NIR flux}), \quad (1)$$

and the limiting NIR flux corresponds roughly to $K_{s,AB} = 23.4$. This is a shallow sample compared to the depth of the NIR images. For the K_s image it corresponds to an 18σ selection. Thus, there should be no significant selection biases.

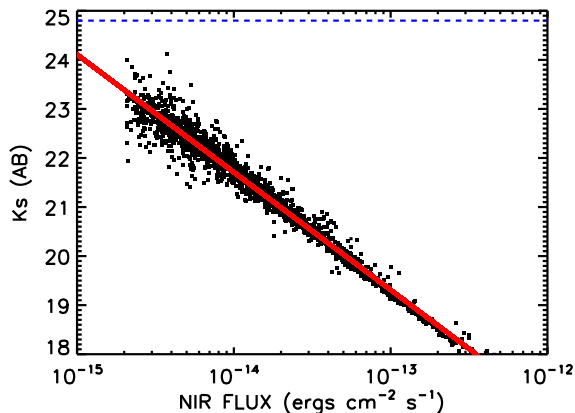


FIG. 2.— Comparison of the rest-frame NIR bolometric flux with the observed K_s magnitude for sources with $z = 0.05 - 1.5$. The red diagonal line shows the least-square polynomial fit of $\log(\text{NIR flux})$ to K_s magnitude. The blue dashed horizontal line shows the 5σ flux limit of 24.8 for the K_s sample.

We identified X-ray counterparts to the NIR sample by matching our sample to the sources detected in the Alexander et al. (2003) catalog of the 2 Ms *Chandra* Deep Field-North (CDF-N) using a $2''$ search radius. Near the aim point the CDF-N X-ray data reach limiting fluxes of $\approx 1.5 \times 10^{-17}$ (0.5–2 keV) and $\approx 1.4 \times 10^{-16}$ ergs $\text{cm}^{-2} \text{s}^{-1}$ (2–8 keV). We similarly obtained the radio fluxes from the Richards (2000) 1.4 GHz catalog, which reaches a 5σ limiting flux of 40 μJy and the 24 μm fluxes are from the DR1+ MIPS 24 μm source list and version 0.36 MIPS 24 μm map provided by the *Spitzer* Legacy Program. This source catalog is flux-limited at 80 μJy and is a subset of a more extensive catalog (R. R. Chary et al. 2007, in preparation).

Our NIR-selected sample, together with the X-ray, 20 cm, and 24 μm detected sources, are shown in Figure 1.

2.2. Spectroscopy

Following the establishment of the Hubble Deep Field-North (HDF-N) with *HST*, intensive spectroscopic observations of the region were made by a number of groups, primarily using the Low-Resolution Imaging Spectrograph (LRIS; Oke et al. 1995) on the Keck I 10 m telescope (these data are summarized in Cohen et al. 2000). After the more extended GOODS-N region was observed with the ACS camera, a number of groups began intensive spectroscopic observations with the large-format Deep Extragalactic Imaging Multi-Object Spectrograph (DEIMOS; Faber et al. 2003) on the Keck II 10 m telescope. Wirth et al. (2004; Keck Team Redshift Survey or KTRS) and Cowie et al. (2004) presented large samples of magnitude-selected redshifts, while Reddy et al. (2006) gave a substantial sample of $z = 2 - 3$ color-selected redshifts, Chapman et al. (2004, 2005) and Swinbank et al. (2004) presented a number of radio/submillimeter redshifts, Treu et al. (2005) measured redshifts for a sample of spheroids, and Barger et al. (2005, 2007) carried out observations on the X-ray and 1.4 GHz samples.

We have attempted to make the most complete and homogeneous spectral database possible by observing all of the missing or unidentified galaxies in a variety of flux-limited samples. A more extensive description of these

samples may be found in Barger et al. (2007, in preparation). In this paper we focus only on the spectroscopic observations of our NIR sample. Our observations were made in a number of DEIMOS runs between 2004 and 2007. We used the 600 lines per mm grating, giving a resolution of 3.5 \AA and a wavelength coverage of 5300 \AA , which was the configuration used in the KTRS and in the Cowie et al. (2004) observations. The spectra were centered at an average wavelength of 7200 \AA , though the exact wavelength range for each spectrum depends on the slit position. Each ~ 1 hr exposure was broken into three subsets, with the objects stepped along the slit by $1.5''$ in each direction. Unidentified objects were continuously reobserved, giving maximum exposure times of up to 7 hrs. The spectra were reduced in the same way as previous LRIS spectra (Cowie et al. 1996). The dithering procedure provides extremely high-precision sky subtraction, which is important if we wish to measure accurate equivalent widths, as in the present paper. We have only included spectra in the sample that could be confidently identified based on multiple emission and/or absorption lines.

We also reobserved objects where the original spectra were of poor quality or where previous redshifts were obtained with instruments other than DEIMOS, as well as where the existing redshift identifications were unconvincing or where there were conflicting redshifts in the literature (a small number of sources). Many of the KTRS spectra have poor sky subtraction. While these spectra are adequate for redshift identifications, they are not suitable for line measurements because of the residual sky lines. For the fainter objects the absolute sky subtraction is often problematic and, in some cases, the spectra even have negative continua. Equivalent width measurements made on such spectra have very large systematic uncertainties. This is a substantial problem for previous work (e.g., Kobulnicky & Kewley 2004) that relied on the KTRS spectra. We have reobserved most of these sources.

We now have spectroscopic redshift identifications for 2020 of the 2634 galaxies (77%) in our NIR sample. We show the redshift distribution for the spectroscopically identified sample in Figure 3 (*black histogram*). The photometric redshift analysis of the remaining sources (*red histogram*) implies that most of these sources lie outside of our redshift ranges of interest ($z = 0.05 - 0.9$ for our metallicity analysis and $z = 0.05 - 1.5$ for our mass assembly and star formation analyses) and hence that the spectroscopic completeness inside our two redshift ranges of interest is extremely high.

We assigned photometric redshifts to all but 14 of the sources in our sample. These 14 sources are either extremely faint or have peculiar SEDs that could not be adequately fitted by the templates. We shall assume that these lie outside of our redshift ranges of interest. Between $z = 0$ and $z = 0.9$ there are 1260 spectroscopically identified sources, and between $z = 0$ and $z = 1.5$ there are 1884 spectroscopically identified sources. Photometric redshifts add a further 126 sources to $z = 0.05 - 0.9$ and a further 229 sources to $z = 0.9 - 1.5$. Based on the SEDs of the sources with only photometric redshifts in these ranges, many are red galaxies, which are more difficult to identify spectroscopically. Of the bluer sources, some may have photometric redshifts that have scattered

into these redshift ranges, even though their true redshifts are higher. Of the 126 galaxies with only photometric redshifts in the redshift range $z = 0.05 - 0.9$, 87 have been spectroscopically observed and none of these have strong emission lines. Emission lines, if present, would have easily been observed in this redshift range.

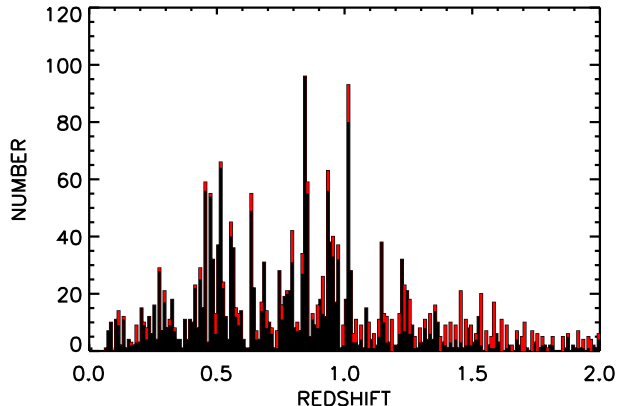


FIG. 3.— Redshift distribution of our full NIR sample. Black (red) histogram shows spectroscopic (photometric) redshifts. The redshift bin size is 0.01.

We conclude that the spectroscopic sample contains nearly all of the sources (1260 out of a maximum of 1386, or $> 91\%$) lying in the redshift range $z = 0.05 - 0.9$ and essentially all of the sources with strong emission lines suitable for measuring emission line metallicities in this redshift range. Over the $z = 0.05 - 1.5$ interval the spectroscopically identified sample contains $> 84\%$ of the galaxies (1884 out of a maximum of 2239).

2.3. Galaxy Morphologies

The galaxy morphological types are taken from Bundy et al. (2005) wherever possible. The Bundy et al. catalog is based on Richard Ellis’s visual classification of the sources in the GOODS-N according to the following scale: $-2 = \text{Star}$, $-1 = \text{Compact}$, $0 = \text{E}$, $1 = \text{E/S0}$, $2 = \text{S0}$, $3 = \text{Sab}$, $4 = \text{S}$, $5 = \text{Scd}$, $6 = \text{Irr}$, $7 = \text{Unclass}$, $8 = \text{Merger}$, and $9 = \text{Fault}$. For galaxies in our sample which were not included in the Bundy et al. (2005) catalog, we visually classified the sources using the *HST* F850LP images, aiming to reproduce the Ellis classifications as closely as possible.

2.4. Galaxy Environments

The local galaxy density can be computed using the distance to the n th nearest neighbor (Dressler 1980). In the present work we use the velocity information only to separate slices; otherwise we use the projected distance d_n . The surface density is then given by $\Sigma = n/(\pi d_n^2)$. An extensive comparison of this measure of the density environment with other methods is given in Cooper et al. (2005), who conclude that the projected distance method is generally the most robust for this type of work.

Edge effects are important in small field areas, such as the GOODS-N region, and can bias the density parameter in low density regions where the projected separation extends beyond the edge of the field. We correct for this effect by including only that part of the area πd_n^2 which

lies within the field (e.g., Baldry et al. 2006). To further reduce the edge effects, we use a low n to minimize the projected distance and also exclude regions of the field that, at the redshift of the galaxy, lie too close to the edge of the field for an accurate measurement.

Thus, for each galaxy we computed the projected density based on the 3rd nearest neighbor having a mass above a uniform mass cut and lying within 1000 km s^{-1} of the galaxy. We exclude galaxies which lie closer than 1 Mpc from the sample edge. This constraint restricts to galaxies with $z \gtrsim 0.3$, since all of the lower redshift galaxies will lie too close to the edges of the field.

3. FOUR UNIFORM NIR LUMINOSITY SAMPLES

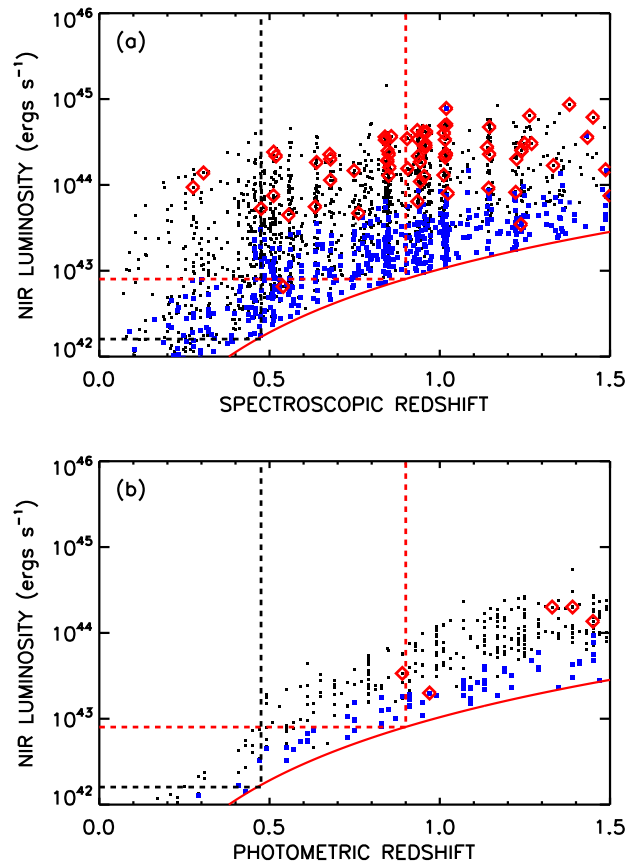


FIG. 4.— (a) NIR luminosity vs. spectroscopic redshift for the spectroscopically identified sources in the NIR sample, and (b) NIR luminosity vs. photometric redshift for the spectroscopically unidentified sources in the NIR sample. The blue solid squares show sources with blue spectra, where massive stars may still make a substantial contribution to the NIR luminosity. The red open diamonds show sources containing AGNs based on their X-ray luminosities. The red solid curve shows the luminosity corresponding to the limiting NIR flux of $2 \times 10^{-15} \text{ ergs cm}^{-2} \text{ s}^{-1}$. The red (black) dashed lines mark the region that corresponds to the mid- z (low- z) uniform NIR luminosity sample, where the [O III] $\lambda 5007$ ($H\alpha$) line would be in the spectrum.

In Figure 4a (4b) we show NIR luminosity versus spectroscopic (photometric) redshift for the spectroscopically identified (unidentified) NIR sample. We denote sources with blue spectra, where massive stars may still make a substantial contribution to the NIR luminosity, by blue solid squares. We denote sources that contain AGNs (based on whether either their $2 - 8 \text{ keV}$ or $0.5 - 2 \text{ keV}$

luminosities are $> 10^{42}$ ergs s^{-1}) by red open diamonds. We show the luminosity corresponding to the limiting NIR flux of 2×10^{-15} ergs $cm^{-2} s^{-1}$ by the solid red curve.

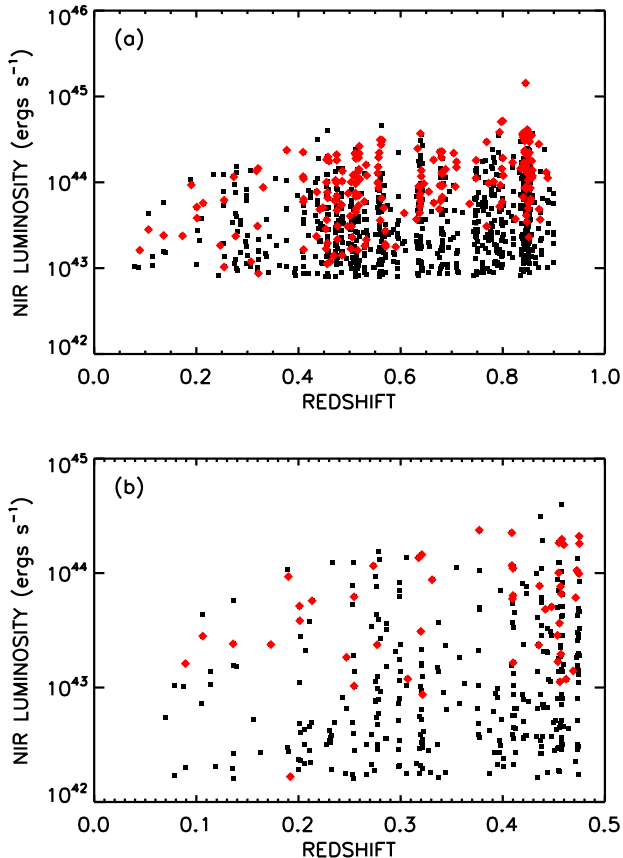


FIG. 5.— NIR luminosity vs. redshift for the spectroscopically identified sources in the (a) mid- z sample and (b) low- z sample. The sources with emission (absorption) line redshifts are denoted by black squares (red diamonds).

We construct two uniform NIR luminosity samples for our metallicity analysis: a mid- z sample and a low- z sample. Although most of the spectra extend to about $1 \mu m$, the sensitivity falls rapidly at the reddest wavelengths, and some spectra are cut off at wavelengths $< 1 \mu m$ because of their mask positions. Thus, we choose a limiting upper wavelength of 9500 \AA . The limiting upper wavelength of 9500 \AA corresponds to $z < 0.9$ ($z < 0.475$) for the $[O III] \lambda 5007 \text{ \AA}$ ($H\alpha$) line to be observable if present. In each case this sets a lower limit on the NIR luminosity, which corresponds to the NIR flux limit at the maximum redshift. The mid- z sample has $z = 0.05 - 0.9$ and NIR luminosity $> 8 \times 10^{42}$ ergs s^{-1} , and the low- z sample has $z = 0.05 - 0.475$ and NIR luminosity $> 1.6 \times 10^{42}$ ergs s^{-1} . These limits are shown in Figure 4 by the red (black) dashed lines for the mid- z (low- z) sample. The low-redshift portion of the mid- z sample is contained as the high-mass subset of the low- z sample.

There are 1009 sources in the mid- z sample, of which 929 (92%) have spectroscopic redshifts. There are 378 sources in the low- z sample, of which 354 (96%) have spectroscopic redshifts. In Figures 5a and 5b we show blow-ups of Figures 4a and 4b to more clearly illustrate both samples, but here our symbols distinguish between absorption line

redshifts (*red diamonds*) and emission line redshifts (*black squares*). Of the 929 (354) spectroscopically identified redshifts in the mid- z (low- z) sample, 210 (49) are based on absorption line features. The absorbers comprise a much higher fraction of the more luminous galaxies. Thus, the smaller fraction of absorbers in the low- z sample is partly a consequence of the lower luminosity limit in that sample.

We also construct two higher-redshift uniform NIR luminosity samples for studying the evolution of the galaxy masses and star formation histories. We will refer to these as our high- z and highest- z samples. The high- z sample has $z = 0.9 - 1.2$ and NIR luminosity $> 2 \times 10^{43}$ ergs s^{-1} . The highest- z sample has $z = 1.2 - 1.5$ and NIR luminosity $> 3 \times 10^{43}$ ergs s^{-1} .

4. FITTING THE GALAXY SPECTRAL ENERGY DISTRIBUTIONS

While NIR luminosities have been the preferred way to estimate galaxy mass, there is still a wide range in the mass to NIR luminosity ratios and there are still considerable uncertainties in the models used to determine the masses. The mass ratio for a galaxy depends on its star formation history and on the level of extinction (Brinchmann & Ellis 2000). We may estimate the conversion from NIR luminosity to mass by fitting the galaxy SEDs with model galaxy types modulated by an assumed extinction law (e.g., Brinchmann & Ellis 2000; Kauffmann et al. 2003a; Bundy et al. 2005). We follow this procedure here to estimate the masses of the galaxies and the extinctions. We use the Bruzual & Charlot (2003; hereafter, BC03) models for ease of comparison with previous work; however, as we will discuss, there has been considerable recent debate over this calibration, which may overestimate galaxy mass.

For every galaxy in each of our four uniform NIR luminosity samples, we fitted BC03 models assuming a Salpeter IMF, a solar metallicity, and a Calzetti extinction law (Calzetti et al. 2000). We included a range of types from single burst models to exponentially declining models to constant star formation models. For each galaxy we varied the age from 5×10^7 yr to the maximum possible age of the galaxy at its redshift. In making the fits, we calculated the χ^2 values assuming an individual error of 0.1 mag in each band together with the 1σ noise in each band, and we fitted the SED over the rest-frame wavelength range $0.2 - 2.4 \mu m$.

Our use of only solar metallicity models does not introduce significant uncertainties in the inferred masses and extinctions. As we shall discuss later there is a well-known strong degeneracy between age and metallicity in the stellar models. Introducing a range in metallicity in the models therefore increases the spread in the possible ages while leaving the other quantities nearly unchanged. We have re-computed the results of the present paper using supersolar and subsolar models and find this does not change any of the conclusions.

In our subsequent analysis we use the mass ratios and extinctions corresponding to the minimum χ^2 fits. Hereafter, we refer to these best fits as our BC03 fits and the corresponding masses and extinctions as our BC03 masses and extinctions. However, we note that the mass to NIR luminosity ratio and extinction probability distributions (see Kauffmann et al. 2003a) show that there are still sub-

stantial uncertainties in these quantities (e.g., Papovich et al. 2006). These uncertainties are the largest for the blue galaxies and can range up to 0.3 dex in the mass to NIR luminosity ratio. This reflects the ambiguities in the type and extinction fitting, where models with different star formation histories and extinctions can reproduce the same galaxy SED.

In Figure 6 we show our BC03 fits to two example galaxies. In (a) we show a red galaxy at $z = 0.850$ which is best fitted by no extinction (*black squares*) and a single burst with an age of 2.4 Gyr (*red SED*). In (b) we show a red galaxy at $z = 0.433$ which is best fitted with a large extinction of $E(B - V) = 0.45$ (*black squares*) and a single burst with an age of 0.18 Gyr (*red SED*). However, as an example of how our distinction between old galaxies and reddened younger galaxies relies on the overall shape of the SED, we also show in (b) a fit with no extinction (*purple diamonds*) and a 1 Gyr exponential decline with an age of 4.5 Gyr (*purple SED*). It would not be possible to differentiate between these two fits with only the optical data; however, with the NIR data the latter is a significantly poorer fit. For all the fits shown the solid portions of the curves indicate the regions over which we made the fits. We did not fit to the rest-frame MIR data because of the limitations of the BC03 models at the longer wavelengths.

However, there are very serious concerns about determining the stellar masses from the population synthesis models and, in particular, from the NIR fluxes. Maraston (2005) pointed out that an improved treatment of the thermally-pulsating asymptotic giant branch (TP-AGB) stars resulted in a substantial increase in the NIR light at intermediate ($\sim 10^9$ yr) ages relative to preceding population synthesis models. This would reduce the stellar mass estimates in the high-redshift galaxies. Bruzual (2007) reports similar results when an improved treatment of the TP-AGB stars is included in a revised version of the Bruzual-Charlot code. Kannappan & Gawiser (2007) have investigated the differences in the various models using a local galaxy sample and, while not coming to a conclusion about a preferred model, they emphasize the uncertainties in the mass determination as a function of galaxy type.

Conselice et al. (2007; hereafter, Conselice07) have used fits to the revised Bruzual-Charlot models to argue that the decrease in the average masses relative to BC03 is small for galaxies in the $z = 0.4 - 2$ redshift range when the masses are based on rest-frame $0.7 - 1.5 \mu\text{m}$ wavelengths. They find an average drop in the masses of 0.08 dex relative to BC03 and a maximum decrease of about 20%. However, averaging may obscure the systematic effects of the uncertainties, particularly when comparing the higher redshift samples with local samples. For example, galaxies with ages of 10^{10} yr will have BC03 masses that are consistent with the Maraston (2005) and revised Bruzual-Charlot codes, while those with ages of 10^9 yr will have BC03 masses that are about 25% too high, and those with ages of $10^8 - 10^9$ yr will have BC03 masses that are about 40% too high (see Fig. 3 of Bruzual 2007). We will consider the possible effects of such systematic uncertainties on the stellar mass density growth rates measured from the formed stellar mass functions and the comparison of those rates with the expected formed stellar mass density growth rates produced by star formation in §11.3.

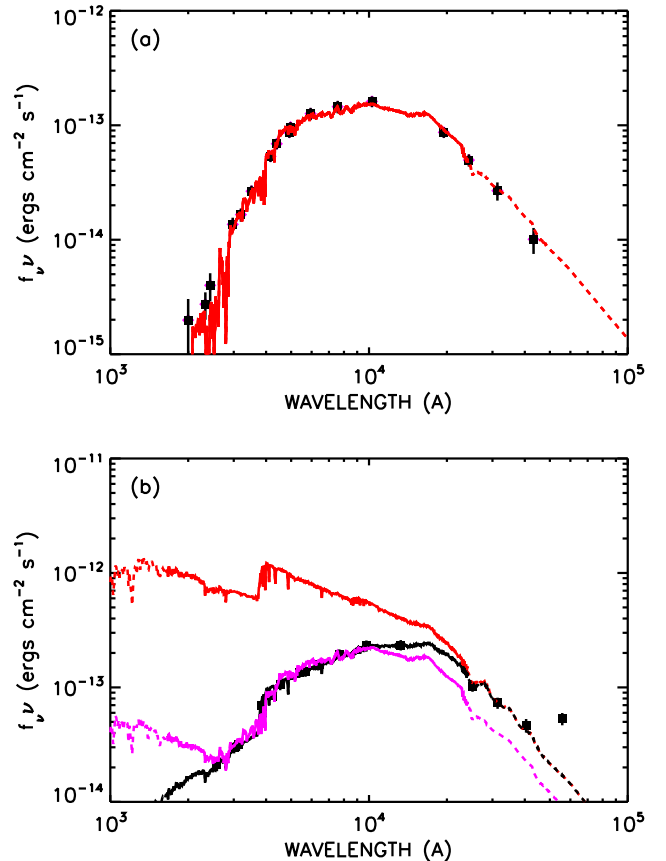


FIG. 6.— Sample BC03 fits to two galaxies. (a) A red galaxy at $z = 0.850$ is best fitted with no extinction (*black squares with the assumed errors from the text*) and a single burst with an age of 2.4 Gyr (*red SED*). The solid portion of the curve shows the region over which we made the fit. (b) A red galaxy at $z = 0.433$ is best fitted with a large extinction of $E(B - V) = 0.45$ (*black squares with the assumed errors from the text show the observed fluxes*) and a single burst with an age of 0.18 Gyr (*the red solid line shows the galaxy SED without extinction and the black line the SED with the extinction included*). The NIR data are required to distinguish between this best-fit extinguished model and another fit having no extinction (*purple diamonds with the assumed errors from the text*) and a 1 Gyr exponential decline with an age of 4.5 Gyr (*purple SED*). The solid portion of each curve shows the region over which we made the fit. Both are good fits to the rest frame optical and UV but the model with no extinction is a significantly poorer fit in the near IR. The no-extinction fit would reduce the mass by a factor of five relative to the and the inferred star-formation rate by a factor of thirty relative to the best fit model.

4.1. Extinctions

Given the model uncertainties discussed above, it is critical to determine how meaningful our BC03 extinctions are. We may test them in two ways. First we look at how they relate to the MIR properties of the galaxies, and then we compare them with extinctions measured from the Balmer lines. We note that the comparison of our BC03 extinctions with the MIR properties is affected by orientation, which will add scatter to the comparison. However, for both of our tests we find reasonable agreement between our BC03 extinctions and the dust properties measured in other ways.

In Figure 7 we show the distribution of the BC03 extinctions for the mid- z sample (*black histogram*). We find

that roughly half of the galaxies in the sample have weak extinctions of $E(B - V) < 0.1$ or no measured extinction, while the remainder lie in an extended tail up to our maximum allowed value of $E(B - V) = 0.63$. The median extinction of $A_v = 0.6$ is twice the local value given by Kauffmann et al. (2003a). This is consistent with the high-redshift galaxies having more gas and dust mass. We shall return to this point in §11.10.

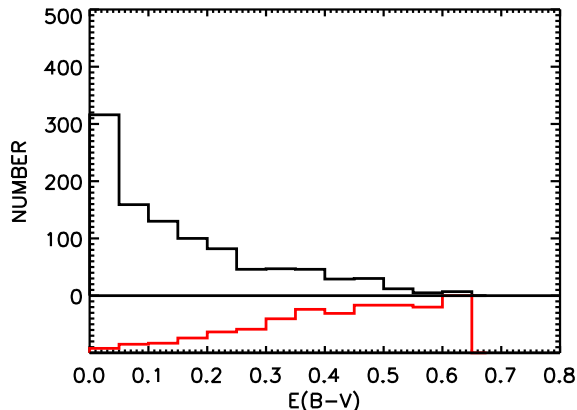


FIG. 7.— Distribution of extinctions for the mid- z sample derived from our BC03 fits (*black histogram*). Roughly half of the galaxies have little or no extinction. The red histogram shown underneath is the fraction of galaxies detected at $24 \mu\text{m}$. Only about 11% of the galaxies with weak extinctions of $E(B - V) < 0.05$ are $24 \mu\text{m}$ sources, while nearly all of the strongly extinguished sources are.

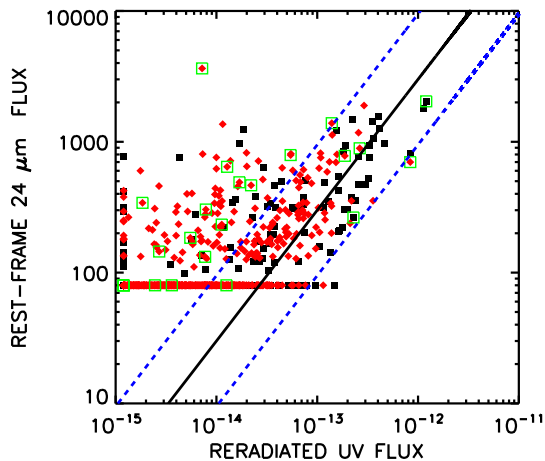


FIG. 8.— Comparison of the reradiated light that originated from rest-frame $2000 - 3000 \text{ \AA}$ (see text for details) with the rest-frame $24 \mu\text{m}$ flux for the mid- z sample. The $24 \mu\text{m}$ K -correction has been computed assuming the M82 SED of Silva et al. (1998). The red diamonds show sources with $z = 0.475 - 0.9$, and the black squares show lower redshift sources. The galaxies without $24 \mu\text{m}$ detections are shown at the $80 \mu\text{Jy}$ limit of the $24 \mu\text{m}$ data, and the galaxies with little or no reradiated flux are shown at a nominal value of $1.2 \times 10^{-15} \text{ ergs cm}^{-2} \text{ s}^{-1}$. The sources containing AGNs based on their X-ray luminosities are enclosed in green squares. There is a linear correlation (*black solid line*) between large reradiated fluxes and $24 \mu\text{m}$ detections with a large spread (± 0.5 dex, *blue dashed lines*).

We may test the extinctions derived from the BC03 fits by comparing the extinguished UV light, which is reradiated into the FIR, with other completely independent measures of the dust reradiated light, such as the $24 \mu\text{m}$ light. This is the longest wavelength light for which ex-

tremely deep images of the field have been obtained. In Figure 7 we show the fraction of galaxies detected at $24 \mu\text{m}$ (*red histogram*). Interestingly, we see that nearly all of the highly extinguished sources are also detected at $24 \mu\text{m}$. To further quantify this comparison, we computed the reradiated UV light from each galaxy in the mid- z sample by subtracting the observed SED from the extinction corrected SED. In Figure 8 we show the difference in the rest-frame $2000 - 3000 \text{ \AA}$ wavelength range (i.e., the UV flux that got reradiated) versus the rest-frame $24 \mu\text{m}$ flux (K -corrected using the M82 SED of Silva et al. 1998).

The sources with large reradiated fluxes are generally detected at $24 \mu\text{m}$, with a linear relation shown by the solid black line. There is a large spread in the relation (± 0.5 dex, shown by the blue dashed lines), which most likely reflects the use of only the M82 template to obtain the K -corrections for the $24 \mu\text{m}$ flux (see, e.g., Dale et al. 2005; Marcillac et al. 2006; Barger et al. 2007 for why this is not ideal). However, there is no substantial redshift change, with the higher redshift points (*red diamonds*) having the same distribution as the lower redshift points (*black squares*).

These results show that the assignment of substantial extinctions to galaxies by our BC03 fits is confirmed by the MIR measurements. About 60% of the $24 \mu\text{m}$ sources in the mid- z sample to the $80 \mu\text{Jy}$ flux limit of the $24 \mu\text{m}$ data are picked out in this way and lie between the dashed lines in Figure 8. However, some of the remaining $24 \mu\text{m}$ sources in the mid- z sample have low reradiated UV fluxes. (A few percent are clearly blended galaxies, where the $24 \mu\text{m}$ flux arises from a different galaxy than the one being fitted in the UV, but this is a small effect.) Therefore, a critical question for the present analysis is whether this implies that we are failing to assign extinctions to galaxies where there should be extinctions.

We have checked this by inspecting the spectra (see §5) of the galaxies in the mid- z sample with $H\alpha$ in their spectrum which are detected at $24 \mu\text{m}$ but for which our BC03 fits have assigned a low extinction. In all cases the $f(H\beta)/f(H\alpha)$ ratios are also consistent with little extinction. These sources may contain obscured nuclei that are only seen in the MIR and have little effect on the measured properties of their host galaxies. Indeed, the brightest $24 \mu\text{m}$ source in the mid- z sample is not picked out by its reradiated UV flux. It is an X-ray source, and it has a Seyfert 2 spectrum, which suggests that it is an obscured AGN. There is also a higher fraction of X-ray AGNs among the remaining sources with $24 \mu\text{m}$ detections but low reradiated UV fluxes. (In Figure 8 we enclose in green open squares sources containing AGNs based on their X-ray luminosities.) However, many of these sources are not X-ray detected and, if the $24 \mu\text{m}$ light in these sources is produced by AGN activity, then the nucleus must be highly obscured in the optical and in the X-ray.

4.2. Masses

In Figure 9 we show the ratio of the stellar mass to the observed (i.e., uncorrected for extinction) NIR luminosity versus the observed NIR luminosity for our low- z and mid- z samples. We hereafter refer to this ratio as the mass ratio. For both samples the mass ratios range from values of about 10^{-34} (blue galaxies) to 10^{-33} (evolved galaxies with ages comparable to the present age of the

universe), though the more luminous galaxies are primarily at the high (evolved) end. Multiplying the 10^{-33} upper limit on the mass ratio (*purple line*) by the NIR luminosity limits of the low- z and mid- z samples, we find that this upper limit implies that the low- z and mid- z samples include all galaxies with masses above $\sim 2 \times 10^9 M_\odot$ and $\sim 10^{10} M_\odot$, respectively. For our high- z and highest- z samples, the corresponding mass limits are $2 \times 10^{10} M_\odot$ and $3 \times 10^{10} M_\odot$, respectively.

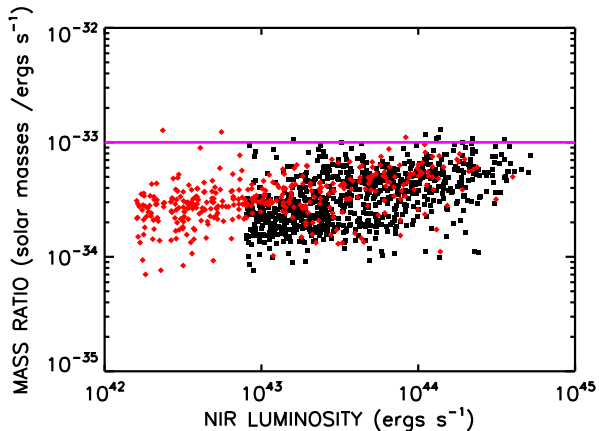


FIG. 9.— Ratio of the stellar mass to the observed (i.e., uncorrected for extinction) NIR luminosity vs. observed NIR luminosity. The mass ratios were computed from our BC03 fits, which include the effects of extinction. The low- z (mid- z) sample is shown with the red diamonds (black squares). The purple line shows the maximum mass ratio adopted in computing the mass limits on the samples.

We also computed the mass to luminosity ratios ($M/L_{z'}$) for the extinction corrected z' -band luminosity, $L_{z'}$, following the procedures given in Kauffmann et al. (2004). For $z = 0.05 - 0.9$, we obtain a median $M/L_{z'} = 1.1$ in the $10^{11} - 10^{12} M_\odot$ range and a median $M/L_{z'} = 0.7$ in the $10^{10} - 10^{11} M_\odot$ range. As expected, since the high-redshift galaxies are younger and have higher star formation rates, these values are about a factor of two lower than the local values. After correcting the Kauffmann et al. (2004) local sample's Kroupa IMF stellar masses to our Salpeter IMF stellar masses, their median values are about 2.5 for the high-luminosity galaxies and about 1.1 for the lower luminosity galaxies, which we may roughly compare with our mass-selected values.

In Figure 10 we show the stellar masses of the galaxies in our NIR sample over the redshift range $z = 0.05 - 1.5$. The purple solid lines show the mass limits given above, to which we expect each of the samples to be complete. (Note that the purple line for the mid- z sample has been truncated below $z = 0.475$ where the sample overlaps with the high-mass end of the low- z sample.) We mark with red diamonds the sources with 2 – 8 keV or 0.5 – 2 keV luminosities above $3 \times 10^{43} \text{ ergs s}^{-1}$, where the AGN luminosity could contaminate the NIR photometry. However, the number of such sources is too small to affect the results. There are only a small number of very high-mass galaxies in the sample. Between $z = 0$ and $z = 1.5$ we find only 13 galaxies with masses above $10^{11.5} M_\odot$ (shown by the green dashed line in Figure 10). As can be seen from the figure, there is a tendency for the more massive galaxies to lie in the high-density filaments in the sample (Cohen et al. 1996, 2000). We will return to this point in §11.8 when

we consider the environmental dependences of the sample.

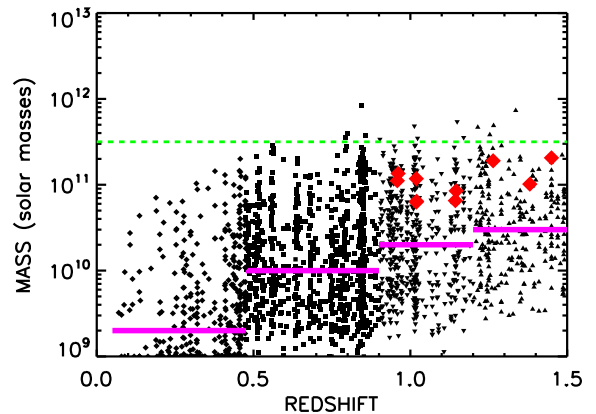


FIG. 10.— Stellar mass vs. redshift for $z = 0.05 - 0.475$ (*diamonds*), $z = 0.475 - 0.9$ (*squares*), $z = 0.9 - 1.2$ (*downward pointing triangles*), and $z = 1.2 - 1.5$ (*upward pointing triangles*). The purple horizontal lines show the masses above which each sample (low- z , mid- z , high- z , highest- z) is expected to be complete. Note that the purple line for the mid- z sample has been truncated below $z = 0.475$ where that sample overlaps with the high-mass end of the low- z sample. The red diamonds show the small number of X-ray sources with 2 – 8 keV or 0.5 – 2 keV luminosities above $3 \times 10^{43} \text{ ergs s}^{-1}$. The green dashed line shows a logarithmic mass of $11.5 M_\odot$, above which there are relatively few galaxies.

5. SPECTRAL LINE MEASUREMENTS

5.1. Equivalent Widths

For each spectrum we measured the equivalent widths (EWs) of a standard set of lines: [S II] $\lambda\lambda 6717, 6731$, H α $\lambda 6563$, [N II] $\lambda 6584$, [O III] $\lambda 5007$, H β $\lambda 4861$, and [O II] $\lambda 3727$. For the stronger lines (rest-frame EW > 10 Å) we used a full Gaussian fit together with a linear fit to the continuum baseline. For the weaker lines we held the full width constant using the value measured in the stronger lines, if this was available, or, if not, then using the nominal width (i.e., the resolution of the spectrum). For the weaker lines we also set the central wavelength to the redshifted value. We measured the noise as a function of wavelength by fitting to random positions in the spectrum and computing the dispersion in the results.

In Figure 11a we show the rest-frame EW(H β) versus NIR luminosity for the mid- z (0.05 – 0.9) sample, and in Figure 11b we show the rest-frame EW(H α) versus NIR luminosity for the low- z (0.05 – 0.475) sample. Both show a strong trend to higher EWs at lower NIR luminosities (see also Fig. 12), reflecting the higher specific star formation rates (the star formation rate per unit galaxy stellar mass) in the smaller galaxies. Absorption line galaxies (*red squares*) appear at $\gtrsim 10^{43} \text{ ergs s}^{-1}$.

Roughly half of the mid- z sample have rest-frame EW(H β) > 4 Å. At this EW the emission lines may be strong enough to make metallicity estimates with line ratios. The fraction of galaxies with a corresponding rest-frame EW(H α) > 12 Å (assuming the case B Balmer ratio discussed below) in the low- z sample is closer to 75%.

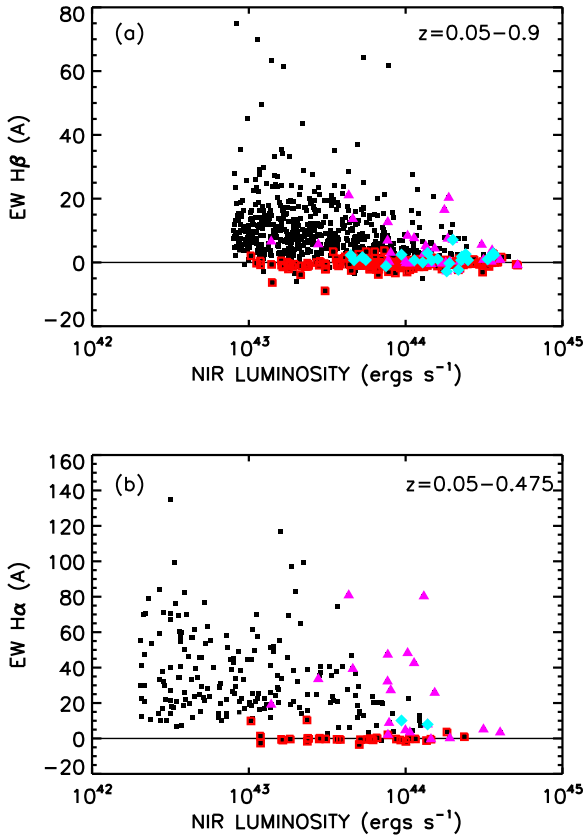


FIG. 11.— (a) Rest-frame $EW(H\beta)$ vs. NIR luminosity for the $z = 0.05 - 0.9$ mid- z sample. (b) Rest-frame $EW(H\alpha)$ vs. NIR luminosity for the $z = 0.05 - 0.475$ low- z sample. In both panels the cyan diamonds show sources containing AGNs based on their X-ray luminosities, the purple triangles show 20 cm detected sources, and the red squares show sources with absorption line redshifts.

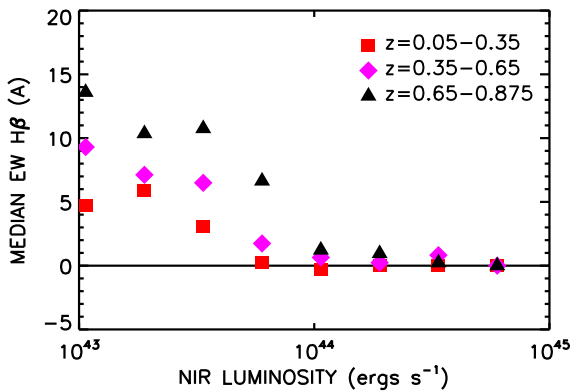


FIG. 12.— Median rest-frame $EW(H\beta)$ vs. NIR luminosity for the mid- z sample. The symbols correspond to values in the redshift intervals $z = 0.65 - 0.9$ (black triangles), $z = 0.35 - 0.65$ (purple diamonds), and $z = 0.05 - 0.35$ (red squares). The presence of strong emission lines suitable for measuring metallicities is highly dependent on both NIR luminosity and redshift.

We also show in Figures 11a and 11b the sources that contain AGNs based on their X-ray luminosities (*cyan diamonds*) and the 20 cm detected sources (*purple triangles*). While the 20 cm sources often have quite strong

Balmer emission lines, consistent with them being high-end star formers, the AGNs generally have weak Balmer emission lines. The weakness of the AGN Balmer lines results in most of them being automatically excluded from our metallicity analysis, but we also use the X-ray signatures to identify and exclude any remaining AGNs.

Not only is the presence of strong emission lines a strong function of NIR luminosity, but because of the decrease in the overall star formation rates with decreasing redshift, it is also a strong function of redshift. We show this in Figure 12, where we plot the median rest-frame $EW(H\beta)$ for the mid- z sample versus NIR luminosity for three redshift intervals spanning the full redshift range. The rapid drop in the EWs with decreasing redshift can be clearly seen. The change in the emission line strengths with redshift introduces a strong selection bias when comparing emission line metallicities in galaxies at different redshifts. This is an important point, which we will return to in §10.

The $EW(H\beta)$ is reduced by the effects of the underlying stellar absorption, and we must correct for this effect. The simplest procedure is to apply a single offset. Kobulnicky & Phillips (2003) found an offset of -2 \AA by measuring several Balmer lines in 22 galaxy spectra (referred to as the K92+ sample in their paper) and obtaining a self-consistent reddening and stellar absorption solution for each galaxy. However, the correction in our data is smaller than this, possibly because of the fitting methods we used. In particular, the Gaussian fits to the emission lines are narrower than the absorption lines, and it is only the absorption integrated through the Gaussian which we need to correct.

We have estimated the correction as follows. First we averaged the normalized spectra of galaxies in the low- z sample grouped by $EW(H\alpha)$. We show a few of these averaged spectra in Figure 13 [those with $EW(H\alpha) < 5 \text{ \AA}$, $EW(H\alpha) = 5 - 15 \text{ \AA}$, $EW(H\alpha) = 15 - 30 \text{ \AA}$, and $EW(H\alpha) = 30 - 60 \text{ \AA}$], where the bottom spectrum [$EW(H\alpha) < 5 \text{ \AA}$] is the averaged spectrum of the absorption line galaxies in the low- z sample (i.e., the absence of $H\alpha$ emission guarantees that there is little $H\beta$ emission). We then renormalized the averaged spectrum of the absorption line galaxies to match each of the other averaged spectra in wavelength regions outside the emission lines. These fits are shown in Figure 13 in red. The renormalized absorption spectrum was then subtracted to form a corrected spectrum. Finally, we measured the $EW(H\beta)$ in the corrected and uncorrected spectra. In Figure 14 we plot the difference of these two measurements versus the $EW(H\alpha)$. We see no strong dependence of the $H\beta$ correction on the galaxy type. Thus, we adopt a fixed offset of 1 \AA to correct for the stellar absorption, regardless of galaxy type. (Our results are not significantly changed if we use a 2 \AA rather than a 1 \AA correction.) In our metals analysis we will restrict to galaxies with corrected $EW(H\beta) > 4 \text{ \AA}$ to minimize the systematic uncertainties introduced by this procedure. Hereafter, we refer to the corrected $EW(H\beta)$ as $EW(H\beta)$.

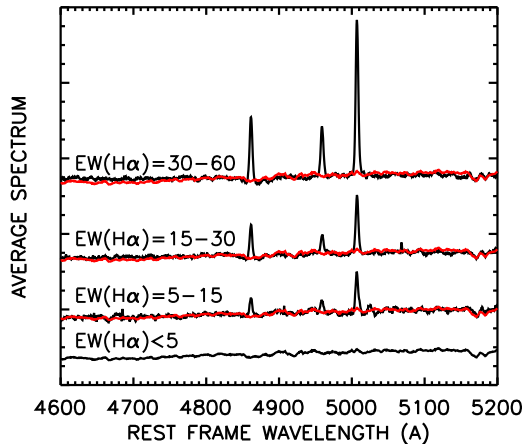


FIG. 13.— Averages of the normalized spectra vs. rest-frame wavelength for galaxies in the low- z sample (*black spectra*). The bottom spectrum shows the averaged spectrum for sources with rest-frame $\text{EW}(\text{H}\alpha) < 5 \text{ \AA}$. This defines an absorption line spectrum. The remaining spectra from bottom to top correspond to rest-frame $\text{EW}(\text{H}\alpha) = 5 - 15$, $15 - 30$, and $30 - 60 \text{ \AA}$, respectively. Each spectrum is offset in the vertical direction to separate them. We also show in red the absorption line spectrum normalized to each of the other averaged spectra, which we used to remove the underlying stellar absorption.

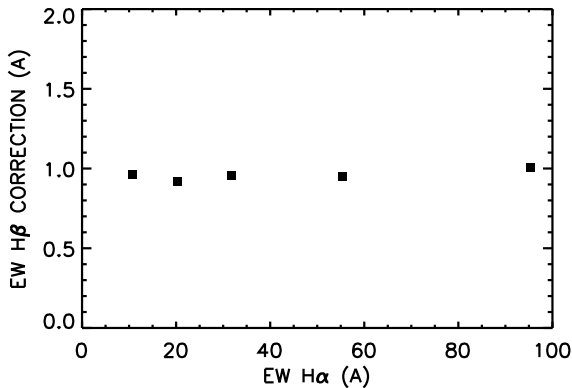


FIG. 14.— Measured correction to the rest-frame $\text{EW}(\text{H}\beta)$ vs. the rest-frame $\text{EW}(\text{H}\alpha)$.

5.2. Line fluxes

Generally the spectra were not obtained at the parallactic angle, since this is determined by the DEIMOS mask orientation. Nor were spectrophotometric standards regularly observed. Thus, flux calibration is difficult and special care must be taken in determining fluxes. Relative line fluxes can be measured from the spectra without flux calibration, as long as we restrict the line measurements to the short wavelength range where the DEIMOS response is essentially constant. For example, one can assume the responses of neighboring lines (e.g., $[\text{O III}] \lambda 4949$ and $[\text{O III}] \lambda 5007$) are the same and then measure the flux ratio without calibration. However, to measure quantities such as the R23 metal diagnostic ratio (see §8.4 for definition) and to estimate the extinction and ionization parameters in the galaxies, we must calibrate the line fluxes over much wider wavelength ranges. We do this by using the broadband fluxes to calibrate the local continuum. We

then use the equivalent width to compute the line flux. This method should work well as long as the sky subtraction is precise and the spectral continuum level well determined.

In addition to the line fluxes, we also measured the 4000 Å break strength in the galaxies. To do this we measured the ratio of the average flux (in units of $\text{ergs cm}^{-2} \text{ s}^{-1} \text{ Hz}^{-1}$) at $4050 - 4250 \text{ \AA}$ to that at $3750 - 3950 \text{ \AA}$ using the extinction corrected spectra normalized by the instrument throughput, which was measured by R. Schiavon

(<http://www.ucolick.org/~ripisc/results.html>). Given the short wavelength span, this ratio should be fairly insensitive to the flux calibration and extinction, but it could be affected by the accuracy of the absolute sky subtraction.

We can use the calibrated spectra to search for any relative offsets in the determination of the zero points in the imaging data, and inversely we can test the spectral shapes by comparing with the photometric colors from the imaging data. We carried out these tests by computing the ratio of the rest-frame B to U bands from the spectra and comparing this with the photometrically determined values for galaxies with masses $> 10^{10} M_{\odot}$. Over this wide wavelength range we found that the measured offsets between the photometric and spectroscopic measurements showed no dependence on redshift over the $z = 0 - 1.1$ range where the values can be measured (see Figure 15). (Beyond $z = 1.1$ the 4500 \AA band moves above the upper wavelength limit of the spectra.) This shows that there are no relative errors in the photometric calibration of the UV and optical data. There is a only a small systematic offset throughout which averages to -0.05 mag . Translated to the smaller wavelength range used in the 4000 Å break measurement, we will underestimate the break strength by a multiplicative factor of 1.02 on average. The measured spread in the offsets translates to a 1σ multiplicative error of 1.07 in the individual 4000 Å break strengths.

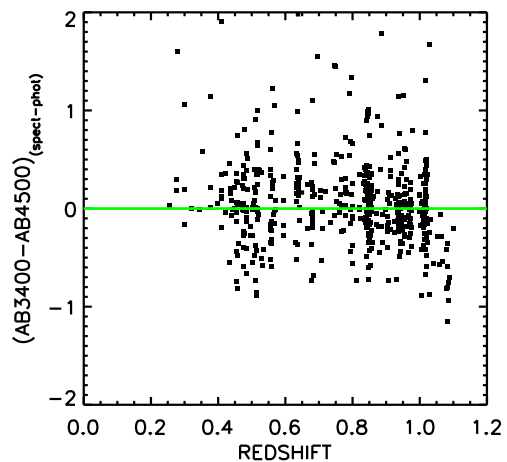


FIG. 15.— Magnitude offset between the rest-frame 3400–4500 Å magnitudes measured from the spectra and those measured from the photometry vs. redshift for $z = 0 - 1.1$ galaxies with masses $> 10^{10} M_{\odot}$ (*black squares*).

6. CONTINUUM VERSUS LINE EXTINCTION

Ideally we would measure the extinctions for the line fluxes from the Balmer ratio $f(\text{H}\alpha)/f(\text{H}\beta)$, since the H II

regions producing the emission lines may have different reddening from the stars providing the continuum. In particular, we might expect reddening in the H II region to be systematically higher than reddening in the continuum, if the H II regions lie in regions of higher gas density (Kinney et al. 1994). However, in the present sample we can only measure the Balmer ratio extinction in the low- z sample. While our analysis of the star formation and stellar mass density histories can be done without reference to the line fluxes, we do require an estimate of the line extinction in computing the metallicity diagnostics and in comparing equivalent widths with galaxy models.

We therefore checked how well the continuum extinctions derived from the BC03 fits match to the extinctions derived from the Balmer ratios in the low- z sample. In Figure 16a we show $f(\text{H}\beta)/f(\text{H}\alpha)$ versus NIR luminosity for the low- z sample with rest-frame $\text{EW}(\text{H}\alpha) > 12 \text{ \AA}$. At low NIR luminosities the median values (*red squares*) are very close to an intrinsic $f(\text{H}\beta)/f(\text{H}\alpha)$ ratio of 0.35 (the ratio for case B recombination at $T = 10^4 \text{ K}$ and $n_e \sim 10^2 - 10^4 \text{ cm}^{-3}$, Osterbrock 1989; *red solid line*), suggesting that there is little extinction. Only in the highest luminosity galaxies (NIR luminosities $> 10^{44} \text{ ergs s}^{-1}$) does the ratio fall significantly below the case B ratio. The highest NIR luminosity galaxies pick out the 20 cm detected sources, which are shown with the cyan triangles.

In Figure 16b we show the Balmer ratio after applying the extinction corrections derived from our BC03 fits. As can be seen from the median values (*red squares*), this completely removes the dependence on NIR luminosity. Thus, the SED derived extinctions can be used to correct the average line ratios. However, the individual points still scatter significantly about the median, implying that there are systematic uncertainties in the flux determinations.

We next estimated the extinctions from the Balmer ratios for the low- z sample with rest-frame $\text{EW}(\text{H}\alpha) > 12 \text{ \AA}$ and made a linear fit against the continuum extinctions. This gives the relation

$$E(B - V)_{\text{spectral}} = 0.0 + (0.87 \pm 0.18)E(B - V)_{\text{BC03}}. \quad (2)$$

This suggests that the line extinction is, if anything, smaller than the continuum extinction, but that, within the errors, the two extinction measurements are consistent on average. We will therefore use the BC03 extinctions to deredden the line fluxes at higher redshifts. However, we will regularly check to make sure that this assumption is providing consistent results.

7. STAR FORMATION RATES

7.1. Relative Calibrations

Extensive discussions of the calibrations of the star formation diagnostics can be found throughout the recent literature (e.g., Kennicutt 1998; Rosa-González et al. 2002; Hopkins et al. 2003; Kewley et al. 2004; Moustakas et al. 2006). However, for consistency, it is best to internally calibrate data sets where possible. We can do this using our low- z sample.

In Figures 16c and 16e we show, respectively, $f([\text{O II}])/f(\text{H}\alpha)$ and $f(\text{UV})/f(\text{H}\alpha)$ versus NIR luminosity for the low- z sample with rest-frame $\text{EW}(\text{H}\alpha) > 12 \text{ \AA}$. Here we have defined the rest-frame UV luminosity as the integral over the frequency range 10^{15} to

$1.5 \times 10^{15} \text{ Hz}$ (which corresponds to the wavelength range 1993 to 2990 \AA) minus 0.03 of the NIR luminosity. The latter correction, the value of which was determined from absorption line galaxies in the sample, removes the contribution from the older stars in the galaxy. Since our shortest measured wavelength is the U -band centered at 3700 \AA , determining the UV luminosity requires an extrapolation for the lowest redshift sources.

Similar to what we saw for the Balmer ratio, there is substantial extinction only in the highest NIR luminosity galaxies. In Figures 16d and 16f we plot the same ratios shown, respectively, in Figures 16c and 16e, but this time after applying our BC03 extinction corrections. Again the medians (*red squares*) are flattened out by the extinction corrections.

To obtain the SFR calibrations and to quantify the scatter in the flux ratios, in Figure 17 we show, respectively, the distribution of the extinction corrected logarithmic (a) Balmer ratios, (b) $f([\text{O II}])/f(\text{H}\alpha)$ ratios, and (c) $f(\text{UV})/f(\text{H}\alpha)$ ratios (*black histograms*), together with Gaussian fits to the distributions (*purple dashed curves*). The mean value of the extinction corrected Balmer ratios agrees precisely with the case B ratio (*red line in Fig. 17a*), illustrating how well the extinction corrections work. However, there is a symmetric scatter with a 1σ dispersion of 0.13 dex in the Balmer ratio about the case B value. We take this as a rough measure of the systematic and statistical errors in the extinction corrected flux determinations at the $\text{H}\beta$ wavelength relative to $\text{H}\alpha$.

Regarding the $f([\text{O II}])/f(\text{H}\alpha)$ ratio, it has been shown that there is a dependence of this ratio on the oxygen abundance (e.g., Kewley et al. 2004; Mouhcine et al. 2005; Moustakas et al. 2006). In fact, it can be seen from Figures 17b and 17c that the UV flux has a somewhat tighter relation to the $\text{H}\alpha$ flux than the $[\text{O II}]$ flux does, despite both the extrapolation made to shorter wavelengths for the lowest redshift sources to determine the UV flux and the larger wavelength separation of the UV from $\text{H}\alpha$ than of $[\text{O II}]$ from $\text{H}\alpha$ (which means any uncertainties in the extinction corrections would have a larger effect). In addition, there are no significant outliers in the $f(\text{UV})/f(\text{H}\alpha)$ ratios, unlike the case for the $f([\text{O II}])/f(\text{H}\alpha)$ ratios.

We can now use the flux ratios to determine the calibrations to star formation rates (SFRs). We use as our primary calibration the conversion of $L(\text{UV})$ to SFR from the BC03 models. The calibration for any individual galaxy depends on the galaxy star formation history (SFH), but the ensemble average is well determined since it is simply the amount of UV light produced per unit mass of stars. Since our principal goal is to compute the universal SFH, this is the appropriate quantity to choose. For our definition of the rest-frame UV luminosity given above,

$$\log \text{SFR} = -42.63 + \log L(\text{UV}). \quad (3)$$

Here the SFR is in M_{\odot} per year and is computed for the Salpeter IMF used throughout this paper. $L(\text{UV})$ denotes the intrinsic (i.e., corrected for extinction) rest-frame UV luminosity and is in units of ergs s^{-1} . Our UV calibration is slightly lower than the value of -42.55 that would be obtained from the commonly used relation given by Kennicutt (1998). The Kennicutt relation is appropriate for

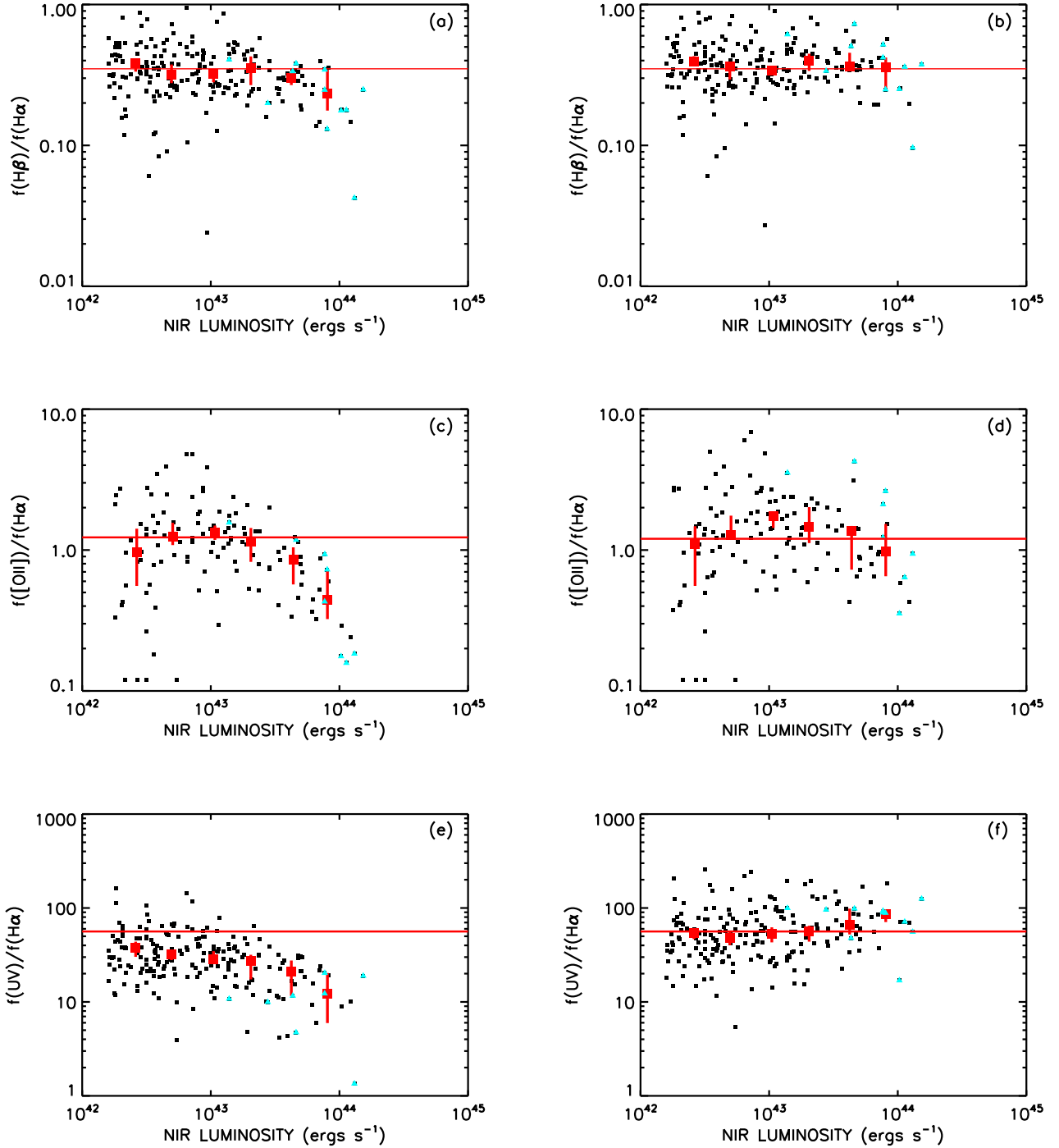


FIG. 16.— In all panels we consider only galaxies in the low- z sample with rest-frame $\text{EW}(\text{H}\alpha) > 12 \text{ \AA}$. The large red squares denote the median values at each luminosity with $\pm 1\sigma$ errors computed using the median sign method. The 20 cm sources are denoted by cyan triangles. All ratios are plotted vs. NIR luminosity. (a) Balmer ratio. (b) Extinction corrected Balmer ratio. In these two panels the case B ratio in the absence of extinction is shown by the red horizontal line. (c) $f([\text{OII}]\lambda 3727)/f(\text{H}\alpha)$. (d) Extinction corrected $f([\text{OII}]\lambda 3727)/f(\text{H}\alpha)$. In these two panels the $f([\text{OII}]\lambda 3727)/f(\text{H}\alpha)$ ratio used to compute the calibration of the $[\text{OII}]\lambda 3727$ determined SFR is shown by the red horizontal line. (e) $f(\text{UV})/f(\text{H}\alpha)$ using the rest-frame UV flux defined in the text. (f) Extinction corrected $f(\text{UV})/f(\text{H}\alpha)$. In these two panels the $f(\text{UV})/f(\text{H}\alpha)$ ratio used to compute the calibration of the UV determined SFR is shown by the red horizontal line.

an individual galaxy undergoing constant star formation, which gives a lower UV flux per unit SFR.

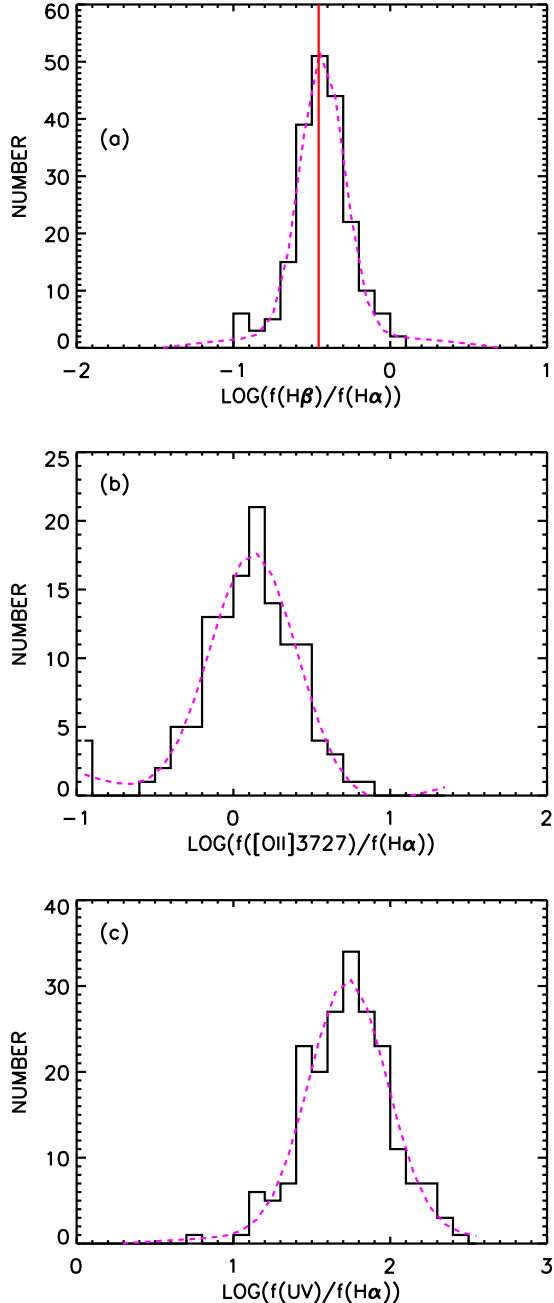


FIG. 17.— Distribution of the logarithm of the extinction corrected ratio of (a) $H\beta$ $\lambda 4861$, (b) $[O II] \lambda 3727$, and (c) rest-frame UV flux as defined in the text to the $H\alpha$ $\lambda 6563$ flux for the low- z sample with rest-frame $EW(H\alpha) > 12 \text{ \AA}$ (black histograms). In each case the Gaussian fit is shown by the purple dashed curve. In (a) the red vertical line shows the case B value, which agrees precisely with the mean measured ratio.

We next compute the $H\alpha$ calibration relative to our UV calibration based on the data. We must be careful in our object selection here since there is a potential problem with using objects selected to have $H\alpha$ flux. This arises because the $H\alpha$ is produced by more massive and younger stars than those responsible for the UV light. As long as the SFR is smoothly changing with time, then this is not

a large effect. However, if the galaxies undergo episodic bursts rather than a smooth evolution (as we shall argue is the case in §11.6), then we will bias this ratio since we will not count galaxies which still have substantial UV light but where $H\alpha$ producing stars are no longer present. The different time averaging present in the emission line and UV calibrations should be borne in mind when considering the SFR of individual galaxies, but it should average out in the ensemble.

We can properly calibrate the $H\alpha/UV$ ratio by computing the average $H\alpha/UV$ for a UV-selected sample, which will then include all of the $H\alpha$ emitters as a subsample. Using the UV-selected sample we obtain

$$\log \text{SFR} = -40.90 + \log L(H\alpha), \quad (4)$$

with a 1σ spread of 0.24 dex. This differs by 0.2 dex from the value of -41.1 given in Kennicutt (1998) and is also higher than the value that would be derived from the BC03 models. (The $H\alpha$ luminosity for the BC03 models is derived from the ionizing photon production assuming this is fully absorbed in the galaxy.) This is not a consequence of the extinction model, since even using the unreddened values only reduces our value to -41.03 .

This result can be restated as the sample having too much UV light relative to $H\alpha$ for the adopted IMF. The $H\alpha$ production is dominated by the most massive stars, and it is probable that the high UV/ $H\alpha$ ratio is a consequence of differences in the true high-end IMF relative to that used in the models. As we noted in the introduction all of the currently used IMFs have similar high mass slopes and so would not change this result. Rather we need more intermediate mass stars relative to the very high mass end in the IMF. Fardal et al. (2007) describe this type of IMF as "paunchy" and as we shall discuss later it can resolve a number of additional problems in making a consistent interpretation of the data set.

From the mean value of the logarithmic $f(H\beta)/f(H\alpha)$ ratio, which is just the case B value (see Fig. 17), we find the calibration of Equation 4 can be translated to

$$\log \text{SFR} = -40.45 + \log L(H\beta), \quad (5)$$

with a 1σ spread of 0.13 dex. $H\beta$ is often avoided as a SFR diagnostic because of concerns about the contamination by the underlying stellar absorption. However, with such a low 1σ spread for our low- z sample, it appears to be quite a good diagnostic.

From Figure 17 we saw that the UV flux provided a better estimate of the SFR than the $[O II]$ flux did. The average calibration for $[O II]$, using the mean value of the logarithmic $f([O II])/f(H\alpha)$ ratio, is

$$\log \text{SFR} = -41.03 + \log L([O II] \lambda 3727), \quad (6)$$

with a 1σ spread of 0.26 dex. This may be compared with the value of -40.85 given in Kennicutt (1998).

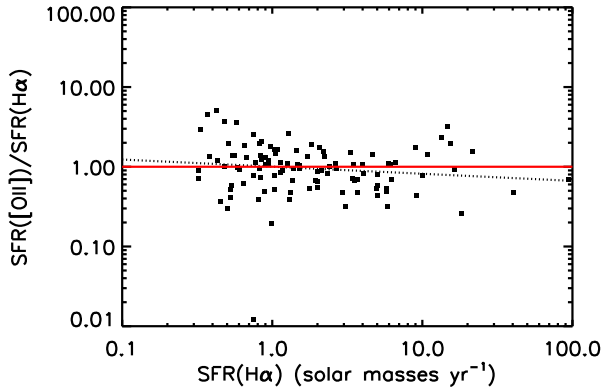


FIG. 18.— Ratio of the [O II] SFR to the $H\alpha$ SFR versus the $H\alpha$ SFR (all extinction corrected) for the low- z sample with $EW(H\alpha) > 12 \text{ \AA}$ and $\log(SFR(H\alpha)) > -0.5$ (black squares). The black dotted line shows the least-square polynomial fit with a gradient of -0.09 dex per dex.

The broader spread in the [O II] calibration is reflected in its systematic dependence on the galaxy properties. In Figure 18 we show the weak dependence of the ratio of the [O II] SFR to the $H\alpha$ SFR on the $H\alpha$ SFR (all extinction corrected). There is a 0.09 ± 0.05 dex decline per dex increase in the $H\alpha$ SFR, which is slightly larger than the locally measured 0.03 ± 0.02 dex decline per dex increase in the $H\alpha$ SFR measured to somewhat lower $H\alpha$ SFRs (Kewley et al. 2004) but consistent within the errors. We show in §7.2 that the dependence of the SFR ratio on the mass of the galaxy is even stronger than its dependence on the $H\alpha$ SFR of the galaxy.

Given the larger scatter and systematic dependences of the [O II] calibration, we will adopt the UV calibration as our primary calibration.

7.2. Comparisons Using the Mid- z Sample

We next tested the relative [O II] and $H\beta$ calibrations against our primary UV calibration over the wider redshift range of the full mid- z sample ($z < 0.9$). In Figure 19a we plot the ratio of the [O II] SFR to the UV SFR (both extinction corrected) versus galaxy mass. We show the lower redshift sources ($z = 0.05 - 0.475$) with red diamonds and the higher redshift sources ($z = 0.475 - 0.9$) with black squares, and we only show the results above the mass at which each redshift range is complete. The ratio changes slowly with both mass and redshift. The change is a 0.19 dex decline per dex increase in mass and a 0.04 dex increase between the low and high redshift ranges. This probably primarily reflects the higher metallicity in the more massive galaxies and the increase of metallicity to lower redshifts, which results in temperature changes in the H II regions and the [O II] line being stronger relative to the primary $H\alpha$ line. Thus, if we were to use our [O II] calibration, we would find it difficult to study the evolution of the SFRs as a function of redshift, mass, and metallicity.

In contrast, as shown in Figure 19b (same symbols as in Fig. 19a), the ratio of the $H\beta$ SFR to the UV SFR (both extinction corrected) varies more slowly with galaxy mass and does not vary significantly with redshift. The change

with mass is a 0.11 dex decline per dex increase in galaxy mass. Thus, $H\beta$ can also be used over the $z = 0.05 - 0.9$ range where it can be measured.

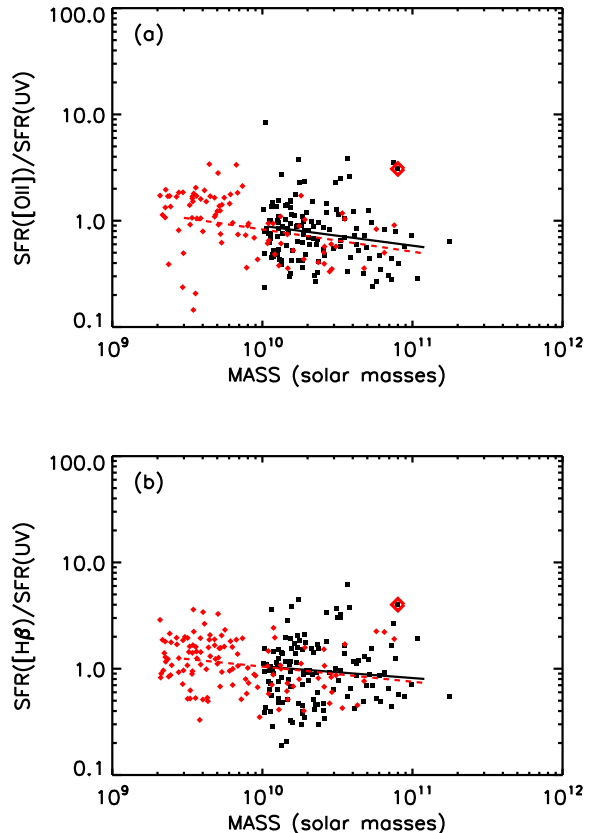


FIG. 19.— (a) Ratio of the [O II] SFR to the UV SFR (both extinction corrected) vs. galaxy mass. (b) Ratio of the $H\beta$ SFR to the UV SFR (both extinction corrected) vs. galaxy mass. Only sources with $EW(H\beta) > 4 \text{ \AA}$ are included. The red diamonds (black squares) show the results for $z = 0.05 - 0.475$ ($z = 0.475 - 0.9$). We show the results only above the mass at which each redshift interval is complete. The least-square polynomial fits are shown with the dashed red (solid black) lines for the $z = 0.05 - 0.475$ ($z = 0.475 - 0.9$) sample. The one AGN based on its X-ray luminosities is enclosed in the large red diamond and is excluded from the fits. In (a) there is a significant gradient with mass and a small amount of evolution between the two redshift samples. In (b) there is a smaller change with galaxy mass and no significant evolution between the two redshift samples.

7.3. Comparison with $24 \mu\text{m}$

Using the observed-frame $24 \mu\text{m}$ fluxes of the galaxies is a relatively poor way to determine the FIR luminosities and hence SFRs of the galaxies (e.g., Dale et al. 2005). However, because of the ready availability of $24 \mu\text{m}$ data from the *Spitzer* MIPS observations, this has become a common way of estimating SFRs, and nearly all of the papers that we will compare with use some version of this method to determine their SFRs. We therefore compare with $24 \mu\text{m}$ determined SFRs here.

We compute the $24 \mu\text{m}$ SFRs following the prescription given in Conselice07. We use the Dale & Helou (2002) SEDs to convert the $24 \mu\text{m}$ flux to FIR luminosity following Figure 7 of Le Floch et al. (2005). We then use the Bell et al. (2005) relation between the reradiated SFR and

the FIR luminosity (converted to the Salpeter IMF of the present paper),

$$\log \text{SFR} = -43.36 + \log L(\text{FIR}), \quad (7)$$

to compute the SFRs.

In Figure 20 we compare the SFRs determined from the $24 \mu\text{m}$ fluxes with the reradiated SFRs determined from the UV luminosities. (Here the reradiated SFR is the difference between the SFR computed after correcting for extinction and the SFR computed without an extinction correction.) In each redshift interval we only show the sources with sufficiently high SFRs that they will lie above the $80 \mu\text{Jy}$ sensitivity of the $24 \mu\text{m}$ observations.

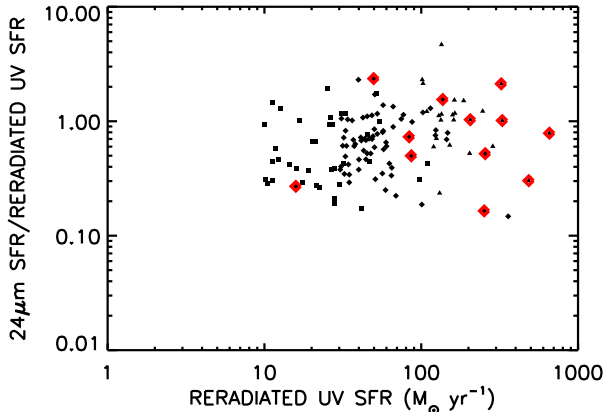


FIG. 20.— Ratio of the $24 \mu\text{m}$ SFR to the reradiated UV SFR vs. the reradiated UV SFR. The sources are separated by redshift interval and are only shown if their SFR is above the SFR where the galaxies will be detected at the flux limit for the $24 \mu\text{m}$ sample. Squares correspond to $z = 0.05 - 0.475$ and are shown above $10 M_{\odot} \text{ yr}^{-1}$, diamonds correspond to $z = 0.475 - 0.9$ and are shown above $30 M_{\odot} \text{ yr}^{-1}$, and triangles correspond to $z = 0.9 - 1.5$ and are shown above $100 M_{\odot} \text{ yr}^{-1}$. Sources containing an AGN based on their X-ray luminosities are enclosed in larger red diamonds.

While there is a considerable spread in the individual SFR ratios, there is no clear dependence on redshift or on SFR. The normalization difference between the two methods is only -0.08 dex in the ensemble average, which is well within the uncertainties in the calibrations. The ensemble distribution is symmetric about the average with a 1σ multiplicative spread of 0.29 dex. Thus, while there is a substantial spread in the individual galaxy determinations, the two methods give good agreement when applied to the galaxy population as a whole. Excluding AGNs based on their X-ray properties (i.e., sources enclosed in red diamonds in Figure 20) has no effect on the relative calibration.

8. METALLICITIES IN THE EMISSION LINE GALAXIES: THE LOW-Z SAMPLE

We may construct a number of emission line diagnostics for the low- z sample, since many of the spectra cover all of the emission lines from [O II] to [S II]. We therefore begin with a comparison of the metallicity-luminosity and metallicity-mass relations for these sources before proceeding to the mid- z sample in §9. We know that the [S II] ratios place most of the galaxies in the low-density regime, but we do not use this information further.

8.1. [NII]/[OII] Diagnostic Ratio

Kewley & Dopita (2002; hereafter KD02) advocate the use of the $\text{N2O2} = f([\text{N II}])/f([\text{O II}])$ diagnostic ratio whenever possible, since this ratio is quite insensitive to the ionization parameter q and has a strong dependence on metallicity above $\log(\text{O}/\text{H})+12 \sim 8.5$. However, the downside of this diagnostic ratio is that it compares two widely separated lines where the uncertainties in the flux calibration and extinction are more severe. Throughout this section we use the BC03 extinctions of §4.

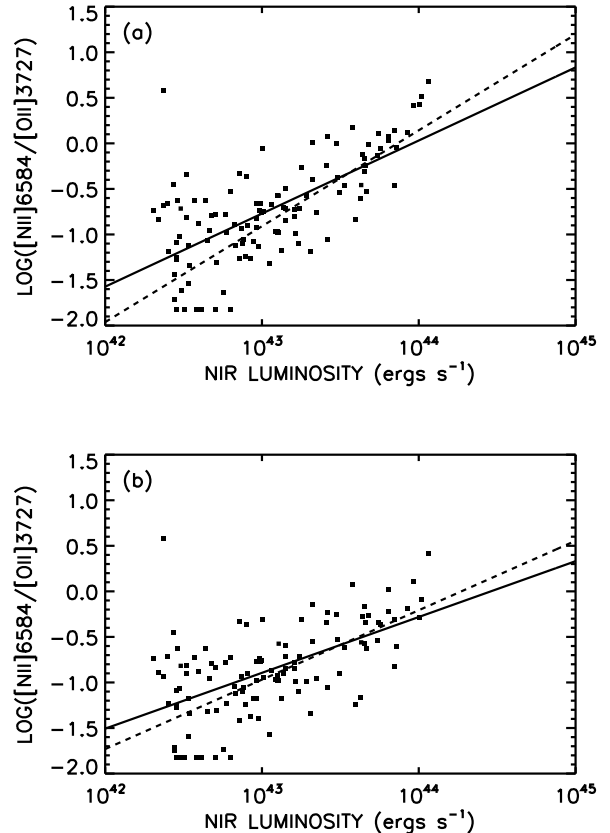


FIG. 21.— Logarithmic (a) extinction uncorrected and (b) extinction corrected N2O2 diagnostic ratio vs. NIR luminosity for the sources in the low- z sample with $\text{EW}(\text{H}\alpha) > 12 \text{ \AA}$ and an [O II] line that can be measured (*black squares*). The sources with a flux ratio less than 0.015 are plotted at that value (-1.82 in the logarithm). In each panel the solid line shows the least-square polynomial fit to all the data, and the dashed line shows the least-square polynomial fit to only the data with NIR luminosities in the range $10^{43} - 10^{44} \text{ ergs s}^{-1}$.

In Figure 21 we plot (a) extinction uncorrected and (b) extinction corrected N2O2 versus NIR luminosity for the 115 sources in the low- z sample with $\text{EW}(\text{H}\alpha) > 12 \text{ \AA}$ and an [O II] line that can be measured (it can be negative). These sources cover the redshift range $z = 0.2 - 0.475$ and have a median redshift of $z = 0.4$. We find a strong correlation between N2O2 and NIR luminosity. For each panel in Figure 21 we use a solid line to show the least-square polynomial fit to all the data. In the faintest sources the $f([\text{N II}])$ and $f([\text{O II}])$ are weak, which results in larger scatter. For example, the extreme up-scattered point at low NIR luminosity in Figure 21 is a source with very

weak $f(\text{[N II]})$ and $f(\text{[O II]})$. Thus, for each panel we also do a fit to the data in the restricted NIR luminosity range $10^{43} - 10^{44}$ ergs s^{-1} to minimize these effects (*dashed line*). The relation for the extinction corrected data restricted in luminosity is

$$\log(\text{N2O2}) = -0.94 + (0.63 \pm 0.08) \log(L_N), \quad (8)$$

where L_N is the NIR luminosity in units of 10^{43} ergs s^{-1} .

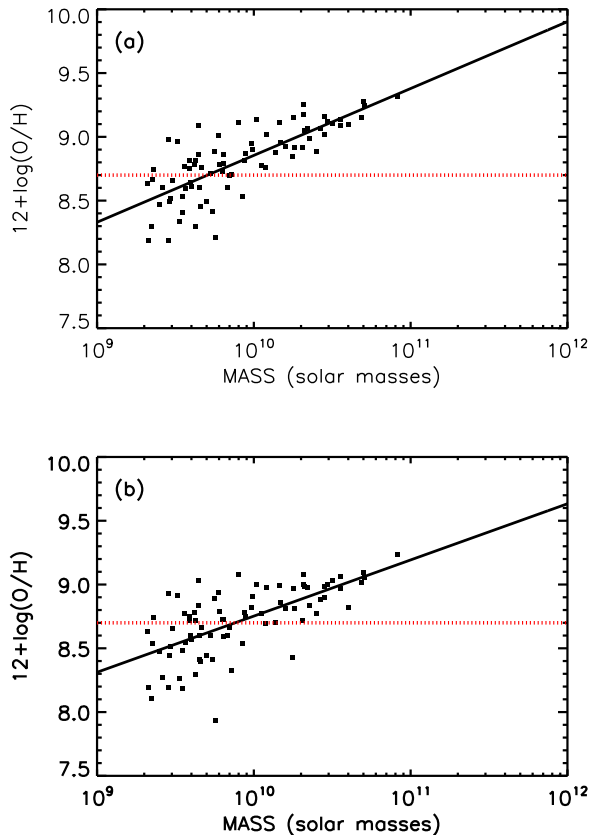


FIG. 22.— Metallicity determined from the (a) extinction uncorrected and (b) extinction corrected N2O2 diagnostic ratio vs. galaxy mass for the sources in the low- z sample with $\text{EW}(\text{H}\alpha) > 12 \text{ \AA}$ and an $[\text{O II}]$ line that can be measured (*black squares*). The conversion is for an ionization parameter $q = 4 \times 10^7 \text{ cm s}^{-1}$, but the conversion is insensitive to this choice. In each panel the black solid line shows the least-square polynomial fit to all the data, and the red dotted line shows the solar abundance.

We use the KD02 calibration (their Eq. 4 and Table 3) to convert our N2O2 values to metallicities, assuming an ionization parameter $q = 2 \times 10^7 \text{ cm s}^{-1}$. This q value is typical of the ionization parameters in our galaxies (see §8.2). However, the present conversion is extremely insensitive to the choice of q . In Figure 22 we plot metallicity determined from (a) extinction uncorrected and (b) extinction corrected N2O2 versus galaxy mass. For each panel we use a solid line to show the least-square polynomial fit to all the data. The metallicity-mass relation for the extinction corrected case is

$$12 + \log(\text{O}/\text{H}) = 8.75 + (0.44 \pm 0.06) \log(M_{10}), \quad (9)$$

where M_{10} is the galaxy mass in units of $10^{10} M_{\odot}$. The extinction corrections flatten the slope (the unextinguished

slope is 0.52 ± 0.06) since they reduce the N2O2 values more substantially in the high mass (high NIR luminosity) galaxies than they do in the lower mass galaxies.

8.2. Ionization Parameter

We can now combine the metallicities determined from extinction corrected N2O2 with extinction corrected O32 $= 1.3 \times f([\text{O III}])/f([\text{O II}])$ to determine the ionization parameters q . Here we do so using the KD02 parameterization of the O32 dependence on q and metallicity. We plot q versus NIR luminosity in Figure 23. The q values lie in a surprisingly small range around a median value of $2.2 \times 10^7 \text{ cm s}^{-1}$, with more than 77% lying within a multiplicative factor of 2 of this value. There also appears to be little dependence of q on NIR luminosity.

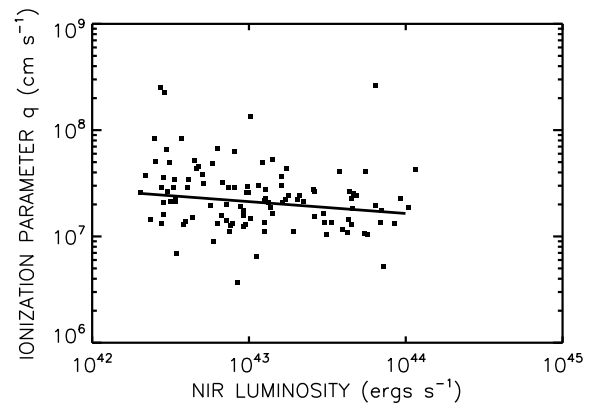


FIG. 23.— Ionization parameter obtained by combining the metallicity determined from the extinction corrected N2O2 diagnostic ratio with the extinction corrected O32 diagnostic ratio vs. NIR luminosity (*black squares*). The effects of the extinction correction are to slightly reduce the average ionization parameter and also to flatten the dependence on luminosity. Most of the sources lie in the $q = 1 - 4 \times 10^7 \text{ cm s}^{-1}$ range with an average value of $q = 2.2 \times 10^7 \text{ cm s}^{-1}$. The black solid line shows the least-square polynomial fit. The ionization parameter shows little dependence on NIR luminosity.

8.3. $[\text{N II}]/[\text{H}\alpha]$ Diagnostic Ratio

The tightly determined q values mean that other diagnostic ratios, such as $\text{NH} = f([\text{N II}])/f(\text{H}\alpha)$, which normally have too much dependence on ionization parameter to be useful, actually work surprisingly well. Because $[\text{N II}]$ and $\text{H}\alpha$ are extremely close in wavelength, NH is not dependent on the extinction corrections nor on the flux calibration methodology and thus provides a powerful check on the metallicities computed from N2O2. In Figure 24 we show NH versus NIR luminosity. There is a strong correlation, which we fit over the NIR luminosity range $10^{43} - 10^{44}$ ergs s^{-1} with the solid line.

We next constructed the metallicity-mass relation from NH using Eq. 12 of Kobulnicky & Kewley (2004; hereafter, KK04) and $q = 2 \times 10^7 \text{ cm s}^{-1}$. (We note that the use of the coefficients given in Table 3 of KD02 for NH appears to give results that are inconsistent with Figure 7 of KD02 and Eq. 12 of KK04.) The metallicity-mass relation,

$$12 + \log(\text{O}/\text{H}) = 8.85 + (0.36 \pm 0.04) \log(M_{10}), \quad (10)$$

is shown in Figure 25 by the black solid line. Recomputing the data points using higher ($q = 4 \times 10^7 \text{ cm s}^{-1}$) or lower ($q = 10^7 \text{ cm s}^{-1}$) ionization parameters and fitting the revised data points (*red dash-dotted lines*) does not substantially change the slope, but it does significantly change the normalization.

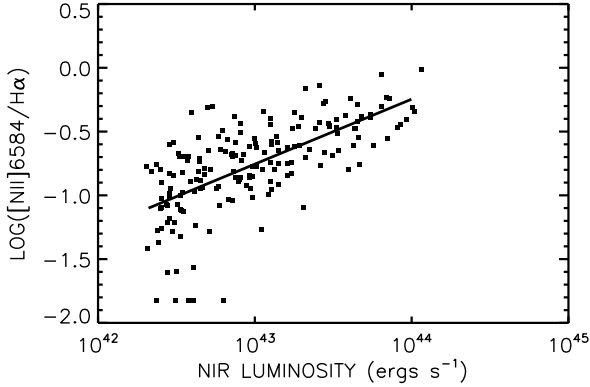


FIG. 24.— Logarithmic NH diagnostic ratio vs. NIR luminosity for the sources in the low- z sample with $\text{EW}(\text{H}\alpha) > 12 \text{ \AA}$ (*black squares*). The black solid line shows the least-square polynomial fit to the data.

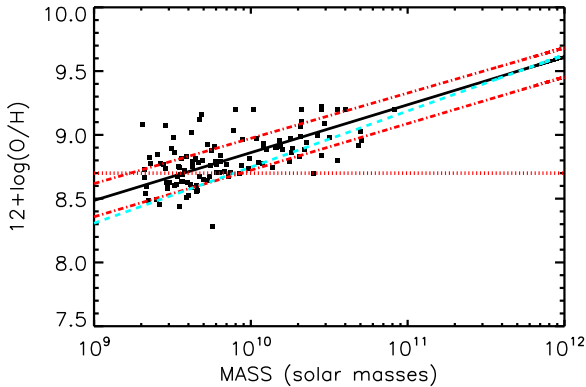


FIG. 25.— Metallicity based on the NH diagnostic ratio vs. galaxy mass for the sources in the low- z sample with $\text{EW}(\text{H}\alpha) > 12 \text{ \AA}$ computed for an ionization parameter of $q = 2 \times 10^7 \text{ cm s}^{-1}$ (*black squares*). The black solid line shows the least-square polynomial fit to the data. The red dash-dotted lines show the fits which would be obtained for $q = 4 \times 10^7 \text{ cm s}^{-1}$ (*upper line*) and $q = 10^7 \text{ cm s}^{-1}$ (*lower line*). The cyan dashed line shows the metallicity-mass relation derived from the extinction corrected N2O2 diagnostic ratio (Eq. 9). The red dotted horizontal line shows the solar metallicity.

In the figure we compare the metallicity-mass relation of Eq. 10 (*black solid line*) with the metallicity-mass relation of Eq. 9 (*cyan dashed line*) derived from N2O2. The agreement is reasonable given the sensitivity of the NH diagnostic to the ionization parameter. The mean metallicity in the 10^{10} to $10^{11} M_{\odot}$ range is 9.03 from NH and 8.99 from N2O2, which reassuringly shows that the metallicity and ionization parameter determinations are roughly self-consistent and that our treatment of the extinctions is plausible.

8.4. R23 Diagnostic Ratio

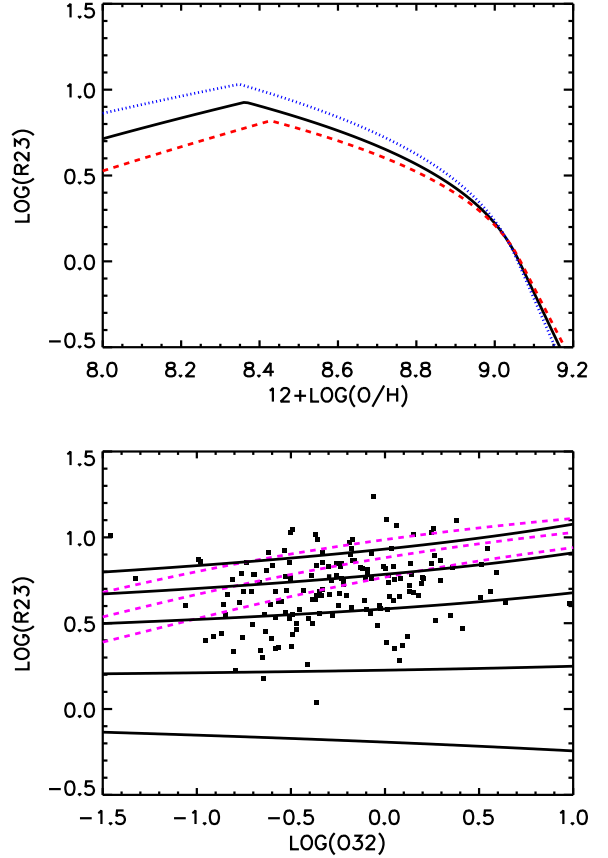


FIG. 26.— (a) Logarithmic R23 vs. metallicity for the McGaugh (1991) models corresponding to $\log(\text{O32}) = -1$ (*red dashed*), -0.25 (*black solid*), and 0.5 (*blue dotted*). These values cover the range of our data. (b) Logarithmic extinction corrected R23 vs. logarithmic extinction corrected O32 for the sources in the low- z sample with $\text{EW}(\text{H}\beta) > 4 \text{ \AA}$ and detected $[\text{O II}]$ (*black squares*). Tracks give the R23-O32 relations from McGaugh (1991): purple dashed lines show the relation on the low metallicity branch for three values of $12 + \log(\text{O}/\text{H})$ [8.0 (*lowest curve*), 8.2, and 8.4 (*highest curve*)], and solid black lines show the relation on the high metallicity branch for five values of $12 + \log(\text{O}/\text{H})$ [8.4 (*highest curve*), 8.6, 8.8, 9.0, and 9.1 (*lowest curve*)]. On the high metallicity branch there is little dependence of R23 on O32.

The R23 diagnostic ratio $[1.3 \times f([\text{O III}] \lambda 5007) + f([\text{O II}] \lambda 3727)]/f(\text{H}\beta)$ of Pagel et al. (1979) is one of the most frequently used metallicity diagnostics. It can be measured in our data out to $z = 0.9$. However, it is unfortunately multivalued with both a low metallicity and a high metallicity branch. Thus, the same value of R23 can correspond to two substantially different metallicities. Moreover, R23 is only weakly dependent on metallicity for $12 + \log(\text{O}/\text{H}) \lesssim 8.6$. We can see these traits in Figure 26. In Figure 26a we plot logarithmic R23 versus metallicity for the McGaugh (1991) models corresponding to $\log(\text{O32}) = -1$ (*red dashed*), -0.25 (*black solid*), and 0.5 (*blue dotted*). These cover the range of ionization dependent O32 measurements from our data, as can be seen from Figure 26b where we plot logarithmic extinction corrected R23 versus logarithmic extinction corrected O32 for the 164 sources in the low- z sample with $\text{EW}(\text{H}\beta) > 4 \text{ \AA}$ and detected $[\text{O II}]$ (*black squares*). Here we overlay the models of McGaugh (1991) for the low metallicity branch (*purple dashed*) and the high metallicity branch (*black*

solid) onto the data.

Unfortunately, much of the data in Figure 26b lie near the peak of the R23 ratio [$\log(\text{R23})$ in the range 0.5 to 1], where R23 is a relatively slowly varying function of the metallicity and where the metallicity could lie on either the upper or lower branches (see Fig. 26a). Fortunately, however, we can see from Figures 22 and 25 (where the metallicities were computed from N2O2 and NH, respectively) that the galaxies in the low- z sample with masses greater than $2 \times 10^9 M_\odot$ primarily lie on the high metallicity branch of the R23 diagnostic ratio [$12 + \log(\text{O}/\text{H}) > 8.4$] (see also KK04). In §9 we will assume that the higher redshift ($z > 0.475$) sources contained in the mid- z sample also predominantly lie on the high metallicity branch, though if there is significant metallicity evolution, this assumption could break down.

With most of the galaxies on the upper branch, the interpretation is considerably simplified, since on this branch there is very little dependence on O32. From the McGaugh (1991) models in Figure 26, we can see that at metallicities of $12 + \log(\text{O}/\text{H}) > 8.6$, the R23 parameter is nearly ionization independent and has a steep dependence on metallicity. We can therefore make a simple investigation of the metal evolution by analyzing the dependence of R23 on the NIR luminosity without considering O32. In Figure 27 we show the dependence of extinction corrected R23 on NIR luminosity for the low- z sample with $\text{EW}(\text{H}\beta) > 4 \text{ \AA}$ and detected [O II]. The median R23 is relatively flat at lower luminosities and then drops at the higher luminosity end. The least-square polynomial fit is

$$\log(\text{R23}) = 0.61 - (0.08 \pm 0.04) \log(L_N). \quad (11)$$

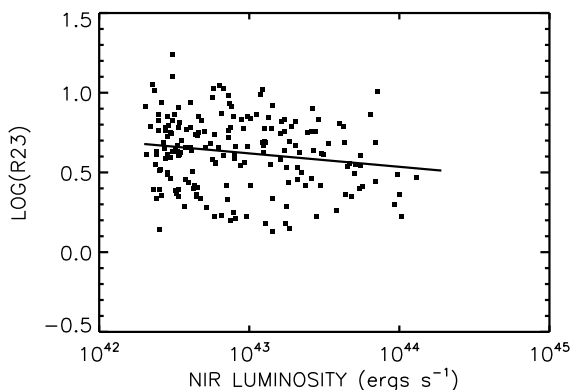


FIG. 27.— The extinction corrected R23 diagnostic ratio vs. NIR luminosity for the low- z sample with $\text{EW}(\text{H}\beta) > 4 \text{ \AA}$ and detected [O II] (*black squares*). The black solid line shows the least-square polynomial fit.

We can now also translate R23 and O32 to metallicity using the KK04 calibration (their Eq. 18), which is an average of the McGaugh (1991) and the KD02 R23 methods and is only valid for the upper branch. The dependence of the metallicity on the mass is then given by

$$12 + \log(\text{O}/\text{H}) = 8.77 + (0.23 \pm 0.05) \log(M_{10}), \quad (12)$$

which we show with a black solid line in Figure 28. Alternatively, we can translate R23 alone to $12 + \log(\text{O}/\text{H})$

using Equation 1 of Tremonti et al. (2004; hereafter, Tremonti04), which is an analytical fit to their R23-metallicity relation and is also only valid for the upper branch. In this case we find for the dependence of the metallicity on the mass

$$12 + \log(\text{O}/\text{H}) = 8.78 + (0.24 \pm 0.05) \log(M_{10}), \quad (13)$$

which has a very similar slope to Equation 12 and, over the mass range 10^{10} to $10^{11} M_\odot$, only differs in the intercept by 0.01 dex.

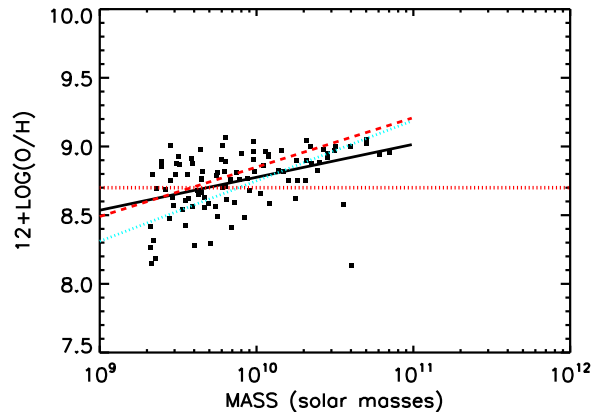


FIG. 28.— $12 + \log(\text{O}/\text{H})$ computed from the extinction corrected R23 and O32 diagnostic ratios using the KK04 calibration vs. galaxy mass for the low- z sample with $\text{EW}(\text{H}\beta) > 4 \text{ \AA}$ and detected [O II] (*black squares*). The black solid line shows the least-square polynomial fit (Eq. 12), which is flatter than the fits to the metallicities derived from the extinction corrected N2O2 diagnostic ratio (Eq. 9; *cyan dotted line*) and the NH diagnostic ratio (Eq. 10; *red dashed line*). The red dotted line shows the solar abundance.

In Figure 28 we compare the fit to the metallicities derived from R23 and O32 using the KK04 calibration (*black solid line*) with the metallicities derived from N2O2 (*cyan dotted line*) and NH (*red dashed line*). While the metallicities are close, using R23 gives a shallower slope, as can be seen quantitatively by comparing Equation 12 with Equations 9 and 10. The shallower slope is most likely a consequence of our assumption that the bulk of the sources lie on the high metallicity branch of R23. This assumption breaks down at the low mass end, causing some of the low metallicity branch points to be assigned artificially high metallicities.

We also calculated the values of the ionization parameter q from R23 and O32 using the new parameterizations of KK04 (their Eqs. 13 and 17) for the KD02 models. (Note that KK04 did not give a parameterization for q for their averaged KD02 and M91 R23 method, which we used to compute the metallicities in Figure 28. However, since q is not particularly sensitive to metallicity, the fact that we are using the updated KD02 parameterizations here to calculate the q values should not be important.) These q values are very similar to those derived from N2O2. The median $q = 2.3 \times 10^7 \text{ cm s}^{-1}$, and 80% of the sample lies between $q = 1.1 \times 10^7 \text{ cm s}^{-1}$ and $q = 4.4 \times 10^7 \text{ cm s}^{-1}$.

9. METALLICITIES IN THE EMISSION LINE GALAXIES: THE [OIII] SAMPLE

At higher redshifts only the R23 diagnostic ratio can be computed from the optical spectra. As can be seen

from Figure 26 (and as we discussed in §8.4), this results in some ambiguities in calculating the metallicities since R23 is relatively insensitive to metallicity at sub-solar values, and the translation from R23 to metallicity requires assumptions about which branch of the R23 relation the metallicity is on. We therefore first analyze the raw R23 evolution without making any translation to metallicity.

In Figure 29 we show the dependence of R23 on redshift for the mid- z sample with $\text{EW}(\text{H}\beta) > 4 \text{ \AA}$ and detected $[\text{O II}]$. We have divided the sample into three NIR luminosity intervals: (a) $(5 - 20) \times 10^{43} \text{ ergs s}^{-1}$; (b) $(2 - 5) \times 10^{43} \text{ ergs s}^{-1}$; and (c) $(0.8 - 2) \times 10^{43} \text{ ergs s}^{-1}$. The purple solid line shows the least-square polynomial fit to the data in (c). This same fit is also shown as a purple line in (a) and (b) for comparison with the fit to the data in each of those intervals (*black solid line*). In all three luminosity intervals we see a similar evolution with redshift, with R23 increasing by about 0.2–0.3 dex between $z = 0.3$ and $z = 0.9$. The parallel evolution of the three luminosity intervals indicates that the shape of the metallicity-mass relation does not evolve rapidly with redshift over this redshift range. This result is not changed if we exclude the strong redshift filament seen at $z = 0.85$. Since R23 decreases with increasing metallicity on the high metallicity branch (see Fig. 26a), we also see from Figure 29 that high luminosity galaxies have higher metallicities than lower luminosity galaxies at all redshifts. Moreover, in a given luminosity interval, the metallicity is increasing with decreasing redshift. The dependence of the metallicity on redshift is sufficiently strong that high luminosity galaxies at high redshifts have comparable metallicities to low luminosity galaxies at lower redshifts.

We may now compute the metallicity evolution with redshift and luminosity more directly at the expense of both assuming that the metallicity is on the upper branch of the R23 relation and adopting a specific calibration to metallicity. In Figure 30 we show $12 + \log(\text{O}/\text{H})$ computed from R23 and O32 in the same manner as in §8.4 using the KK04 calibration. The points are separated into the redshift intervals $z = 0.05 - 0.475$ (*red diamonds*) and $z = 0.475 - 0.9$ (*black squares*) with median redshifts of 0.44 and 0.75. Even over this relatively narrow redshift range the average metallicity has dropped by about 0.13 dex. Both distributions show an upper envelope of $12 + \log(\text{O}/\text{H}) \sim 9.1$. The spread to lower metallicities at the higher redshifts should not be taken seriously as it is a consequence of applying the high metallicity branch equation to galaxies that are on the low metallicity branch. We find the least-square polynomial fit to the metallicities, NIR luminosities, and $(1+z)$ values for all the galaxies together to be

$$12 + \log(\text{O}/\text{H}) = 8.95 + 0.18 \log(L_N) - 1.52 \log(1+z), \quad (14)$$

which we show in Figure 30 calculated at the median redshifts of 0.44 (*red solid*) and 0.75 (*black solid*), respectively. We also show the least-square polynomial fits to the metallicities and NIR luminosities for $z = 0.05 - 0.475$ (*red dashed*) and $z = 0.475 - 0.9$ (*black dashed*).

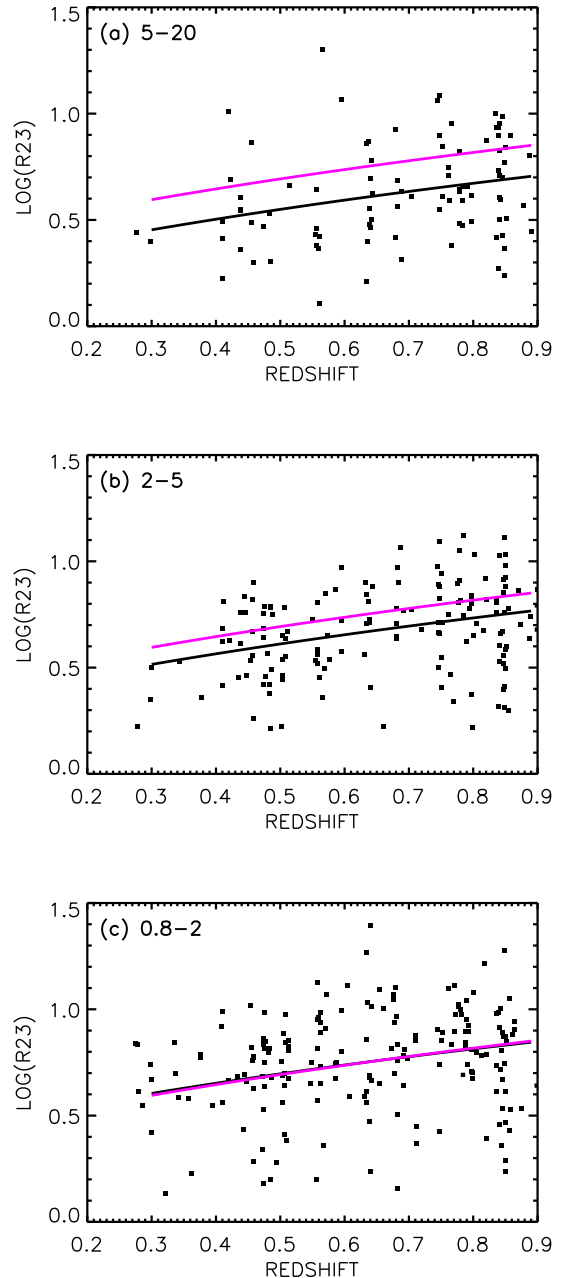


FIG. 29.— Logarithmic extinction corrected R23 vs. redshift for the mid- z sample with $\text{EW}(\text{H}\beta) > 4 \text{ \AA}$ and detected $[\text{O II}]$ for three NIR luminosity ranges: (a) $(5 - 20) \times 10^{43} \text{ ergs s}^{-1}$, (b) $(2 - 5) \times 10^{43} \text{ ergs s}^{-1}$, and (c) $(0.8 - 2) \times 10^{43} \text{ ergs s}^{-1}$. Each panel is marked with the luminosity range in units of $10^{43} \text{ ergs s}^{-1}$. In (a) and (b) the black solid line shows the least-square polynomial fit to $\log(\text{R23})$ vs. $\log(1+z)$. In (a), (b), and (c) the purple solid line shows the least-square polynomial fit to the data in (c).

Using the KK04 calibration, we find the least-square polynomial fit to the metallicities and masses for $z = 0.475 - 0.9$ to be

$$12 + \log(\text{O}/\text{H}) = 8.72 + (0.13 \pm 0.06) \log M_{10}. \quad (15)$$

Using the Tremonti04 calibration, we find

$$12 + \log(\text{O}/\text{H}) = 8.70 + (0.17 \pm 0.05) \log M_{10}. \quad (16)$$

These two fits only differ by an average of 0.02 dex over the $10^{10} - 10^{11} M_{\odot}$ range. Moreover, within the wide errors, the slopes of both fits are consistent with the slopes of the fits given in Equations 12 and 13, which were made to the low- z sample alone over the wider mass range using the KK04 and Tremonti04 calibrations, respectively. To show the similarity of the slopes for the two redshift intervals, in Figure 31 we plot Equations 12 (*red line*) and 15 (*black line*) on top of the $z = 0.05 - 0.475$ (*red diamonds*) and $z = 0.475 - 0.9$ (*black squares*) data restricted to masses above $10^{10} M_{\odot}$, where the mid- z sample is complete.

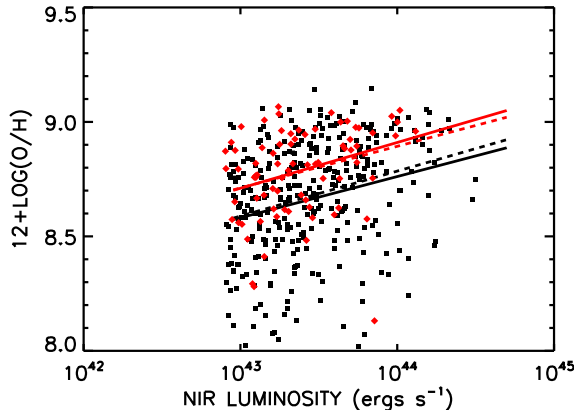


FIG. 30.— Metallicity vs. NIR luminosity for the mid- z sample computed from the extinction corrected R23 and O32 diagnostic ratios using the KK04 calibration. The red diamonds show the galaxies with $z = 0.05 - 0.475$. The black squares show the galaxies with $z = 0.475 - 0.9$. Both have an upper limit of about 9.1 for $12 + \log(\text{O}/\text{H})$. However, the mean metallicity has dropped by about 0.13 dex. The solid lines show the least-square polynomial fit to the metallicities, NIR luminosities, and $(1+z)$ values for all the galaxies together (Eq. 14) computed at the median redshifts (*red for 0.44*; *black for 0.75*). The dashed lines show the least-square polynomial fits to the metallicities and NIR luminosities for $z = 0.05 - 0.475$ (*red*) and $z = 0.495 - 0.9$ (*black*).

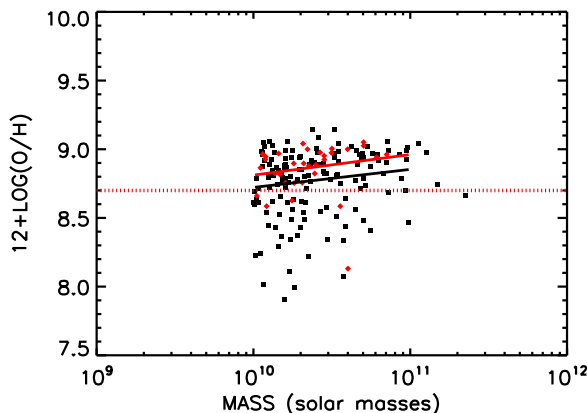


FIG. 31.— Metallicity vs. mass for the mid- z sample computed from the extinction corrected R23 and O32 diagnostic ratios using the KK04 calibration. The red diamonds show the galaxies with $z = 0.05 - 0.475$. The black squares show the galaxies with $z = 0.475 - 0.9$. The solid lines show the least-square polynomial fits to each redshift interval from Eq. 12 (*red line*) and Eq. 15 (*black line*).

We can more clearly compare the metallicities in the low- z and mid- z samples in histogram form. In Figure 32

we show the distribution of metallicities computed using the KK04 calibration for the galaxies in the $10^{10} - 10^{11} M_{\odot}$ range. The $z = 0.475 - 0.9$ ($z = 0.05 - 0.475$) interval is shown in black (red). The median metallicity in the mid- z (low- z) interval is 8.79 ± 0.03 (8.92 ± 0.04), where the errors give the 68% confidence range calculated using the median sign method. The increase of 0.13 dex in metallicity from median redshift 0.75 to median redshift 0.44 is consistent with that found from the fits to the larger luminosity selected sample in Equation 14.

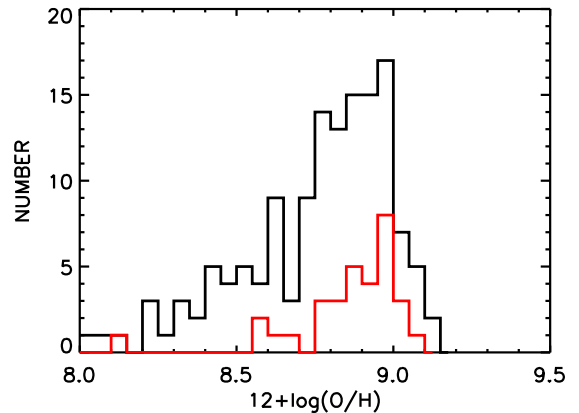


FIG. 32.— Distribution of metallicities computed from the extinction corrected R23 and O32 diagnostic ratios using the KK04 calibration for the galaxies in the mid- z sample with masses $10^{10} - 10^{11} M_{\odot}$. The black (red) histogram shows the distribution of galaxies between $z = 0.475 - 0.9$ ($z = 0.05 - 0.475$).

10. MISSING GALAXIES IN THE METALS ANALYSIS

The metals analysis of §8 and §9 only includes galaxies with strong emission lines, and this selection is a strong function of galaxy mass. In Figure 33 we show the fraction of galaxies with strong enough emission lines to have been included in that analysis versus logarithmic mass for $z = 0.05 - 0.475$ (*red diamonds*) and $z = 0.475 - 0.9$ (*black squares*). The fraction decreases smoothly with increasing logarithmic mass, falling to zero above $\sim 10^{11} M_{\odot}$, depending on the redshift interval.

We also show the relative contributions to the mass density versus logarithmic mass from all the galaxies in the redshift intervals $z = 0.05 - 0.475$ (*red histogram*) and $z = 0.475 - 0.9$ (*black histogram*). Combining this distribution with the fraction of galaxies in the strong emission line sample, we find that only about 20%–30% of the total galaxy mass density is included in the strong emission line metallicity analysis. It is therefore important to understand the evolution of the remaining galaxies if we are to understand fully the metallicity-mass evolution.

We can divide the galaxies excluded from the strong emission line metallicity analysis into two categories: apparently passive galaxies with no clear signs of ongoing star formation, and weakly active galaxies where the source has $\text{EW}(\text{H}\beta) < 4 \text{ \AA}$ and either $\text{EW}([\text{O II}]) > 5 \text{ \AA}$ or a $24 \mu\text{m}$ detection. In Figure 33 we show the fraction of non-strong emission line galaxies in the redshift intervals $z = 0.05 - 0.475$ (*red*) and $z = 0.475 - 0.9$ (*black*) that are weakly active (*solid curves*). This fraction is quite substantial. In fact, there are very few completely passive

galaxies below $\sim 3 \times 10^{10} M_{\odot}$ over the entire $z = 0.05 - 0.9$ redshift range. However, $\sim 40\%$ of the total galaxy mass density is contained in the passive population, and the majority of the massive galaxies ($> 10^{11} M_{\odot}$) fall into this category.

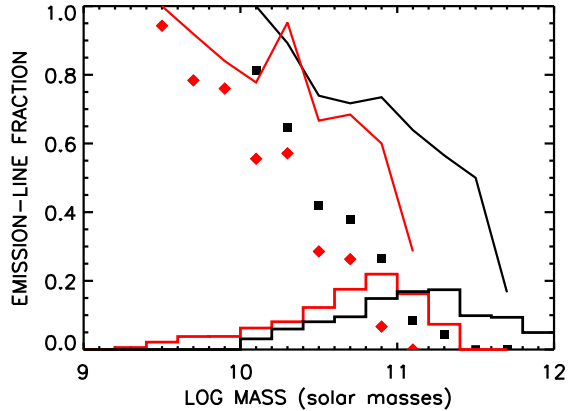


FIG. 33.— Fraction of galaxies in the redshift intervals $z = 0.05 - 0.475$ (red diamonds) and $z = 0.475 - 0.9$ (black squares) that are included in the strong emission line metallicity analysis of §8 and §9 vs. galaxy mass. The red (black) histogram shows the fraction of the mass density in each bin that comes from the galaxies in the redshift interval $z = 0.05 - 0.475$ ($z = 0.475 - 0.9$). The solid curves show the fraction of non-strong emission line galaxies in the redshift intervals $z = 0.05 - 0.475$ (red) and $z = 0.475 - 0.9$ (black) that are weakly active. In all cases we only show the fractions where there are more than 4 objects in the bin.

10.1. Passive Galaxies

We formed stacked spectra of the passive galaxies in each of the two redshift intervals by normalizing the flux calibrated spectra in the 3500 – 5000 Å range and then averaging the spectra. Regions around the atmospheric bands and the chip boundaries in the DEIMOS instrument were blanked out in the individual spectra.

In Figure 34a we show the stacked spectrum (black) for the redshift interval $z = 0.475 - 0.9$. We fitted the spectrum by assuming a range of metallicities and then found the best-fit BC03 model for each metallicity. Prior to measuring the χ^2 we removed slight shape differences by fitting a second-order polynomial to the ratio of the stacked spectrum to the model spectrum. Unfortunately, even in the stacked spectrum there is almost no distinction between fits with very different metallicities because of the metallicity-age degeneracy. In the case of the $z = 0.475 - 0.9$ stacked spectrum, the best-fit solar metallicity model is a single burst with an age of 1.9 Gyr (upper red spectrum). It closely matches the stacked spectrum. However, in Figure 34b we show the best-fit $2.5\times$ solar metallicity model, which is a single burst with an age of 1.0 Gyr (upper red spectrum). This fit is indistinguishable from the solar metallicity fit. In each panel we also show the residual (lower red spectrum) between the best-fit model and the stacked spectrum. There is very weak [O II] emission visible in the stacked spectrum but no H β or [O III], so there is no possibility of using the gaseous emission to estimate the metallicity.

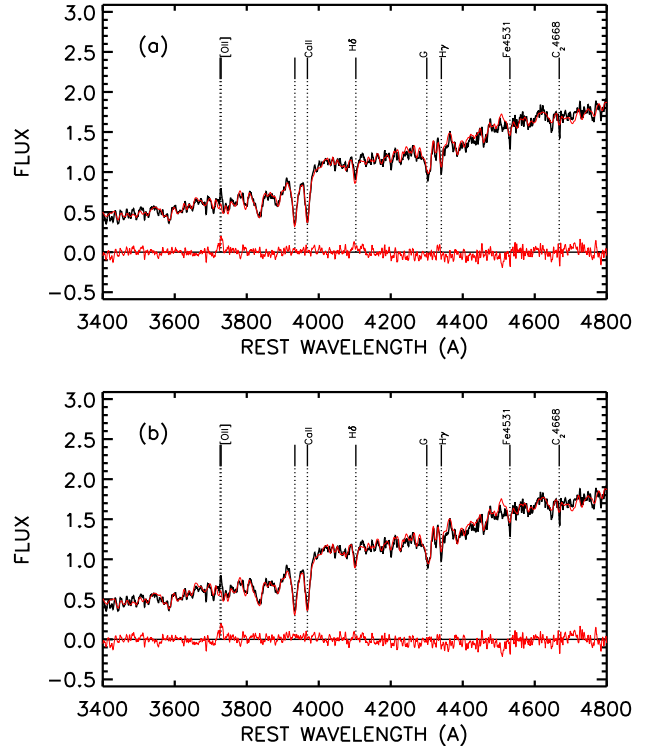


FIG. 34.— Stacked spectrum for passive galaxies in the redshift interval $z = 0.475 - 0.9$ formed by normalizing the individual extinction corrected spectra and averaging them (black in each panel). The upper red spectrum in (a) is the best-fit BC03 solar metallicity model, which is a single burst with an age of 1.9 Gyr. In (b) the upper red spectrum is the best-fit BC03 $2.5\times$ solar metallicity model, which is a single burst with an age of 1.0 Gyr. The overall shapes are matched by applying a second-order polynomial over the wavelength range. The lower red spectrum shows the residual difference between the data and the fit. The fits are both excellent and essentially indistinguishable.

10.2. Weakly Active Galaxies

In contrast to the stacked spectrum for the passive galaxies, the stacked spectrum for the weakly active galaxies clearly shows gaseous emission lines (see Fig. 35b). In this section we will derive metallicities from the stacked spectrum for the weakly active galaxies. However, to assess how well we are able to do this, we will also derive metallicities from the stacked spectrum for the strong emission line galaxies and compare with the metallicities that we obtained previously for the individual sources.

In Figure 35a we show the stacked spectrum (black) for the strong emission line galaxies [EW(H β) > 4 Å] in the redshift interval $z = 0.475 - 0.9$ and over the mass interval $10^{10.5} - 10^{11} M_{\odot}$. We overlay the best-fit BC03 solar metallicity model, which is exponentially declining with $\tau = 5$ Gyr and an age of 2.8 Gyr (upper red). (Note again that it does not matter what metallicity we adopt, as it would only affect the age.) We also show the residual spectrum (lower red) after subtracting the best-fit model from the stacked spectrum.

In Figure 35b we show the stacked spectrum (black) for the weakly active galaxies in the same redshift interval and over the same mass interval. We overlay the best-fit BC03

solar metallicity model, which is exponentially declining with $\tau = 5$ Gyr and an age of 7.5 Gyr (*upper red*). We again also show the residual spectrum (*lower red*).

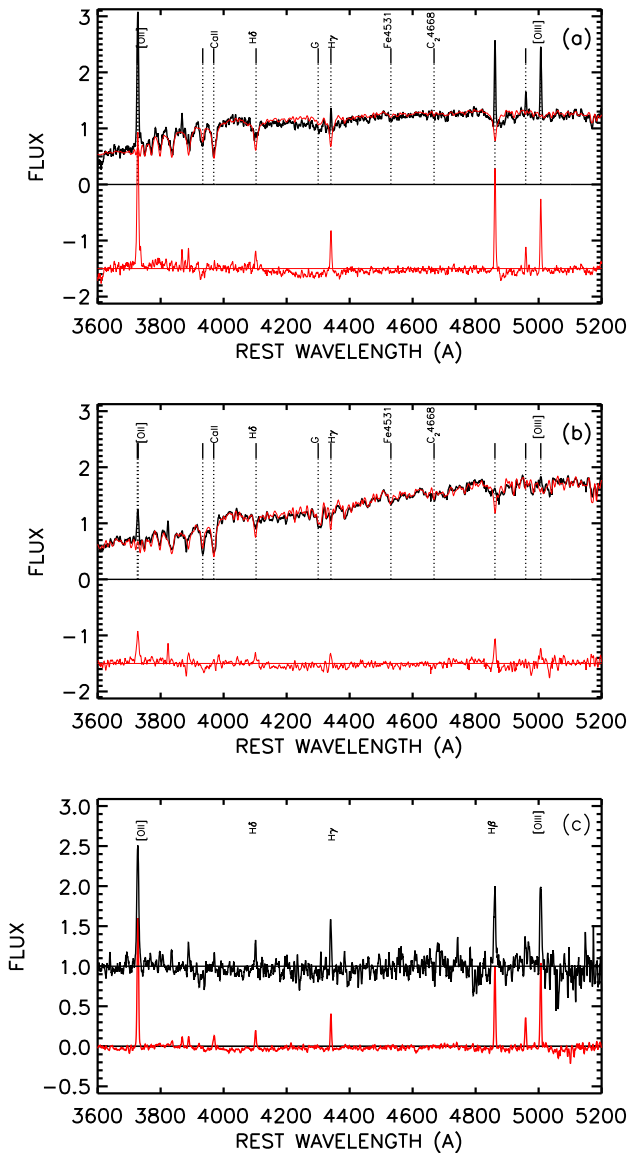


FIG. 35.— Stacked spectra for galaxies with $z = 0.475 - 0.9$ and masses $10^{10.5} - 10^{11} M_{\odot}$ formed by normalizing the individual extinction corrected spectra and averaging them. (a) Strong emission line galaxies with $EW(H\beta) > 4 \text{ \AA}$, all of which were included in the individual metallicity analysis (*black*). The upper red spectrum is the best-fit BC03 solar metallicity model, which is exponentially declining with $\tau = 5$ Gyr and has an age of 2.8 Gyr. (b) Weakly active galaxies with $EW(H\beta) < 4 \text{ \AA}$ and either $EW([OII]) > 5 \text{ \AA}$ or a $24 \mu\text{m}$ detection. The upper red spectrum is the best-fit BC03 solar metallicity model, which is exponentially declining with $\tau = 5$ Gyr and has an age of 7.5 Gyr. In (a) and (b) the lower red spectrum shows the residual difference between the data and the fit. (c) A direct comparison of the residual spectra from (a) (*red*) and (b) (*displaced black*). Both have been normalized to unity in the $H\beta$ line so that the strengths of the other lines may be directly compared. The measured R23 is 3.24 for the strong emission line galaxies and 5.62 for the weakly active galaxies.

In Figure 35c we show the two residual spectra normal-

ized to unity in the $H\beta$ line so that the strengths of the other lines may be directly compared.

We can make a rough analysis of the metallicities in the stacked spectra using the R23 method. The high degree of homogeneity we saw earlier in the ionization parameters and in the metallicities at a given mass gives us some confidence that this procedure may work reasonably well in analyzing the ensemble of galaxies. The assumptions are similar to those we made to determine the metallicities for the individual galaxies: namely, that the metallicity determined from the composite spectrum of H II regions in the galaxy roughly matches the average metallicity that would be derived from an independent analysis of the individual H II regions in the galaxy. In general this type of averaging results in a small underestimate (by about 0.1 dex) in the derived oxygen abundance for the individual galaxies (Kobulnicky et al. 1999).

In Figure 36 we compare the metallicities derived from the stacked spectrum for the strong emission line galaxies (using the Tremonti04 calibration) (*solid symbols*) with the best fits to the metallicities of the individual galaxies (*solid lines*) from Equations 13 and 16 (which also use the Tremonti04 calibration). The red (black) color denotes the $z = 0.05 - 0.475$ ($z = 0.475 - 0.9$) interval. We use the Tremonti04 calibration so that we may compare the results directly with the local measurements in §11. The lower redshift points are in good agreement with the fit to the individual measurements, while the higher redshift points are about 0.1 dex higher on average. The open red (black) symbols show the measurements from the weakly active galaxies for the redshift interval $z = 0.05 - 0.475$ ($z = 0.475 - 0.9$). These show substantial scatter, but the measurements are in broad agreement with the strong emission line galaxies. We will assume in §11 that the weakly active galaxies parallel the evolution of the strong emission line galaxies.

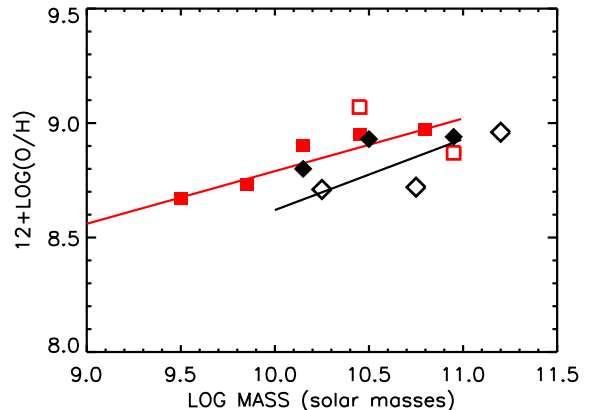


FIG. 36.— Metallicities derived from either the stacked spectrum for the strong emission line galaxies (*solid symbols*) or the stacked spectrum for the weakly active galaxies (*open symbols*) vs. logarithmic galaxy mass for the redshift intervals $z = 0.05 - 0.475$ (*red*) and $z = 0.475 - 0.9$ (*black*). All metallicities were computed with the Tremonti04 calibration. The solid lines show the fits to the individual galaxies in the strong emission line sample using the Tremonti04 calibration [Eq. 13 (*red*) and Eq. 16 (*black*)].

We now bring together the results from the previous sections to form an integrated picture of galactic stellar mass assembly, star formation, and metallicity evolution. In §11.1 and §11.2 we measure the galactic stellar mass functions and the growth of the stellar mass densities with redshift. In §11.3 we measure the star formation rate densities as a function of redshift and galaxy mass. In §11.4 we compute the expected formed stellar mass density growth rates produced by star formation and show that they match those measured from the formed stellar mass functions if the IMF is slightly increased from the Salpeter IMF at intermediate masses ($\sim 10 M_{\odot}$). In §11.5 we determine the instantaneous specific star formation rates, which give a quantitative description of the range of behaviors in the galaxies. We show that only galaxies below about $10^{11} M_{\odot}$ are growing substantially over $z = 0.05 - 1.5$. In §11.6 we analyze the distributions of galaxy colors, equivalent widths, and 4000 Å break strengths and find that star formation in all but the lowest mass galaxies in our sample is occurring in bursts with characteristic time intervals of about 4×10^9 yr. We also find that most of the growth in the mass density is in the red sequence galaxies, whether these are chosen by color or from the rest-frame EW([O II]). In §11.7 we show that as the redshift decreases, the galaxy types smoothly migrate from spirals to S0s and elliptical galaxies at all masses. The mass build-up is primarily in the E/S0 galaxies, which are also the red sequence galaxies, and there is little change in the galactic stellar mass function of the spirals. In §11.8 we find that although the masses are a strongly increasing function of environment, there is little redshift dependence in this relation. Unlike local results, the fraction of galaxies in the red sequence shows little environmental dependence and appears to depend primarily on the galaxy mass. Finally, in §11.9 we compare the metallicity evolution in the present sample with local and high-redshift metallicity measurements. In §11.10 we combine the measured increases in metallicity with redshift with the metals returned from the measured SFRs to make a crude estimate of the galaxy gas mass reservoir, and we compare this to the stellar mass density as a function of galaxy mass.

11.1. Galactic Stellar Mass Functions

In Figure 37 we show the galactic stellar mass functions (*black squares*) in three redshift intervals [(a) $z = 0.9 - 1.5$, (b) $z = 0.475 - 0.9$, and (c) $z = 0.05 - 0.475$] computed using the $1/V$ methodology (Felten 1976) and compared with the local mass function of Cole01 adjusted to the present cosmology (*purple crosses*). Both the Cole01 and our own mass functions are computed with the Salpeter IMF assumed throughout.

For each mass function we have computed the errors in two ways. First, we assigned 1σ errors based on the number of sources in each bin (*red error bars*). These errors dominate at the high-mass end where there are small numbers of sources in each bin. Second, we estimated the effect of cosmic variance in a simple empirical way. In each redshift interval we eliminated the strongest redshift sheet from the sample. For example, in the $z = 0.475 - 0.9$ redshift interval we removed all of the sources lying between $z = 0.845$ and $z = 0.86$ (see Figure 10). Typically the strongest single sheet will contain about 10%–20% of the galaxies in the redshift interval. We then recomputed

the mass function corresponding to the new volume and used the difference as an error estimate (*black error bars*). These error estimates dominate at the low-mass end. The internal error estimate from this method are similar in size to the analytic estimates of Somerville et al. 2004 which would give systematic error of 0.25, 0.15 and 0.1 dex in the $z = 0.05 - 0.475$, $z = 0.475 - 0.9$ and $z = 0.9 - 1.5$ redshift intervals.

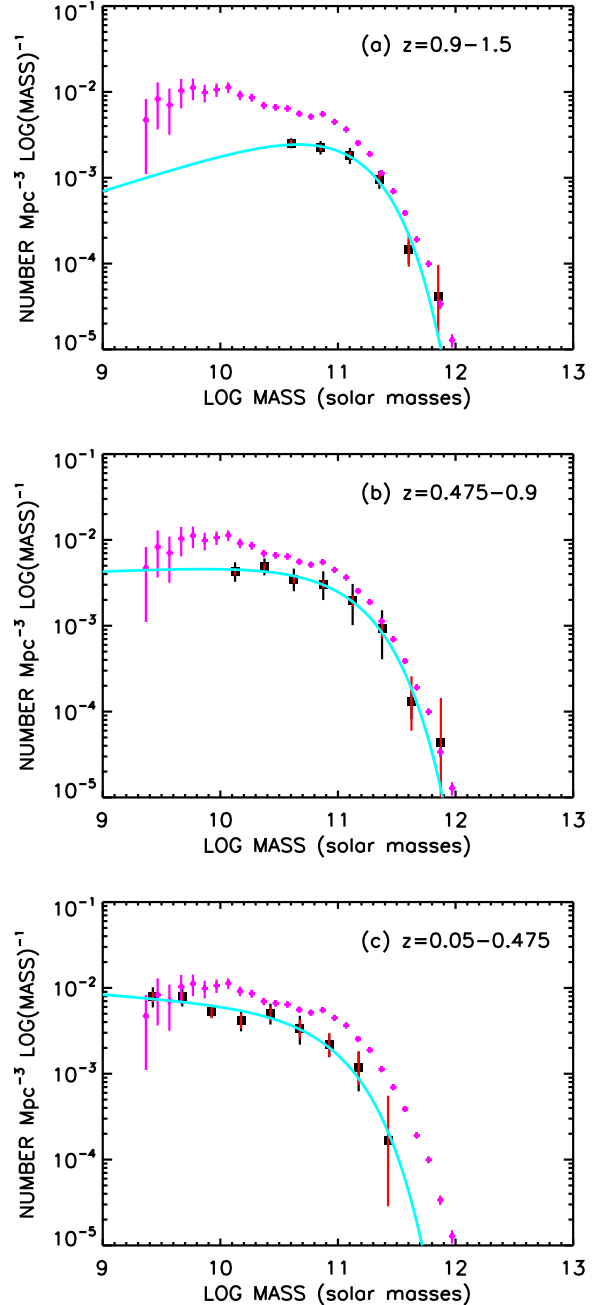


FIG. 37.— Galactic stellar mass functions in the redshift intervals (a) $z = 0.9 - 1.5$, (b) $z = 0.475 - 0.9$, and (c) $z = 0.05 - 0.475$ (*black squares*). The red error bars are 1σ , based on the number of sources in each bin, while the black error bars are derived from excluding the strongest velocity sheet in each redshift interval (see text for details). The purple crosses and associated 1σ error bars are the same in all three redshift intervals and show the local mass function of Cole01 for the Salpeter IMF adjusted to the present cosmology. The cyan curves show the best-fit Schechter functions obtained using the Sandage et al. (1979) maximum likelihood method.

In order to provide parametric fits to the data, we have assumed a Schechter (1976) form,

$$\phi(M) = \phi_* \left(\frac{M}{M_*(z)} \right)^{\alpha(z)} \frac{e^{-M/M_*(z)}}{M_*(z)}, \quad (17)$$

for the mass function, where $\phi(M)$ is the number of galaxies per unit mass per Mpc^3 at mass M . We used the Sandage et al. (1979) maximum likelihood method to determine the power-law index $\alpha(z)$ and the characteristic mass $M_*(z)$ for each of the three redshift intervals. The best-fit functions are shown in Figure 37 (*cyan curves*), and the derived α and M_* for each redshift interval are shown in Figure 38 together with the 68% and 95% confidence error ellipses. We obtained the normalizations $\phi_*(z)$ by normalizing to the number of objects in each redshift interval. We used our variance estimates (which dominate the error budget) in computing the error on this quantity. We summarize the maximum likelihood fits in each redshift interval in Table 1, together with the 68% confidence ranges.

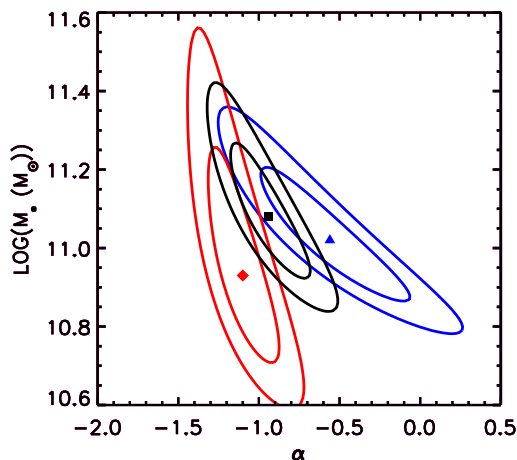


FIG. 38.— Sandage et al. (1979) fits to $\alpha(z)$ and $M_*(z)$ for the three redshift intervals $z = 0.05 - 0.475$ (*red diamond*), $z = 0.475 - 0.9$ (*black square*), and $z = 0.9 - 1.5$ (*blue triangle*). In each case the inner contour shows the 68% confidence range and the outer contour shows the 95% confidence range for the symbol of the same color.

A number of analyses of galactic stellar mass functions have recently been undertaken (see references in §1), and our results are broadly consistent. We may make the most straightforward comparison with Fontana et al. (2006; hereafter Fontana06), who analyze their data in a very similar way and who also use the Salpeter IMF. While their GOODS-MUSIC sample relies heavily on photometric redshifts, in other respects it is comparable to the present sample. Their Figure 4 bears a striking resemblance to our Figure 37. Conselice07 use a much larger field size with almost twenty times as many objects and also draw a similar conclusion. The agreement between fields is reassuring that our results are robust and are not being dominated by cosmic variance.

The effects of downsizing can be clearly seen in both Fontana06’s Figure 4 and our Figure 37: the galaxy number densities at the low-mass end are still rising down to the lowest redshift interval, while the number densities at

the high-mass end ($> 10^{11} M_\odot$) are changing much more slowly over $z = 0.05 - 1.5$.

Over this redshift range Fontana06 find a relatively invariant $\alpha(z) \sim -1.2$, but their $M_*(z)$ rises by about 0.12 dex from $z = 0$, where $\log M_* = 11.16$ from Cole01, to $z = 1.35$. Our $\alpha(z)$ values are slightly greater than this, though consistent with a constant $\alpha(z) = -1.2$ within the 2σ errors (see Fig. 38). Our slightly greater $\alpha(z)$ values are a consequence of Fontana06 having a turn-up at the low-mass end (see their Fig. 4). It is quite likely that this is a result of their use of photometric redshifts, which are more problematic for low-mass galaxies because such galaxies are predominantly blue and harder to fit, but it could also be a measure of the cosmic variance.

However, we do see a significant evolution in the mean mass (a rise in either M_* or α with increasing redshift) in our data. In particular, the fitted values in the highest redshift interval are not consistent at the 3σ level with those in the lowest redshift interval (see Fig. 38). We can see this evolution most clearly by adopting a fixed $\alpha(z) = -1.18$ from the local Cole01 fit and computing $M_*(z)$ for this fixed slope. This is given as the final column in Table 1, and it shows a rise of about 0.12 dex between $z = 0$ (Cole01) and our highest redshift interval, an identical result to that of Fontana06.

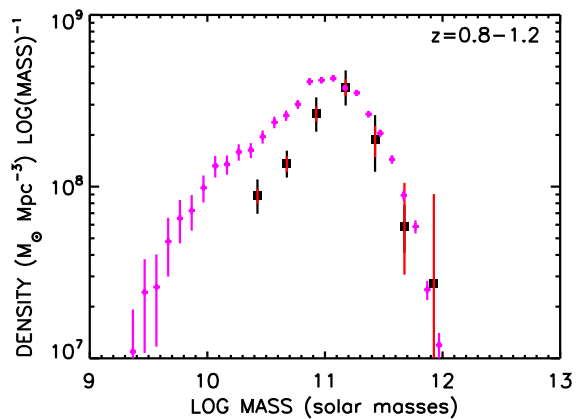


FIG. 39.— Stellar mass density per logarithmic galaxy mass interval in the redshift range $z = 0.8 - 1.2$ (*black squares*) compared with the local distribution from Cole01 (*purple crosses*). The error bars are as in Figure 37.

The change in $M_*(z)$ is a numerical consequence of the build-up of the low-mass region of the galactic stellar mass function relative to the high-mass region. In Figure 39 we compare the stellar mass density per logarithmic galaxy mass interval in the redshift range $z = 0.8 - 1.2$ (*black squares*) with that from Cole01 locally (*purple crosses*). Both distribution functions are strongly peaked with most of the mass density lying in galaxies with masses close to the peak value. However, the Cole01 function is broader and extends to lower masses.

The peak of the mass density per logarithmic galaxy mass, $M_*(z)(2\alpha(z) + 1)$, provides an alternative way to characterize the Schechter function (see Baldry et al. 2006). The evolution of the peak is better defined than the evolution of either $\alpha(z)$ and $M_*(z)$ separately. The location of the peak increases from $11.07 \pm 0.01 M_\odot$ in Cole01 and 10.88 ($10.77 - 11.09$) M_\odot in our lowest redshift

shift interval to $11.18 \pm 0.03 M_{\odot}$ in our highest redshift interval.

11.2. Stellar Mass Density Growth with Redshift

In Figure 40 we plot the stellar mass density versus redshift for various mass intervals. In both panels we use black solid squares and 68% confidence limits to show the mass density evolution for all of the galaxies in our sample above $10^{10.5} M_{\odot}$. We also obtained the local mass density above $10^{10.5} M_{\odot}$ by integrating the Cole01 function. We denote this by a black open square, which we show extended to all redshifts (*black dashed line*) for ease of comparison. $10^{10.5} M_{\odot}$ is the lowest mass to which we can measure the mass density over our entire $z = 0.05 - 1.5$ redshift range.

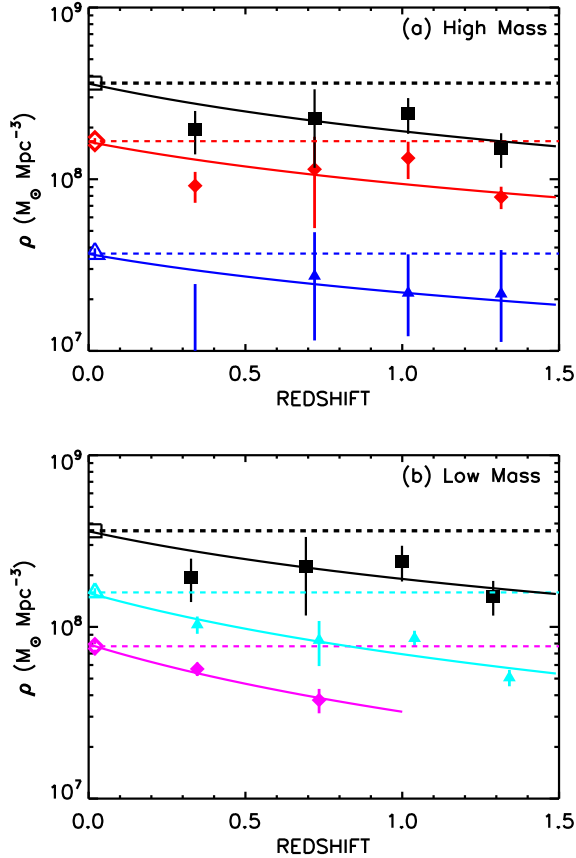


FIG. 40.— Universal stellar mass density vs. redshift. In both panels the black solid squares show the evolution of the mass density for all sources above $10^{10.5} M_{\odot}$, and the black open square (and black dashed line) shows the local mass density above $10^{10.5} M_{\odot}$ obtained by integrating the Cole01 function. (a) The evolution in the mass intervals $10^{11.5} - 10^{12} M_{\odot}$ (*blue triangles, highest-mass interval*) and $10^{11} - 10^{11.5} M_{\odot}$ (*red diamonds, high-mass interval*). (b) The evolution in the mass intervals $10^{10.5} - 10^{11} M_{\odot}$ (*cyan triangles, intermediate-mass interval*) and $10^{10} - 10^{10.5} M_{\odot}$ (*purple diamonds, low-mass interval*). The low-mass interval is only shown at $z < 0.9$ where it is complete. Errors are the maximum of the numerical and variance errors discussed in the text. The least-square polynomial fits of $\log \rho$ vs. $\log(1+z)$ are shown with the solid curves. The local mass densities for each of the mass intervals obtained by integrating the Cole01 function (*open symbols, color corresponds to the mass interval*) are also shown extended to all redshifts (*dashed lines*).

In Figure 40a we show the mass density evolution for two high-mass intervals: $10^{11.5} - 10^{12} M_{\odot}$ (*blue triangles;*

hereafter, our highest-mass interval) and $10^{11} - 10^{11.5} M_{\odot}$ (*red diamonds; our high-mass interval*). In Figure 40b we show the mass density evolution for two lower mass intervals: $10^{10.5} - 10^{11} M_{\odot}$ (*cyan triangles; our intermediate-mass interval*) and $10^{10} - 10^{10.5} M_{\odot}$ (*purple diamonds; our low-mass interval*). We show the evolution in the low-mass interval only to $z = 0.9$ where the sample is complete. We obtained the local mass density for each of the mass intervals by integrating the Cole01 function over those intervals (*open symbols*). For ease of comparison, we show those local mass densities extended to all redshifts (*dashed lines*).

Locally almost equal mass densities lie in the high (*open red diamond in Fig. 40a*) and intermediate (*open cyan triangle in Fig. 40b*) mass intervals. However, the high-mass interval material is changing more slowly than the intermediate-mass interval material, which is growing smoothly over the whole $z = 0.05 - 1.5$ range. The low-mass interval material is also growing smoothly over $z = 0.05 - 0.9$. The highest-mass interval material has a slow evolution (and indeed is consistent with having no evolution) over the entire $z = 0.05 - 1.5$ range, though the error bars are large and the amount of material contained in this mass interval is small.

The mass-sliced data may be most easily compared with Conselice07, who present their data in a similar way. While the Conselice07 sample is a large one (almost 50,000 objects), the data are not of the same quality as that in Fontana06 or in the present paper. Only about 22% of their sample have spectroscopic redshifts from the DEEP2 observations, and their photometric redshifts were calculated using only 4 (*BRIK*; half the sample) or 5 (*BRIJK*) band colors. These are too few colors to get reliable measurements of all of the desired quantities (i.e., extinction, photometric redshifts, mass, age/metallicity, and evolutionary model). For comparison, recall that over the redshift range $z = 0.05 - 1.5$ we have spectroscopic redshifts for 84% of the galaxies in our uniform NIR flux-limited sample (see §2.2). Moreover, for the very small fraction of sources where we used photometric redshifts, they were derived from 13 band colors (*UBVRIz'JHK_s* and the four *Spitzer* IRAC bands). Fontana06 used 14 band colors to determine their predominantly photometric redshifts.

Despite these limitations, the agreement is good. We can compare our Figure 40 with Figure 4 of Conselice07 if we convert our stellar masses and stellar mass densities to the Chabrier (2003) IMF used by Conselice07 by dividing by 1.70, as discussed in §1. Our results extend to lower masses than Conselice07 since our NIR sample is deeper. However, if we compare the region of mass and redshift where the two studies overlap, then we find good agreement between the two results in both absolute value and shape. Both analyses show slow growth at the higher masses and more rapid growth at the lower masses. The one quantitative difference is that we do not reproduce the sharp drop in the mass density which Conselice07 see in their $10^{11} - 10^{11.5} M_{\odot}$ interval above $z = 1.2$. It is not clear whether this is simply a result of cosmic variance (neither of the surveys are large enough for cosmic variance not to matter), or whether it is related to Conselice07's use of 4 or 5 band photometric redshifts. Since the present work is based on a much deeper and far more spectroscopically complete sample than that of Conselice07, our

results should be more reliable if this is the explanation.

In order to quantify the results of Figure 40, we made least-square polynomial fits to the logarithmic stellar mass densities [including the local values obtained by integrating the Cole01 function] versus the logarithmic cosmic time. We show these in Figure 40 with solid curves. For the total mass above $10^{10.5} M_{\odot}$ we find

$$\log \rho_*(> 10.5 M_{\odot}) = 8.56 + (0.73 \pm 0.16) \log(t/t_0), \quad (18)$$

and for the mass intervals we find

$$\log \rho_*(10^{10} - 10^{10.5} M_{\odot}) = 7.89 + (1.11 \pm 0.28) \log(t/t_0), \quad (19)$$

$$\log \rho_*(10^{10.5} - 10^{11} M_{\odot}) = 8.20 + (0.95 \pm 0.10) \log(t/t_0), \quad (20)$$

$$\log \rho_*(10^{11} - 10^{11.5} M_{\odot}) = 8.22 + (0.65 \pm 0.12) \log(t/t_0), \quad (21)$$

$$\log \rho_*(10^{11.5} - 10^{12} M_{\odot}) = 7.57 + (0.59 \pm 0.37) \log(t/t_0). \quad (22)$$

The fit for Equation 19 is over the $z = 0.05 - 0.9$ redshift range, while the remaining fits are over the $z = 0.05 - 1.5$ range. The low-mass ranges ($< 10^{11} M_{\odot}$) are growing approximately linearly with time, while the high-mass ranges are growing more slowly. Thus, the low-mass galaxies have roughly constant stellar mass density growth rates, and it is the drop in the growth rates in the high-mass galaxies that is responsible for the overall drop in the growth rates seen in Equation 18.

We also computed the total stellar mass density evolution by integrating to the limiting mass in each redshift interval and extrapolating to estimate the contribution from lower mass galaxies. This correction is not large since the total mass density is dominated by galaxies near $M_*(z)$. Locally about 72% of the mass density lies in galaxies above $10^{10.5} M_{\odot}$ and about 89% in galaxies above $10^{10} M_{\odot}$. If we use our best-fit Schechter function, then in the $z = 0.9 - 1.5$ interval about 88% of the mass density lies in galaxies above $10^{10.5} M_{\odot}$ and about 97% in galaxies above $10^{10} M_{\odot}$. If we instead force-fit to $\alpha = -1.18$, then the percentages are 77% and 91%, respectively. When we include these corrections, the total stellar mass density has a slightly steeper dependence on redshift than does the mass density above $10^{10.5} M_{\odot}$. Using, respectively, our best-fit Schechter function and the fit where α is forced to -1.18 , we find

$$\log \rho_*(\text{total}) = 8.77 + (0.91 \pm 0.15) \log(t/t_0), \quad (23)$$

and

$$\log \rho_*(\text{total}) = 8.77 + (0.80 \pm 0.15) \log(t/t_0). \quad (24)$$

11.3. Star Formation History

We tested our empirical SFR calibrations (§7.1) by calculating the universal SFH from $z = 0.05 - 1$ for all of the galaxies in our NIR sample. We show this in Figure 41, where we use red open (solid) squares to denote the star formation rate densities (SFRDs) calculated from the $H\beta$ (UV) luminosity densities after applying our extinction corrections. As is well known, the extinction corrections are substantial, typically factors of five in the various redshift bins. At $z = 0.9$ about 80% of the light is dust

reradiated. Our extinction corrected values at $z > 0.3$ agree broadly with the many measurements in the literature (see the references in §1). We explicitly compare with the values derived from radio and submillimeter data from the stacking analysis of Wang et al. (2006) (*black squares*). These should be a good measure of the total star formation history, including highly-obscured sources. The good agreement suggests that we are seeing most of the higher redshift star formation in our present sample.

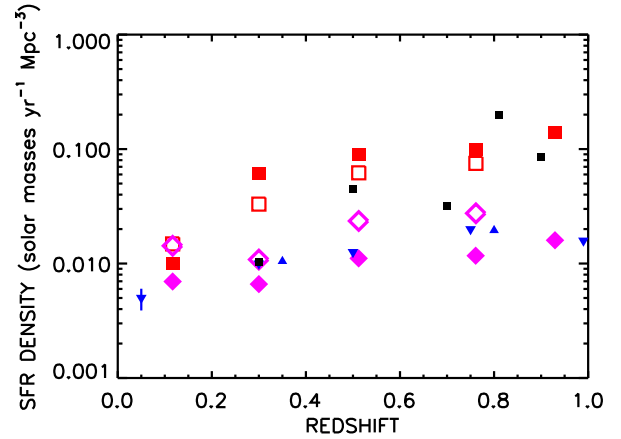


FIG. 41.— Star formation histories calculated from the rest-frame $H\beta$ (*open*) and UV (*solid*) luminosity densities of the NIR sample using the calibrations of §7.1. The red symbols show the extinction corrected SFRDs. The purple symbols show the extinction uncorrected SFRDs. The black solid squares were derived by Wang et al. (2006) from radio and submillimeter data and agree well with our extinction corrected values. The blue symbols show the SFRDs directly seen at rest-frame UV wavelengths for UV selected galaxies. We only show the *GALEX* determinations of Wyder et al. (2005; local) and Schiminovich et al. (2005) (*downward pointing triangles*) and the ground-based determinations of Wilson et al. (2002) (*upward pointing triangles*), since these are the most accurate measurements near $z = 1$. All agree reasonably well with our extinction uncorrected values. The formal errors are mostly smaller than the symbol sizes.

However, the SFRDs from the NIR sample drop steeply at lower redshifts. At these lower redshifts most of the star formation is instead seen as direct UV emission from lower mass galaxies, which have very small extinctions. Thus, in Figure 41 we also show the SFRDs derived from our extinction uncorrected data. Here we use purple open (solid) diamonds to denote the SFRDs calculated from the $H\beta$ (UV) luminosity densities. Since the extinction correction is smaller at $H\beta$, the $H\beta$ points lie above the UV points. We can compare the UV data with the literature results for rest-frame UV flux measurements of UV selected galaxies (*blue symbols*), such as the ground-based observations of Wilson et al. (2000) (*upward pointing triangles*) and the more recent *GALEX* determinations of Wyder et al. (2005; local) and Schiminovich et al. (2005) (*downward pointing triangles*). We again find close agreement.

In Figure 42 we show our extinction corrected SFRDs (*red squares*) calculated from the rest-frame UV luminosity densities versus redshift for the mass intervals (a) $10^{10} - 10^{10.5} M_{\odot}$, (b) $10^{10.5} - 10^{11} M_{\odot}$, (c) $10^{11} - 10^{11.5} M_{\odot}$, and (d) $10^{11.5} - 10^{12} M_{\odot}$. As another check of our UV extinction corrections, we also show the SFRDs (*blue diamonds*) obtained by adding those computed from the $24 \mu\text{m}$ fluxes for the obscured star formation with those

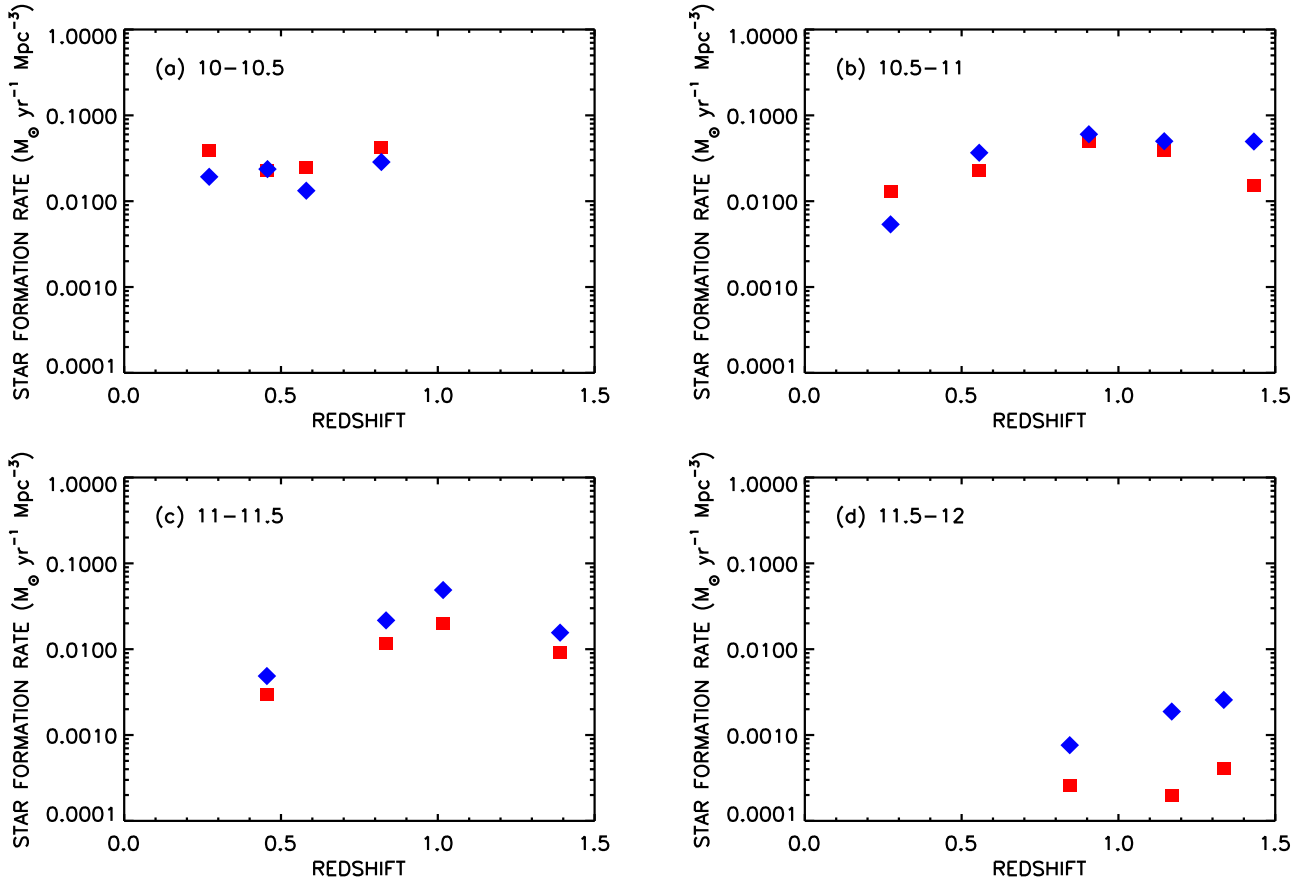


FIG. 42.— Star formation rate densities from two different methods vs. redshift for the mass intervals (a) $10^{10} - 10^{10.5} M_{\odot}$, (b) $10^{10.5} - 10^{11} M_{\odot}$, (c) $10^{11} - 10^{11.5} M_{\odot}$, and (d) $10^{11.5} - 10^{12} M_{\odot}$. The red squares show the extinction corrected SFRDs calculated from the UV luminosity densities using our empirical calibrations. The blue diamonds show the completely independent calculation of the SFRDs from the 24 μm fluxes and the extinction uncorrected [O II] fluxes.

computed from the extinction uncorrected [O II] luminosities for the unobscured star formation (see Conselice07). This method has no dependence on the UV extinction corrections and shows extremely similar results to the UV-based method.

In Figure 43 we show our UV-based extinction corrected SFRDs per unit logarithmic mass versus the logarithmic mass in the redshift intervals $z = 0.05 - 0.475$ (*red diamonds*), $z = 0.475 - 0.9$ (*black squares*), and $z = 0.9 - 1.5$ (*blue triangles*). In each redshift interval we only show the SFRDs over the mass range where the NIR sample is complete. Just for a shape comparison, we also show on the figure the stellar mass density distribution function for $z = 0.475 - 0.9$ divided by the age of the universe at $z = 0.7$ (*black curve*). The contrast between this and the SFRD distribution is striking, with the latter being much more strongly weighted to low-mass galaxies. At all redshifts there is very little star formation at masses $> 10^{11.1} M_{\odot}$, but at high redshifts the star formation peaks in the interval $10^{10.5} - 10^{11.1} M_{\odot}$. It is the drop in star formation for galaxies in this mass interval that results in the drop in the overall SFH. At lower masses there is relatively little change over $z = 0.05 - 0.9$.

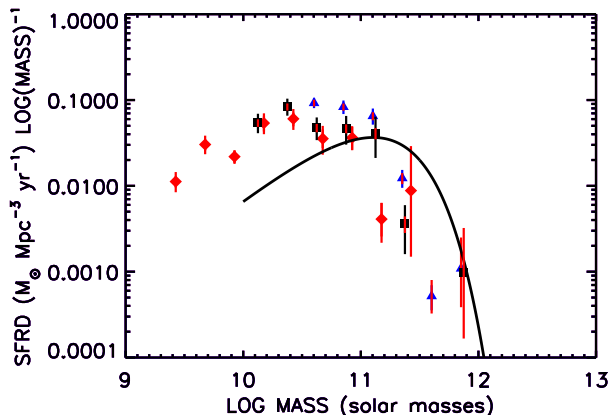


FIG. 43.— Extinction corrected star formation rate density per unit logarithmic mass vs. logarithmic mass in the redshift intervals $z = 0.05 - 0.475$ (*red diamonds*), $z = 0.475 - 0.9$ (*black squares*), and $z = 0.9 - 1.5$ (*blue triangles*). The solid black curve shows the corresponding shape of the stellar mass density distribution function for $z = 0.475 - 0.9$ divided by the age of the universe at $z = 0.7$.

11.4. Comparison of Growth Rates

In this section we want to compare the stellar mass density growth rates produced by star formation with those measured from the stellar mass functions. Other groups have made this comparison before (e.g., Borch et al. 2006; Pérez-González et al. 2008), but generally they have not done so by mass interval, nor have they done it self-consistently, since they rely on other groups' determinations of the star formation. Thus, they have to assume that the galaxies producing the star formation have masses in the same range as the galaxies in their stellar mass function analysis. A comparison by mass interval is a much more powerful way to analyze this type of data.

First, to obtain the growth rates from the stellar mass functions, we took the derivative of the least-square polynomial fits of Equations 19–22 after multiplying the mass

densities by the average correction of 1.35 given in §1 to convert to formed stellar mass densities (i.e., the total mass density formed into stars prior to stellar mass loss; it is the formed mass density growth rates which are directly related to the SFRDs). We show these growth rates (*purple solid lines*) in Figure 44 versus redshift for the mass intervals (a) $10^{10} - 10^{10.5} M_{\odot}$, (b) $10^{10.5} - 10^{11} M_{\odot}$, (c) $10^{11} - 10^{11.5} M_{\odot}$, and (d) $10^{11.5} - 10^{12} M_{\odot}$.

Next, to compute the expected formed stellar mass density growth rates produced by star formation, we need to allow for the fact that the mass of a galaxy will grow as it forms stars. Consequently, the mass that formed in one mass interval will eventually end up in another mass interval. We can describe this movement with the conservation equation

$$\dot{\rho}(M) = s(M) - \frac{d}{dM}(\dot{M}\rho(M)), \quad (25)$$

where $\rho(M)$ is the stellar mass density per unit mass interval and $s(M)$ is the SFRD per unit mass interval. Since \dot{M} is related to $s(M)$ through $\dot{M} = s(M)/\phi(M)$, where $\phi(M)$ is the number of galaxies per unit mass interval, and M is related to $\rho(M)$ through $M = \rho(M)/\phi(M)$, we can rewrite the equation as

$$\dot{\rho}(M) = -\frac{ds(M)}{d \ln(M)}. \quad (26)$$

Integrated over the total stellar mass function, Equation 26 simply says that the rate of increase in the formed stellar mass density per unit time is equal to the SFRD.

Merging can also redistribute mass from low to high masses in the galactic mass function (e.g., Conselice07), but this is much harder to quantify. As we shall see below, Equation 26 provides a good description of the changes seen in the formed stellar mass function with mass and time without including substantial merging. Conselice07 reach a similar conclusion.

As a simple intuitive example of the meaning of Equation 26, we may consider the case where the specific star formation rate is constant (i.e., $s \propto \rho$). In this case the mass distribution function per unit logarithmic mass, as shown in Figure 39, simply moves to the right in the x-axis. Then the mass density in a given interval grows for high masses above the peak in the mass distribution function, where $d\rho/d \ln(M)$ is negative ($\dot{\rho}$ positive), and the mass density in a given interval drops at low masses, where $d\rho/d \ln(M)$ is positive ($\dot{\rho}$ negative).

In Figure 44 we show the formed stellar mass density growth rates produced by star formation (as calculated from Equation 26) for both the UV-based (*red squares*) and the $24 \mu\text{m} + [\text{O II}]$ -based (*blue diamonds*) methods. We can now compare these with the growth rates found earlier from the formed stellar mass functions (*purple lines*). The agreement between the shapes with both redshift and mass is amazingly good. However, there is a slight normalization difference, with the Equation 26 UV-based measurements being higher by about 0.1 dex in the $10^{10} - 10^{10.5} M_{\odot}$ interval and higher by about 0.2 dex in the $10^{10.5} - 10^{11} M_{\odot}$ and $10^{11} - 10^{11.5} M_{\odot}$ intervals. (The offset is -0.2 dex in the $10^{11.5} - 10^{12} M_{\odot}$ interval, but the uncertainties are large.) The offset is only slightly reduced

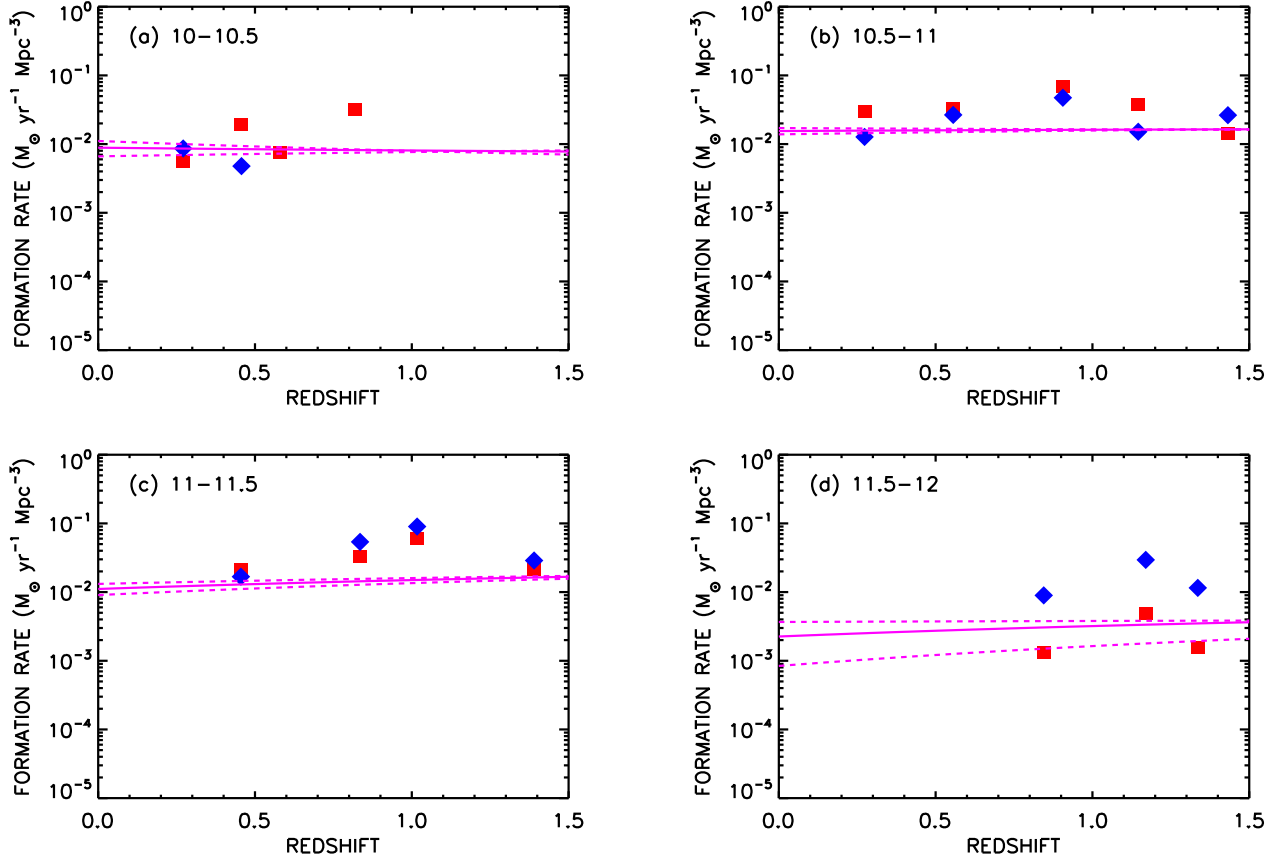


FIG. 44.— Mass formation rate densities from two different methods vs. redshift for the mass intervals (a) $10^{10} - 10^{10.5} M_{\odot}$, (b) $10^{10.5} - 10^{11} M_{\odot}$, (c) $10^{11} - 10^{11.5} M_{\odot}$, and (d) $10^{11.5} - 10^{12} M_{\odot}$. The red squares show the formed stellar mass density growth rates that the extinction corrected SFRDs calculated from the UV luminosity densities using our empirical calibrations would produce in each mass interval, as calculated from Eq. 26. The blue diamonds show the same but this time based on the SFRDs calculated from the $24 \mu\text{m}$ and extinction uncorrected [O II] fluxes. The purple solid lines show the formed stellar mass density growth rates as obtained from the derivative of the least-square polynomial fits to the stellar mass density history (Eqs. 19–22) after multiplying by a factor of 1.35 to convert the present stellar masses to formed stellar masses (see §1). The purple dashed lines show the range given by the 1σ errors on the fits. The black dotted lines show the 68% range in the specific star formation rates from Noeske et al. 2007.

if we exclude X-ray selected AGNs from the star formation calculation. Most previous analyses have also found the measurements based on star formation to be higher than the measurements based on the formed stellar mass functions (e.g., Fardal et al. 2007 and references therein). However, given the completely different wavelength ranges used (UV versus NIR), the uncertainties in the extinction corrections and in the stellar models, and the effects of cosmic variance, some discrepancy would inevitably be expected. In this sense, the agreement is remarkably good, even for the normalization.

The offset is unlikely to be due to relative uncertainties in the local mass function, which generally lie at the 20%–30% level (e.g., compare Cole01, Bell et al. 2003, and Eke et al. 2005 with each other). Cole01 lies at the high end of the mass density estimates, and reducing the local mass density would increase the discrepancy. The offset is also unlikely to be due to overestimation of the UV extinction corrections, since our $24\ \mu\text{m} + [\text{O II}]$ -based method for calculating the SFRDs is completely independent of the UV extinction corrections and shows extremely similar results to the UV-based method both in the direct SFRDs (Fig. 42) and in the formed stellar mass density growth rates computed from Equation 26 (Fig. 44).

However, the issue of the uncertainty in the population synthesis models and the recent treatments of TP-AGB stars, which we discussed in §4, is more complicated. If the BC03 masses which we are using are uniformly too high, then this would increase the discrepancy. However, if the local masses are close to the BC03 values and the high-redshift values are lower than the BC03 values, then we will increase the gradients in Equations 18–22, and this will reduce the discrepancy. We may estimate a maximum effect by assuming that the mass densities in the $z = 1.2 - 1.5$ interval are only 60% of the BC03 values (the maximum correction in Bruzual 2007). This only slightly increases the formed stellar mass density growth rates in the various mass intervals, generally by less than 0.1 dex. We can see the reason for this by inspecting Figure 40. Typically we are building a large fraction of the local mass density over $z = 0.05 - 1.5$ and changing the starting point mass density downward has a relatively limited effect on the required growth rate. Thus, it appears that the mass density growth rates cannot be raised enough to explain the discrepancy with the rates inferred from star formation.

A possible explanation for the offset is that the IMF is slightly different from the assumed Salpeter form. We can resolve the problem by changing the index of the IMF to -1.10 . This is well within the uncertainties in the slope of the high-end IMF (Kroupa 2001; Chabrier 2003) and close to the Baldry & Glazebrook (2003) value of -1.15 . However, in order to obtain our observed $\text{H}\alpha$ to UV ratio, we must turn this over at high masses. Using the -1.10 index to $10\ M_{\odot}$ and an index of -1.6 from $10\ M_{\odot}$ to $100\ M_{\odot}$ resolves both problems. Fardal et al. (2007) argued that this type of mid-mass-weighted IMF, which they describe as paunchy, can also help in providing a consistent description of the extragalactic background light.

11.5. Specific Star Formation Rates

We now consider the distribution of specific SFRs (SSFRs) in the individual galaxies. Although in computing

the instantaneous SSFRs we are simplifying the effects of the time history in the individual galaxies, it is still useful to have a quantitative description of the range of behaviors in the galaxies. We shall return to a study of the time history of the galaxies in §11.6.

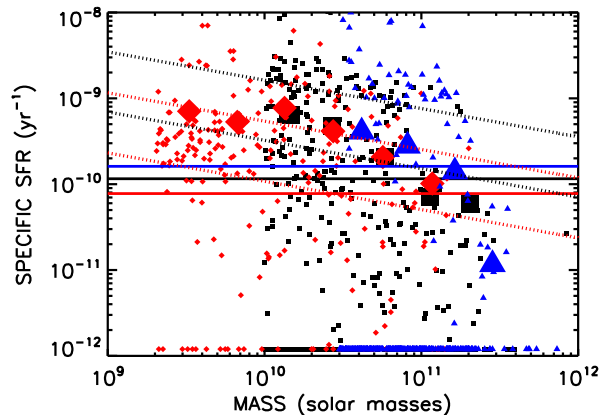


FIG. 45.— Specific star formation rates (SFR per unit mass in the galaxy) vs. mass in the redshift intervals $z = 0.05 - 0.475$ (red diamonds), $z = 0.475 - 0.9$ (black squares), and $z = 0.9 - 1.5$ (blue triangles). The high-redshift sample is only shown above the limiting $3 \times 10^{10}\ M_{\odot}$ to which it is complete. The large symbols show the mean values for each redshift interval. The solid lines show the inverse age of the universe at redshifts $z = 0.05$ (red), $z = 0.475$ (black), and $z = 0.9$ (blue). Only galaxies with an average SSFR above the inverse age of the universe at the redshift of the galaxy can undergo a significant change in mass. The red ($z = 0.2 - 0.7$) and black ($z = 0.85 - 1.1$) dotted lines show the “main sequence” range of Noeske et al. (2007). They claim that 68% of the galaxies should lie within this range based on their DEEP2 observations.

In Figure 45 we show the SSFRs versus galaxy mass in the redshift intervals $z = 0.05 - 0.475$ (red diamonds), $z = 0.475 - 0.9$ (black squares), and $z = 0.9 - 1.5$ (purple triangles). There is clearly a wide spread at all redshifts and masses. However, only galaxies with SSFRs larger than the inverse age of the universe at the redshift of the galaxy can change their mass significantly if those rates are maintained over the full time interval. We shall refer to such galaxies as strong star formers. Note that if the star formation is episodic, then the mass change in the galaxies will be smaller. Thus, the number of strong star formers represents an upper bound on the fraction of galaxies that may grow significantly at a given redshift. The mean SSFRs (large symbols) reproduce the results of §11.3. That is, they show that, on average, only galaxies with masses $\lesssim 10^{11}\ M_{\odot}$ grow significantly in any of the redshift intervals. Since the high-redshift blue triangles cross the growth line at slightly higher masses than the black squares and red diamonds of the lower redshift intervals, the typical mass at which growth is taking place is downsizing in the later redshift intervals. In the lowest redshift interval where we can measure the masses below $10^{10}\ M_{\odot}$, we see that the mean SSFRs finally flatten out (at a high level). There also appears to be a rough maximum to the SSFRs of about $3 \times 10^{-9}\ \text{yr}^{-1}$.

In Figure 46 we show the distribution functions of the SSFRs for the mass intervals (a) $10^{11} - 10^{11.5}\ M_{\odot}$, (b) $10^{10.5} - 10^{11}\ M_{\odot}$, and (c) $10^{10} - 10^{10.5}\ M_{\odot}$. In each panel the redshift intervals $z = 0.9 - 1.5$ (blue triangles), $z = 0.475 - 0.9$ (black squares), and $z = 0.05 - 0.475$ (red

diamonds) are shown. We see little evolution in the distribution functions over the observed redshift range, but they do have very different shapes in the different mass intervals.

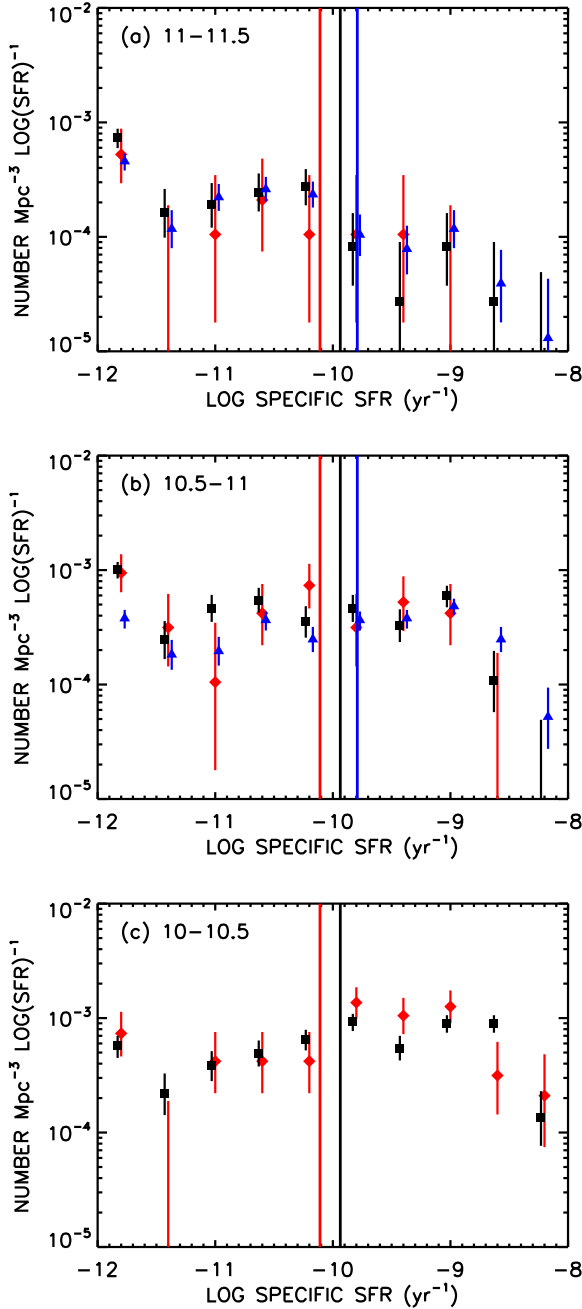


FIG. 46.— Distribution functions of the specific star formation rates for logarithmic mass intervals (a) $11 - 11.5 M_{\odot}$, (b) $10.5 - 11 M_{\odot}$, and (c) $10 - 10.5 M_{\odot}$. In each panel the red diamonds denote $z = 0.05 - 0.475$, the black squares $z = 0.475 - 0.9$, and the blue triangles $z = 0.9 - 1.5$. The error bars show the 68% confidence limits. The blue triangles and black squares have been slightly displaced in the x-axis (by plus and minus 0.03, respectively) to allow the error bars to be distinguished. The solid vertical lines show the log of the inverse age of the universe at redshifts $z = 0.05$ (red), $z = 0.475$ (black), and $z = 0.9$ (blue).

In the highest mass interval (Fig. 46a) most of the galaxies have very low SSFRs. There are only a small fraction of strong star formers at any redshift. Overall only about

10% of the galaxies can be growing significantly. In the two lower mass intervals (Figs. 46b,c) the number of sources with strong SSFRs increases. In fact, in the lowest mass interval (Fig. 46c) galaxies with SSFRs above the 10^{-10} yr^{-1} dominate the population. The percentages of strong star formers in all three mass intervals are given in Table 2. In the lowest mass range we give the values only in the two lower redshift intervals where the sample is complete.

We may conclude from this that what star formation is occurring in the galaxies in the $10^{11} - 10^{11.5} M_{\odot}$ interval is spread over many galaxies, and there are very few galaxies in this mass interval that are undergoing significant growth. The situation is less clear in the lower mass intervals. By the time we reach the $10^{10} - 10^{10.5} M_{\odot}$ interval, the distribution is roughly evenly split between galaxies undergoing strong star formation and galaxies with weak star formation (see Table 2). This could be a distinction between two populations: one with strong ongoing star formation and one with weak or little growth. Alternatively, it could be that there is a high frequency of bursting relative to steady star formation at these redshifts with all galaxies undergoing significant star formation on average. Regardless of this point, a substantial number of the low-mass galaxies have SSFRs that, if maintained over the time frame, would change their mass significantly.

We cannot easily compare our results with previous analyses of the evolution of the SSFRs over this redshift interval, such as Brinchmann & Ellis (2000) or Bauer et al. (2005), since they did not include extinction corrections, which make substantial increases in the SSFRs. However, we can compare our results with a recent analysis by Noeske et al. (2007), who used a portion of the DEEP2 sample with K -band and $24 \mu\text{m}$ observations to analyze the SSFRs. They used $24 \mu\text{m}$ plus emission line estimates of the SFRs. Noeske et al. (2007) claim that the SSFRs lie within a rather tightly defined range as a function of mass. The normalization of this range increases with redshift, with the SSFRs increasing by roughly a factor of three from $z = 0.3$ to $z = 1$. They argue that this implies a smooth evolution in the galaxy SFRs, a result which would be inconsistent with our subsequent analysis of the star formation histories in the more massive galaxies using Balmer lines and colors. We show their ranges in Fig. 45 with the dotted lines (red: $z = 0.2 - 0.7$; black: $z = 0.85 - 1.1$), where we have corrected their Kroupa masses to Salpeter. It is clear that the present results are inconsistent with the Noeske et al. (2007) analysis. While their upper bound corresponds roughly to the maximum values seen in the present SSFRs, we see a much larger scatter in the values for the high-mass galaxies above $10^{10} M_{\odot}$. Our data include many galaxies with low SSFRs. The result is not dependent on the method we used to calculate the SFRs. We find the same effect using the $24 \mu\text{m}$ plus emission line estimates of the SFRs. The result is also not a simple consequence of the optical magnitude selection used in DEEP2 ($R = 24.1$), since nearly all of the high-mass galaxies would be included by such a selection, as Noeske et al. (2007) discuss and we self-consistently find in the present data. The difference may lie in more subtle effects of the spectroscopic completeness versus color and optical magnitude or in the limited photometry of the DEEP2 sample.

We can also compare our results with the local analy-

sis of Brinchmann et al. (2004), and, in particular, with their Figure 24. (Their masses are based on the Kroupa IMF and must be increased by a factor of 1.54 to match ours.) Brinchmann et al. (2004) only included star forming galaxies in their analysis, so their distribution is truncated at low SSFRs and the means are slightly higher. Nevertheless, the overall shape and normalization, including the roughly constant SSFRs at low mass, the decline in the SSFRs above $10^{10} M_{\odot}$, the upper bound on the SSFRs, and the change in the distribution of SSFRs at high mass are all in extremely good agreement with the present results.

11.6. Galaxy Colors, Equivalent Widths, and the 4000 Å Break

Rest-frame galaxy colors and features in the spectra, such as the equivalent widths of the emission lines and the strengths of the 4000 Å break, provide a measure of the SSFRs convolved with the recent time history of the star formation. Since the colors and the various spectral features are sensitive to different stellar mass ranges, they can provide information on the time history of the star formation and how smooth or episodic it is. (See, e.g., the Kauffmann et al. 2003a analysis of the SDSS sample using the 4000 Å break and the H δ line.) Thus, the combination of photometric and spectroscopic information in the present sample provides a powerful tool to investigate the nature of the star formation.

Locally the SDSS results have shown that the galaxy colors are bimodal and divide into a red sequence of galaxies that are not currently undergoing star formation and a blue cloud of galaxies with active star formation (e.g., Strateva et al. 2001; Baldry et al. 2004). The red sequence dominates above $3 \times 10^{10} M_{\odot}$ (Kauffmann et al. 2003b), and the blue cloud dominates below. This color bimodality is also seen in higher redshift, optically-selected samples (e.g., Bell et al. 2004; Weiner et al. 2005; Giallonga et al. 2005; Willmer et al. 2006). However, these analyses did not correct for internal extinction, which, as we shall show below, is important. Moreover, the bimodality appears to be at least partially a consequence of the optical selection and is not so strong in our mass-selected samples at the higher redshifts.

In Figure 47 we show the rest-frame UV–blue (AB3400–AB4500) colors uncorrected for extinction for our full NIR sample versus redshift. (Note that if we change to the Vega-based magnitudes used by Willmer et al. 2006 in their DEEP2 analysis, then we find a nearly identical range of colors as they.) We see almost no evolution in the color distribution over the $z = 0.05$ –1.5 redshift range. The precise split between the blue cloud and the red sequence depends on the mass or luminosity, but we have shown the rough split with the red dashed line. This is based on the average value of the relation given by van Dokkum et al. (2000) in the appropriate luminosity range. It is not easy to see evidence for strong bimodality in this figure. Rather, we see a uniform spread of colors stretching from the blue cloud to the red sequence. Nearly all of the galaxies in the intermediate color range (sometimes referred to as the green valley) are 24 μ m sources (green triangles).

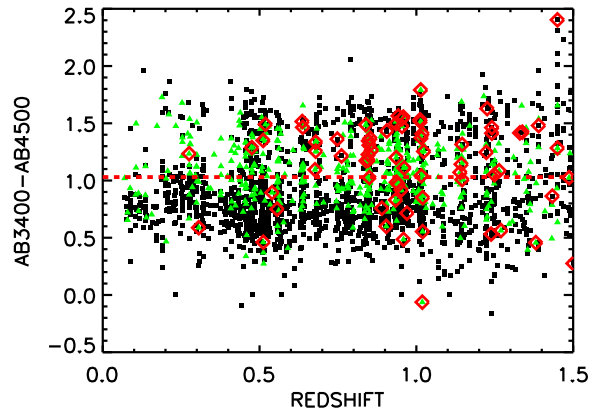


FIG. 47.— Rest-frame 3400–4500 Å color vs. redshift for our NIR sample. Green triangles denote 24 μ m sources, and black squares denote sources which are not detected at 24 μ m. Sources with X-ray luminosities implying the presence of an AGN are enclosed in red diamonds. The red dashed horizontal line shows the approximate separation between the blue cloud and the red sequence based on the average value of the relation given by van Dokkum et al. (2000) in the appropriate luminosity range.

The spread in colors may be more clearly seen in histogram form. In Figure 48a we show the colors prior to applying any extinction corrections. We see that the 24 μ m sources lie in the green valley (green dashed line). While there is a hint of bimodality in the total sample (black solid line), it is quite weak with sources present at all colors. In Figure 48b we show the colors after correcting for extinction. Now the bulk of the 24 μ m sources lie in the blue cloud, and there is a more clearly bimodal distribution in the total sample. Even with the extinction correction there are still many sources (both 24 μ m and non-24 μ m) in the intermediate color region, but it is clear that applying extinction corrections is critical when analyzing the galaxy colors. Many of the sources seen in the green valley and the red sequence prior to correcting for extinction are, in fact, dusty sources with intrinsically blue colors. Quantitatively, 801 out of 2254 sources (35%) are in the red sequence (defining this as AB3400–AB4500 > 1.03) prior to the extinction correction, but nearly half of these are dusty blue galaxies. After applying the extinction correction, the number in the red sequence gets reduced to 466 out of 2254 sources, or roughly 20%.

The extinction corrections have a mass dependence since higher mass galaxies, with their larger column densities of gas and dust, reprocess more of their UV light. (The very highest mass galaxies will generally have lower extinctions because they are gas deficient.) The extinction corrections may also have a redshift dependence due to the evolution in the metallicity and gas content of the galaxies. Thus, any analyses of the color versus mass or color versus luminosity relations that do not apply extinction corrections will be biased.

In Figure 49 we show the dereddened colors versus galaxy mass for the redshift intervals (a) $z = 0.9$ –1.5, (b) $z = 0.475$ –0.9, and (c) $z = 0.05$ –0.475. The red sequence is clearly seen in all of the intervals. Rather than attempt to measure the slope of the color-mass relation from the present data, we have assumed the locally determined slope of 0.08 mag per dex in mass determined by

van der Wel et al. (2007). We then normalized this slope to match the red sequence galaxies in the $z = 0.9 - 1.5$ redshift interval with masses above $3 \times 10^{10} M_{\odot}$ to obtain the red sequence relation with mass, M ,

$$AB3400 - AB4500 = 1.26 + 0.08(\log M - 9). \quad (27)$$

We show this relation with the solid black line in Figure 49. In contrast to previous results from optically-selected and extinction uncorrected data (e.g., Bell et al. 2004; van der Wel et al. 2007), we see no change in the position of the red sequence with redshift. This suggests that the effect they observed was primarily a consequence of reddening. The intrinsic colors of the reddest galaxies are not changing over this redshift interval.

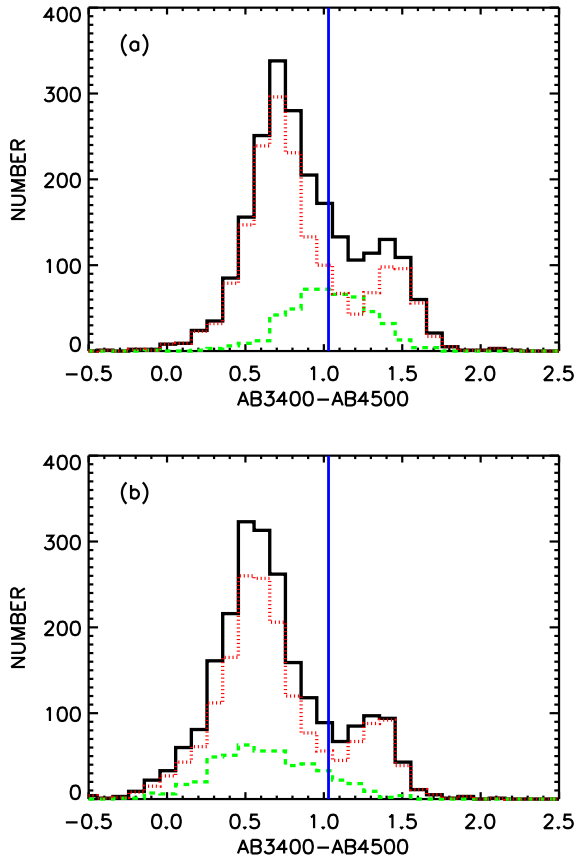


FIG. 48.— Distribution of rest-frame 3400 – 4500 Å color for our NIR sample (a) before and (b) after correcting for internal extinction. The black histogram shows the distribution of the total sample. The green dashed (red dotted) line shows the distribution of 24 μm (non-24 μm) sources. The blue vertical line shows the approximate separation between the blue cloud and the red sequence based on the average value of the relation given by van Dokkum et al. (2000) in the appropriate luminosity range.

While it is clear from Figure 48 that there is no precise split between the red sequence and the blue cloud, we may approximately separate them with a cut lying about 0.25 mag below the track of the red sequence,

$$AB3400 - AB4500 = 1.01 + 0.08(\log M - 9). \quad (28)$$

This allows for the spread in colors in the red sequence itself. We show this relation in Figure 49 with the solid blue line. The high-mass, blue cloud galaxies are nearly

all 24 μm sources (*green triangles*). Moreover, most of the 24 μm sources lie in the blue cloud, though at the highest masses we also see some 24 μm sources that move into the red sequence region.

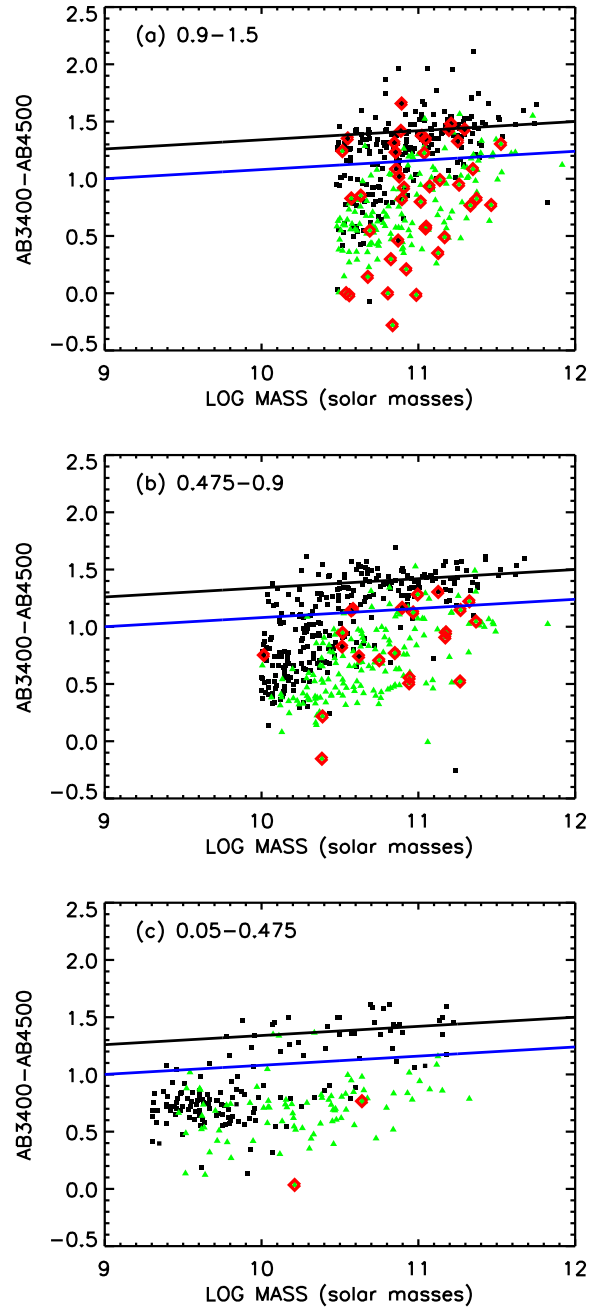


FIG. 49.— Rest-frame 3400 – 4500 Å color corrected for extinction vs. logarithmic mass for our NIR sample in the redshift intervals (a) $z = 0.9 - 1.5$, (b) $z = 0.475 - 0.9$, and (c) $z = 0.05 - 0.475$. The colors are only shown above the mass at which the sample in the given redshift interval is complete. Green triangles denote 24 μm sources, and black squares denote sources which are not detected at 24 μm . Sources with X-ray luminosities implying the presence of an AGN are enclosed in red diamonds. The solid black line shows the red sequence (with locally determined slope 0.08 mag per dex in mass) normalized to match the $z = 0.9 - 1.5$ interval. The blue line shows this relation offset by 0.25 mag, which we adopt as the split between the red sequence and the blue cloud.

Although we can see that the red sources dominate at

the high masses and that nearly all low-mass galaxies below $10^{10} M_{\odot}$ are blue cloud galaxies, there does not appear to be a clear transition mass in any of the redshift intervals. Rather, the fraction of galaxies with high SSFRs drops as we move to higher masses in all the redshift intervals. We also note that the split between the blue cloud and the red sequence becomes more pronounced at low redshifts, while at higher redshifts there are a considerable number of intermediate color sources.

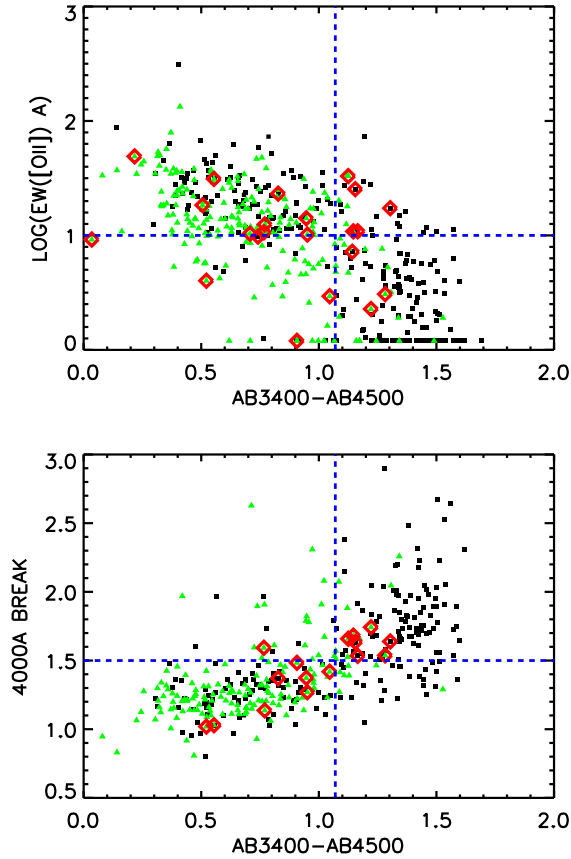


FIG. 50.— (a) $EW([OII])$ and (b) the 4000 \AA break vs. the extinction corrected rest-frame $AB3400-AB4500$ color for the mid- z sample ($z = 0.05 - 0.9$) with masses greater than $10^{10} M_{\odot}$. The black squares (green triangles) show sources without (with) $24 \mu\text{m}$ detections. Sources containing AGNs based on their X-ray luminosities are enclosed in large red diamonds. The blue dashed lines show the rough division between the blue cloud and the red sequence. A color selection of $AB3400-AB4500 > 1.07$, which would separate the red sequence from the blue cloud at $10^{11} M_{\odot}$, roughly corresponds to an $EW([OII]) < 10 \text{ \AA}$ or a 4000 \AA break strength greater than 1.5.

We may also use the $EW([OII])$ or the 4000 \AA break to separate the galaxies. The $EW([OII])$ is independent of the extinction correction, and the 4000 \AA break is nearly independent so these provide an invaluable check of our analysis of the colors. In particular this removes any dependence on our BC03 fitting. In Figure 50 we show (a) the $EW([OII])$ and (b) the 4000 \AA break versus the extinction corrected rest-frame $AB3400-AB4500$ color. While there is not a perfect one-to-one relation, a color selection of $AB3400-AB4500 > 1.07$ (blue dashed vertical line), which would separate the red sequence from the blue cloud at $10^{11} M_{\odot}$, roughly corresponds to an

$EW([OII]) < 10 \text{ \AA}$ (blue dashed horizontal line in a) or a 4000 \AA break strength greater than 1.5 (blue dashed horizontal line in b). Thus, these cuts may also be used to separate red sequence galaxies from blue cloud galaxies.

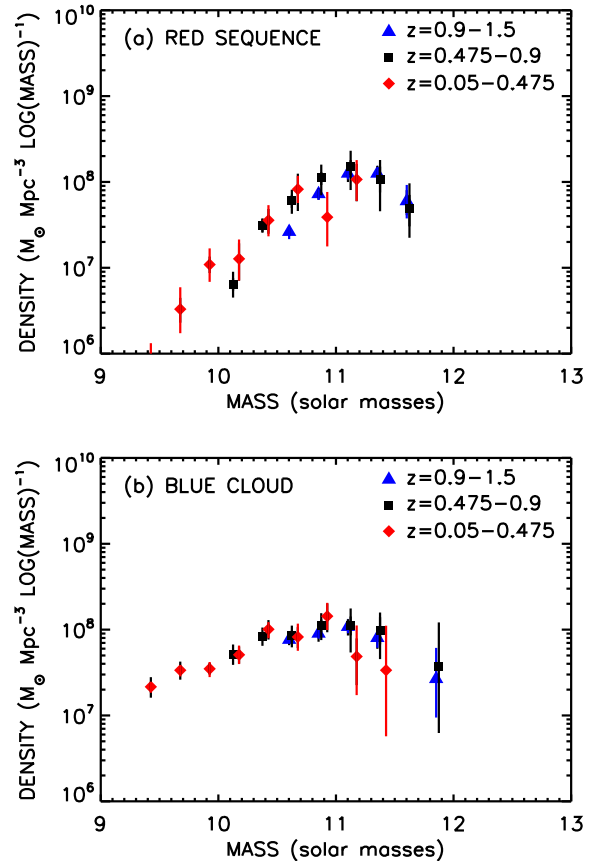


FIG. 51.— Mass density per unit log mass functions for (a) the red sequence galaxies and (b) the blue cloud galaxies in the redshift intervals $z = 0.9 - 1.5$ (blue triangles), $z = 0.475 - 0.9$ (black squares), and $z = 0.05 - 0.475$ (red diamonds).

In Figure 51 we show the mass density per unit log mass distribution functions separated by color using our dividing line between the blue cloud and the red sequence given in Equation 28. There are almost equal amounts of mass in the two color-selected samples, though the red sequence is highly peaked at $10^{11} M_{\odot}$ while the blue sequence has a substantial contribution from lower mass galaxies. In the $z = 0.475 - 0.9$ redshift interval the red sequence contains $1.29 \times 10^8 M_{\odot} \text{ Mpc}^{-3}$ and the blue cloud $1.45 \times 10^8 M_{\odot} \text{ Mpc}^{-3}$ to the $10^{10} M_{\odot}$ completeness limit at this redshift. Figure 51a shows that growth in the mass density is occurring in red galaxies with masses in the interval $10^{10.5} - 10^{11} M_{\odot}$. However, it must be noted that this result is only based on the difference between the $z = 0.475 - 0.9$ and $z = 0.9 - 1.5$ redshift intervals in the one mass bin and therefore the conclusion is rather weak. In contrast, Figure 51b shows little apparent change in the mass distribution of the blue cloud with redshift. Bell et al. (2004), who first noted this effect, argued that since the star formation, and hence the mass build-up, is primarily occurring in the blue galaxies, the blue galaxies must be shifting to the red sequence at all times in order to leave the blue mass function invariant. However, Bundy et al.

(2006) and Borch et al. (2006) both show evidence for a decline in the massive blue galaxies with cosmic time.

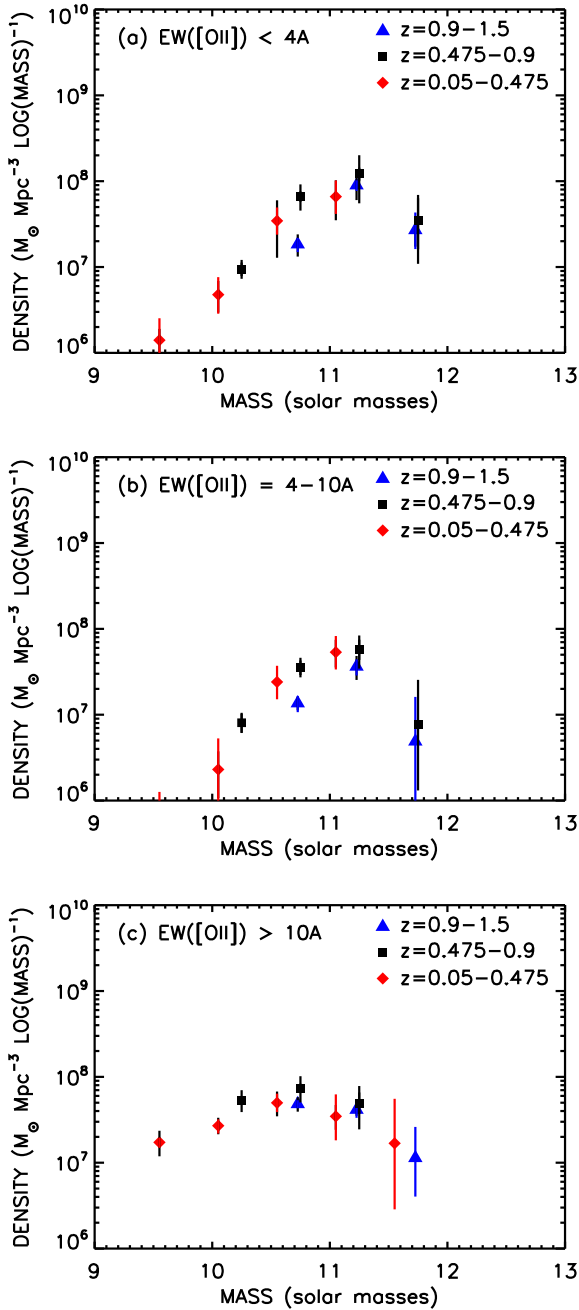


FIG. 52.— Mass density per unit log mass functions for rest-frame (a) $\text{EW}([\text{O II}]) < 4 \text{ \AA}$, (b) $4 \text{ \AA} < \text{EW}([\text{O II}]) < 10 \text{ \AA}$, and (c) $\text{EW}([\text{O II}]) > 10 \text{ \AA}$ in the redshift intervals $z = 0.9 - 1.5$ (blue triangles), $z = 0.457 - 0.9$ (black squares), and $z = 0.05 - 0.475$ (red diamonds).

We can make a finer division using the $\text{EW}([\text{O II}])$. In Figure 52 we show the mass function split into three classes according to the strength of the $[\text{O II}]$ line. In (c) we show sources with rest-frame $\text{EW}([\text{O II}]) > 10 \text{ \AA}$, which, as we have discussed above, roughly corresponds to the blue cloud color selection. As for Figure 51b, we see few signs of evolution. (Note that cosmic variance may be causing us some problems with the lowest redshift sources.) We then split the remaining galaxies into (b) weak emitters with

$4 \text{ \AA} < \text{EW}([\text{O II}]) < 10 \text{ \AA}$ and (a) passive sources with $\text{EW}([\text{O II}]) < 4 \text{ \AA}$. With this division we can see growth occurring in both the passive sources and in the sources with weak star formation signatures, suggesting that the red sequence contains both a truly passive population with no signs of recent star formation and a population which has more recently evolved off the blue cloud and still contains signatures of recent star formation.

We may consider this further by plotting the rest-frame AB3400–AB8140 color versus the rest-frame $\text{EW}(\text{H}\beta)$ to investigate the star formation history. Both are measures of the SSFRs in the galaxies and are therefore correlated with one another, but the $\text{EW}(\text{H}\beta)$ is produced by higher mass stars and thus fades more rapidly than the AB3400–AB8140 color, providing a well-known age signature. In Figure 53 we plot the extinction corrected rest-frame AB3400–AB8140 color versus the rest-frame $\text{EW}(\text{H}\beta)$ for the $z = 0.05 - 0.9$ sample with masses (a) $10^{11} - 10^{12} M_{\odot}$, (b) $10^{10.5} - 10^{11} M_{\odot}$, and (c) $10^{10} - 10^{10.5} M_{\odot}$. All but one of the galaxies in the highest mass interval (Figure 53a) have little $\text{H}\beta$ emission. Most of the sources are very red, but there is a tail which extends to bluer colors. The $24 \mu\text{m}$ detected galaxies (*blue triangles*) are preferentially bluer than the non- $24 \mu\text{m}$ galaxies (*black squares*). We compare the observations with some simple evolutionary tracks from the BC03 models for galaxies with exponentially declining SFRs of 10^8 yrs (*black solid*) (essentially a burst model), 5×10^8 yrs (*red dashed*), and 5×10^9 yrs (*green dotted*). The positions of the galaxies in Figure 53a are not consistent with the green dotted line, where the smoothly declining star formation history would continue to produce $\text{H}\beta$ emission at intermediate AB3400–AB8140 colors. Rather, we appear to be seeing episodic bursts of star formation that have moved the galaxy off the red sequence, but where the massive stars powering the $\text{H}\beta$ emission have already burned away. Considering the burst model shown by the black line in Figure 53a, about a quarter of the galaxies have colors which would require a burst to have occurred in the last $3 \times 10^8 - 10^9$ yrs (*thin portion*). It is these galaxies, which still have substantial UV flux, that are inferred to have high SSFRs in Figure 46, while the more evolved galaxies lie in the low SSFR portion of this diagram. (This emphasizes again that the SSFRs in Figure 46 are not necessarily measures of the instantaneous star formation in the galaxy but are a time convolution of the SFR history.) In order to have this fraction of galaxies in the portion of the evolutionary track we would require bursts to occur in all galaxies about every 4×10^9 yrs. If some galaxies are totally passive and do not participate in this cycling between the red sequence and the blue cloud then the remaining galaxies must have more frequent bursts.

Differential extinction, where the very massive stars producing the $\text{H}\beta$ line are more extinguished than the stars producing the UV continuum, could increase the $\text{EW}(\text{H}\beta)$ strength. However, this effect would have to be very large to move the blue sources with very weak $\text{H}\beta$ to the smooth star formation curves, and, as we have discussed in §6, we see no signs of this effect in our comparison of the Balmer line ratios and the SED derived extinctions. Errors in the UV extinction corrections may also introduce scatter in the y-axis and place some sources at bluer locations than

they should have, but, again, this effect cannot be large enough to move the sources onto the smooth star formation curves. Finally, truncation of the SFRs in the smooth models can move the tracks laterally over onto the burst model on short timescales, but it would not account for the bluest sources in the figure, which can only be reproduced with short bursts.

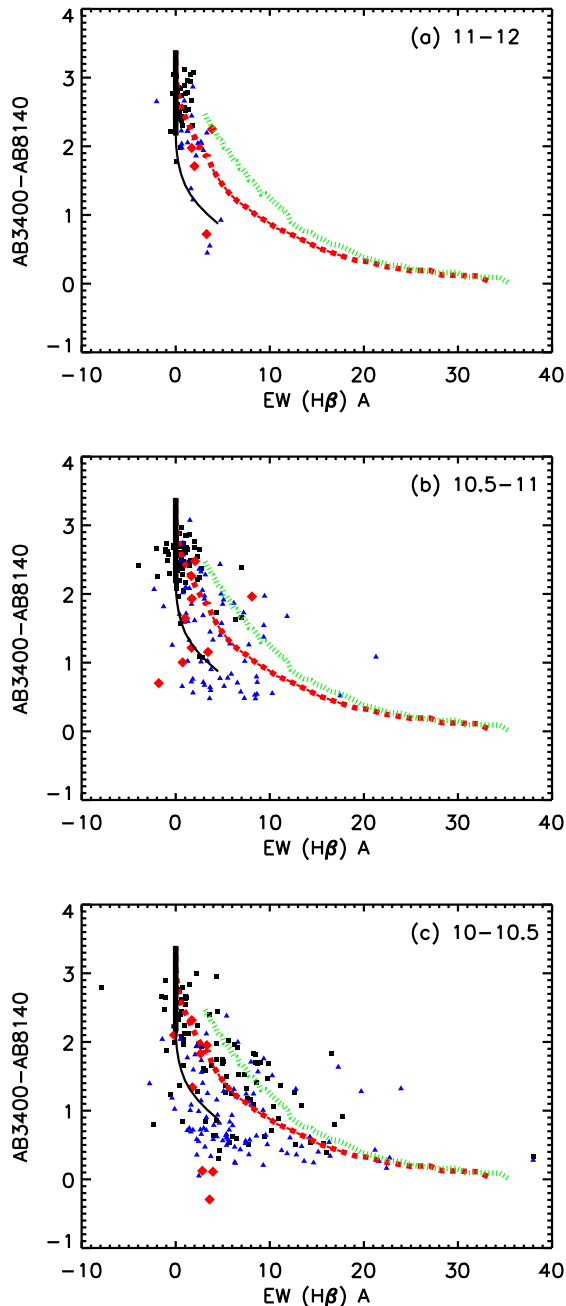


FIG. 53.— Extinction corrected rest-frame AB3400-AB8140 vs. rest-frame EW(H β) for the $z = 0.05 - 0.9$ sample in the logarithmic mass intervals (a) $11 - 12 M_{\odot}$, (b) $10.5 - 11 M_{\odot}$, and (c) $10 - 10.5 M_{\odot}$. The black squares (blue triangles) show sources without (with) $24 \mu\text{m}$ detections. Sources containing AGNs based on their X-ray luminosities are denoted by large red diamonds. The curves show the tracks expected from the BC03 models for galaxies with exponentially declining star formation rates of 10^8 yrs (black solid), 5×10^8 yrs (red dashed), and 5×10^9 yrs (green dotted). The black curve is divided into ages of $3 \times 10^8 - 10^9$ yrs (thin portion) and greater than 10^9 yrs (thick portion).

The intermediate mass galaxies in Figure 53b have a larger fraction of galaxies with blue AB3400-AB4500 colors, suggesting that the burst frequency is higher in these galaxies. For the lowest mass galaxies shown in Figure 53c there appears to be a distinction between the $24 \mu\text{m}$ sources (blue triangles), which still preferentially lie along the burst track, and the non- $24 \mu\text{m}$ sources (black squares), which are more consistent with smooth ongoing star formation. This suggests that it is the burst process which results in the dusty galaxies producing the $24 \mu\text{m}$ emission. In the higher mass galaxies bursting is the dominant process and all the galaxies with high SFRs are $24 \mu\text{m}$ sources.

11.7. Galaxy Morphologies

Galaxy morphologies, while closely related to the colors and spectral properties of the galaxies, provide an alternative view of the evolution. In particular, we would like to see in which types of galaxies the star formation and mass evolution is occurring and use this information to clarify the relationship between star formation and stellar growth in the mass density.

The Ellis morphological classifications that we are using (see §2.3) are based on the *HST* F850LP images. Therefore, in order to avoid biasing in type by observing the galaxies in the rest-frame UV rather than in the rest-frame optical, we will restrict the NIR sample to only galaxies at $z < 1.2$ for this section. This ensures that the F850LP band corresponds to rest-frame wavelengths above 4000 \AA .

We first compare the morphological typings with the spectral characteristics of the galaxies. In Figure 54 we show the distribution of the galaxy types in both rest-frame EW(H β) and 4000 \AA break strength. The black symbols show the E/S0 galaxies (classes 0-2), the green symbols show the Sab and S galaxies (classes 3-4), and the small red symbols show the Scd and Irr galaxies (classes 5-6). The large red squares show the galaxies classified as Mergers (class 8). Both the spectral and the morphological typings place nearly all of the massive galaxies ($10^{11} - 10^{12} M_{\odot}$; Figure 54a) into the E/S0 or Sab-S categories, while the lower mass galaxies ($10^{10} - 10^{11} M_{\odot}$; Figure 54b) show a much wider distribution, including many Irr. Figure 54 may be compared with Figure 4 of Barbaro & Poggianti (1997) for a local sample. The positions of the morphological types in the 4000 \AA break-EW(H β) plane match closely the positions of the local values. There is no change in this distribution over the redshift range $z = 0.05 - 0.9$.

In Figure 55 we quantitatively show the distribution of the EW(H β) by morphological type for the mass intervals (a) $10^{11} - 10^{12} M_{\odot}$, (b) $10^{10.5} - 10^{11} M_{\odot}$, and (c) $10^{10} - 10^{10.5} M_{\odot}$. We divide the galaxies into the broader classes of E/S0s (classes 0-2) (solid black line), Spirals (classes 3-5) (dashed red line), and Peculiars (classes 6 and 8) (dotted cyan line). The distribution of equivalent widths is very similar for the Spirals and the Peculiars, but it is a strong function of mass. Most of the massive Spirals are only weak star formers, while the lower mass Spirals have a much wider distribution of equivalent widths, and the mean equivalent width is much larger.

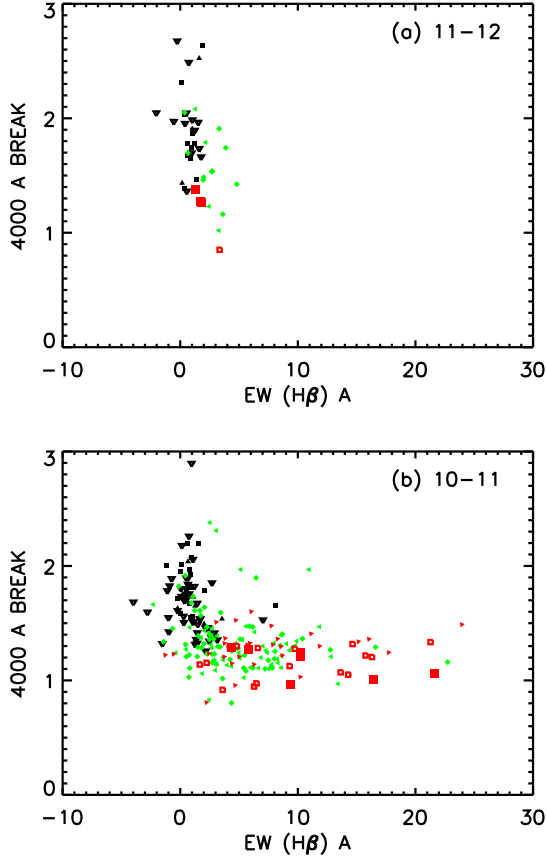


FIG. 54.— Distribution of morphological types in both 4000 Å break strength and rest-frame $EW(H\beta)$ in the mid- z sample ($z = 0.05 - 0.9$) for the logarithmic mass intervals (a) $11 - 12 M_{\odot}$ and (b) $10 - 11 M_{\odot}$. The black symbols show the E/S0 galaxies (solid squares = class 0, solid triangles = class 1, and open downward-pointing triangles = class 2); the green symbols show the Sab and S galaxies (diamonds = class 3, leftward-pointing triangles = class 4); the small red symbols show the Scd and Irr galaxies (open squares = class 5, rightward-pointing triangles = class 6); and the large red squares show the Mergers (class 8).

In Figure 56 we show galaxy morphological type versus mass for the redshift intervals $z = 0.05 - 0.475$ (*red diamonds*), $z = 0.475 - 0.9$ (*black squares*), and $z = 0.9 - 1.2$ (*blue triangles*). For each redshift range we only show galaxies above our mass completeness level of $2 \times 10^9 M_{\odot}$, $10^{10} M_{\odot}$ and $2 \times 10^{10} M_{\odot}$ respectively. Confirming a well-known result, we see a strong correlation between the galaxy morphology and the galaxy mass, with many of the most massive galaxies being E/S0s (classes 0 – 2). The large symbols show the median morphological types by mass and by redshift. A strong evolution with redshift in the mass-morphology relation is also evident. As an example, the typical $10^{11} M_{\odot}$ galaxy has moved from being an Sb-like (class 4) galaxy in the $z = 0.9 - 1.2$ redshift interval (*blue*) to being an S0 (class 2) galaxy in the $z = 0.05 - 0.475$ redshift interval (*red*), but this kind of morphological type evolution is present across the entire mass range.

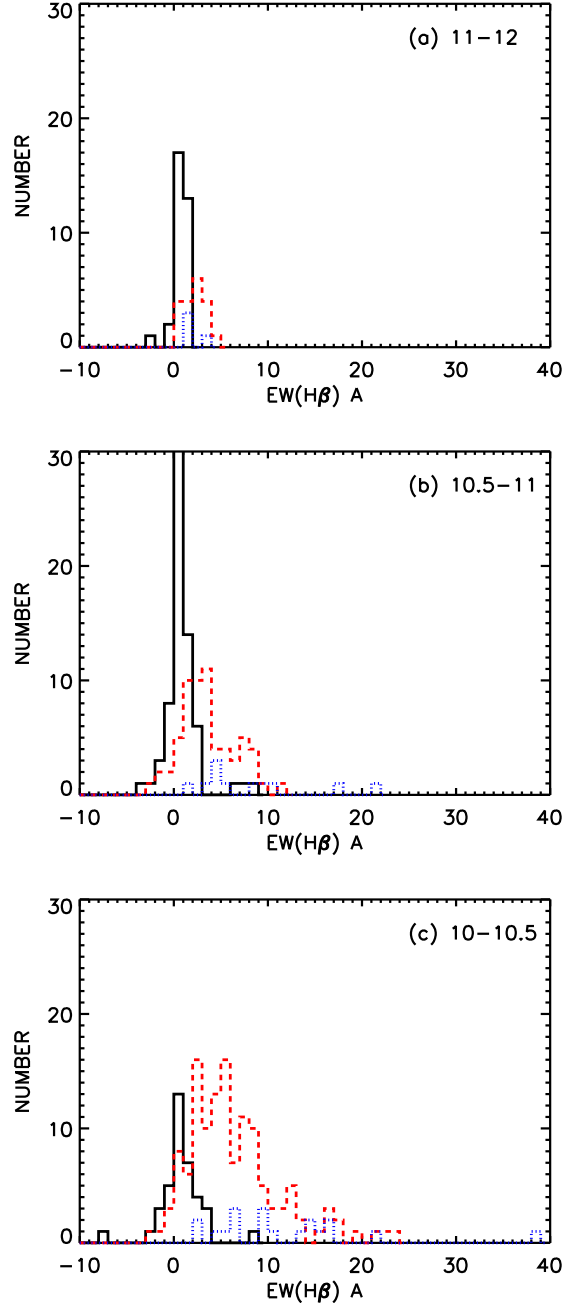


FIG. 55.— Distribution of rest-frame $EW(H\beta)$ for galaxies in the redshift interval $z = 0.05 - 0.9$ and in the logarithmic mass intervals (a) $11 - 12 M_{\odot}$, (b) $10.5 - 11 M_{\odot}$, and (c) $10 - 10.5 M_{\odot}$. In each panel the solid black line shows the E/S0 galaxies (classes 0 – 2), the red dashed line shows the Spirals (classes 3 – 5), and the dotted blue line shows the Peculiars (classes 6 and 8).

We may now examine the morphological type distribution in which the stellar growth in the mass density is occurring. As we showed in §11.6 (Fig. 52), the mass build-up in the redshift range $z = 0.05 - 0.9$ is primarily in the passive ($EW([O II]) < 4 \text{ \AA}$) and weakly active galaxies ($4 \text{ \AA} < EW([O II]) < 12 \text{ \AA}$) in the $10^{10.5} - 10^{11} M_{\odot}$ interval. In Figure 57 we show the distribution of morphological types in this redshift and mass interval split into passive galaxies (*black solid line*), weakly active galaxies (*red dashed line*), and strong emission line galaxies (*blue*

dotted line). It can be seen that the weakly active galaxies primarily lie in the spiral and S0 classes, though they are more strongly weighted to S0s than are the strong emitters, while the passive galaxies predominantly lie in the E/S0 classes. (We note in passing that we have visually checked the emission line galaxies that are morphologically classified as E, and these classifications are generally robust.)

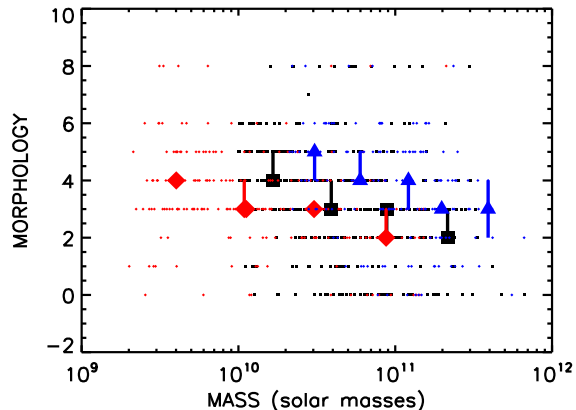


FIG. 56.— Galaxy morphological types (classes 0–8) vs. mass for the redshift intervals $z = 0.05–0.475$ (red diamonds), $z = 0.475–0.9$ (black squares), and $z = 0.9–1.2$ (blue triangles). For each redshift range we only show galaxies above our mass completeness level of $2 \times 10^9 M_{\odot}$, $10^{10} M_{\odot}$ and $2 \times 10^{10} M_{\odot}$ respectively. In each redshift interval the large symbols show the median values for that mass interval with 68% confidence limits. The error bars are generally one morphological class or less which can result in an asymmetrical appearance.

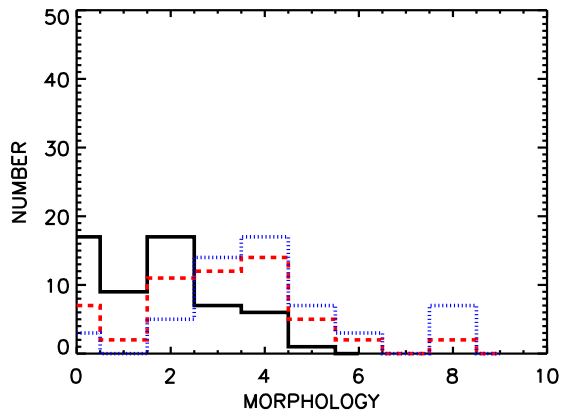


FIG. 57.— Distribution of morphological types for galaxies in the $z = 0.05–0.9$ redshift range with logarithmic masses $10.5–11 M_{\odot}$. The black solid line shows passive galaxies with $\text{EW}([\text{O II}]) < 4 \text{ \AA}$, the red dashed line shows weakly active galaxies with $4 \text{ \AA} < \text{EW}([\text{O II}]) < 12 \text{ \AA}$, and the blue dotted line shows strong emission line galaxies with $\text{EW}([\text{O II}]) > 12 \text{ \AA}$.

In Figure 58 we show the build-up of the mass density per unit logarithmic mass as a function of redshift and galaxy type. We have separated the E/S0 class into E (class 0) and S0 (classes 1–2) classes, though if we instead separate it into E (class 0–1) and S0 (class 2) classes, it does not change our conclusions. Here it can be seen that both the E (Fig. 58a) and S0 (Fig. 58b) classes are building up strongly in the $10^{10.5}–10^{11} M_{\odot}$ interval,

while the Spirals (Fig. 58c) and Peculiars (Fig. 58d) are not changing significantly. When we further separate the E/S0 galaxies by the $\text{EW}([\text{O II}])$, we find that all of the growth is in the passive or weakly active galaxies.

Thus, it appears that the mass build-up is primarily moving into elliptical and S0 galaxies. In other words, mass formation occurs in the spiral galaxies, and the spiral galaxies gradually move into the E/S0 class with decreasing redshift as the overall star formation dies away. This results in the mass function of the strong emitters and spiral galaxies being relatively invariant and the mass build-up being primarily seen in the passive and weakly active E/S0 galaxies.

11.8. Galaxy Environments

As described in §2.4, we use the projected nearest neighbor density, Σ_3 , to characterize the galaxy environment. In order to provide a uniform sample with a sufficiently high density to minimize edge effects, we use the galaxy sample with masses greater than $2 \times 10^{10} M_{\odot}$ to compute Σ_3 . This restricts our analysis to the redshift range $z = 0.3–1.2$. The lower redshift bound is set by the size of the field and our edge restriction (objects must be more than 1 Mpc from the field edge), and the upper redshift bound is set by the mass limit of the sample. The average density is $\Sigma_3 = 0.96 \text{ Mpc}^{-2}$, and very few objects have densities less than 0.3 Mpc^{-2} , where edge effects begin to enter. (A $4 \times 10^{10} M_{\odot}$ sample gives an average $\Sigma_3 = 0.31 \text{ Mpc}^{-2}$, where this issue would be more significant.)

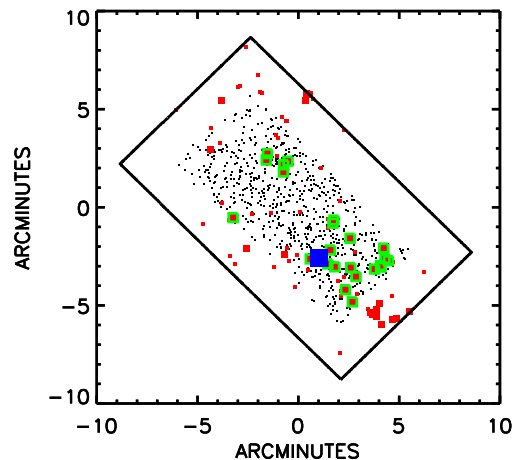


FIG. 59.— Galaxies in the $z = 1.0156$ sheet in the GOODS-N region are shown by the red squares (large symbols correspond to galaxies with masses above $2 \times 10^{11} M_{\odot}$; small symbols to lower mass galaxies). The full region of the field is shown by the black rectangle. The galaxies with measured Σ_3 are shown with small black squares. This region is smaller than the full field because of the edge constraint. Galaxies in the velocity slice with $\Sigma_3 > 3 \text{ Mpc}^{-2}$ are shown enclosed in green squares. The large blue symbol shows the position of the diffuse X-ray emission from Bauer et al. (2002).

Nearly all of the sources with $\Sigma_3 > 5 \text{ Mpc}^{-2}$ lie in just four velocity sheets at $z = 0.4851, 0.8472, 0.9367,$ and 1.0156 . The strongest of these is the well-known structure at $z = 1.0156$, which we illustrate in Figure 59 (*red squares*). This feature is dominated by a fairly substantial cluster lying at the southern end of the GOODS-N region, together with a smaller concentrated group to the north. We have identified 29 galaxies in the southern cluster with masses above $2 \times 10^{10} M_{\odot}$. The total stellar mass of these

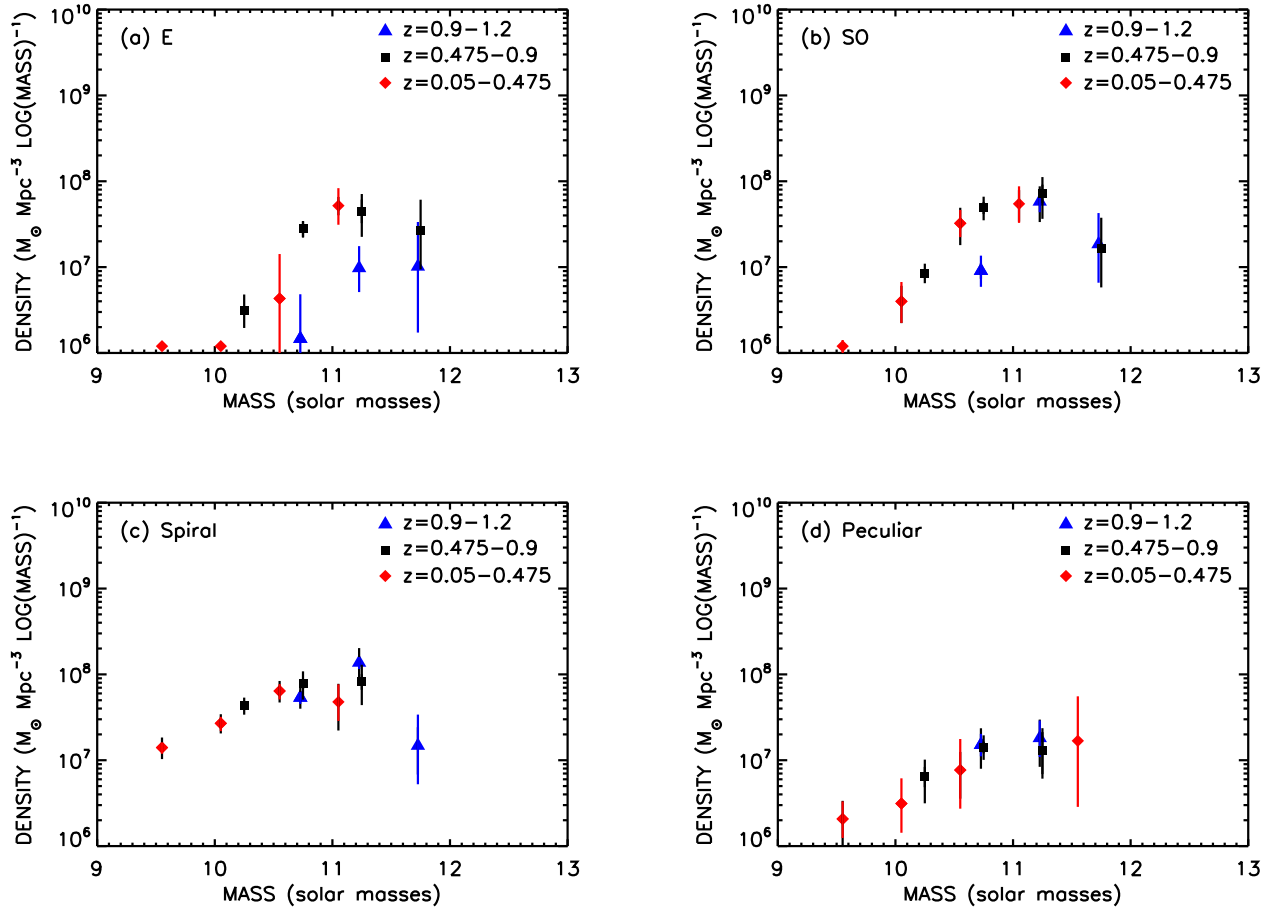


FIG. 58.— Build-up of the mass density per unit logarithmic mass for the redshift intervals $z = 0.9 - 1.2$ (*blue triangles*), $z = 0.475 - 0.9$ (*black squares*), and $z = 0.05 - 0.475$ (*red diamonds*) and for the morphological classes (a) E (class 0), (b) S0 (classes 1 – 2), (c) Spirals (classes 3 – 5), and (d) Peculiars (classes 6 and 8).

29 galaxies alone is $4 \times 10^{12} M_{\odot}$. The velocity dispersion is 470 km s^{-1} . There is associated diffuse X-ray emission centered on one part of the cluster (Bauer et al. 2002) (*blue square*). Within the region where the density parameter can be measured, nearly all of the galaxies at $z = 1.0156$ lie in substantially overdense regions with $\Sigma_3 > 3 \text{ Mpc}^{-2}$ (*green squares*). The other sheets are weaker and, in some cases (e.g., the $z = 0.8472$ structure), more diffuse.

Because the redshift intervals have different mass limits, it is most natural to plot the density parameter versus mass. In Figure 60 we show this relation for the redshift intervals $z = 0.9 - 1.2$ (*blue triangles*), $z = 0.475 - 0.9$ (*black squares*), and $z = 0.3 - 0.475$ (*red diamonds*). The mass-density relation is clearly seen in the median values (*large symbols*). At lower masses (below $10^{11} M_{\odot}$) the dependence on the environment is very weak. However, nearly all of the most massive galaxies lie in higher density regions. There is relatively little evolution in the mass-density relation over the $z = 0.05 - 0.9$ redshift range.

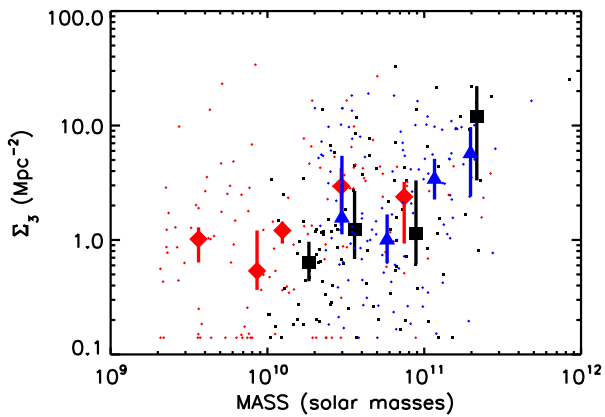


FIG. 60.— Σ_3 density parameter vs. stellar mass for the redshift intervals $z = 0.9 - 1.2$ (*blue triangles*), $z = 0.475 - 0.9$ (*black squares*), and $z = 0.3 - 0.475$ (*red diamonds*). In each case the large symbols show the median values for the mass intervals with 68% confidence limits.

While this relationship is well known in general terms, it is not easy to compare it precisely with other results, either because the environmental parameters are expressed in different ways, or because the increases are measured for optical luminosity rather than for mass (e.g., Croton et al. 2005; Hoyle et al. 2005; Cooper et al. 2007, 2008). However, Baldry et al. (2006) provide a local analysis of the galaxy masses using a similar environmental parameter. They characterize their Schechter function fits to the galaxy mass functions in different environments with the mass at which the contribution to the local galaxy mass density per dex in galaxy mass peaks. They show in their Figure 8d how this peak mass depends on Σ . We have measured this quantity for our $z = 0.6 - 1.2$ sample and show the result in Figure 61. In order to compare with Baldry et al. (2006) (*blue solid line*), we have adjusted their Kroupa masses to Salpeter masses, and we have matched their median Σ parameter to ours. We see from Figure 61 that the mass versus Σ_3 relation has a very similar slope at both redshifts but that the mass in a given environment is about 0.3 dex higher at $z = 0.9 - 1.2$ than it is now. This is expected, since the high-mass galaxies are already in place at the higher redshifts, while the low-mass galaxies are

still forming. However, it shows that this relative growth of the low-mass galaxies is occurring across our measured density range and is not a strong function of environment.

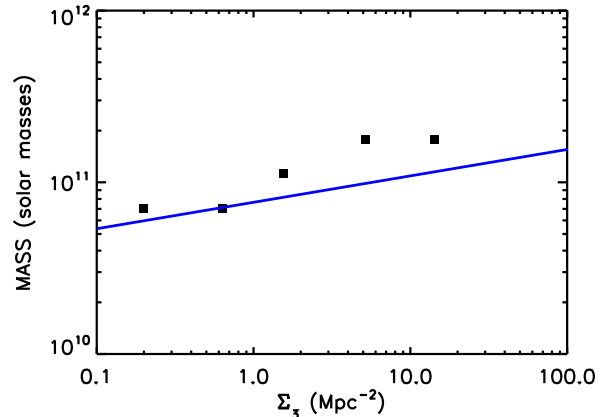


FIG. 61.— Mass at which contribution to the mass density per dex in galaxy mass peaks vs. Σ_3 density parameter. The black squares show the results from the present data in the $z = 0.9 - 1.2$ redshift interval. The blue line shows the corresponding local result derived by Baldry et al. (2006).

However, unlike the local analysis of Baldry et al. (2006), we do not see an environmental dependence for the distribution of galaxies between the blue cloud and the red sequence at $z = 0.6 - 1.2$. In Figure 62 we show the distribution of colors for galaxies with $z = 0.6 - 1.2$ separated by both mass and environment (*black histograms*). We compare this with the distribution of all galaxies in each mass interval (*green curves*) normalized to the number of galaxies in that particular sample (*number in upper right corner*). The blue histograms show sources detected at $24 \mu\text{m}$ which dominate the blue cloud at these masses, and the red histograms show sources which are not detected at $24 \mu\text{m}$ which dominate the red sequence. It can be seen that the distributions are essentially invariant with environment, while the fraction of red galaxies increases with mass. Thus, the environmental dependence of the red fraction seen in the local sample must have been imprinted over the $z = 0 - 1$ redshift interval. This suggests that the star formation switch-off may have been more rapid in the higher density environments.

11.9. Metal Evolution

We show the evolution of the metallicity-mass relation with redshift in Figure 63. In Figure 63a we compare the locally derived metallicity-mass relation of Tremonti04 (*black solid curve*) with our relations derived from the R23 method (using the Tremonti04 calibration) for $z = 0.05 - 0.475$ (*red*) and $z = 0.475 - 0.9$ (*cyan*). Since the Tremonti04 masses are computed for the Kroupa (2001) IMF, we had to increase them by a factor of 1.54 to make the comparison (see §1). As we have discussed in §1, the adopted IMF does not otherwise affect the results. We show both the polynomial fits to the metallicity-mass relations (*colored lines*) and the median values and errors in various mass bins (*symbols*).

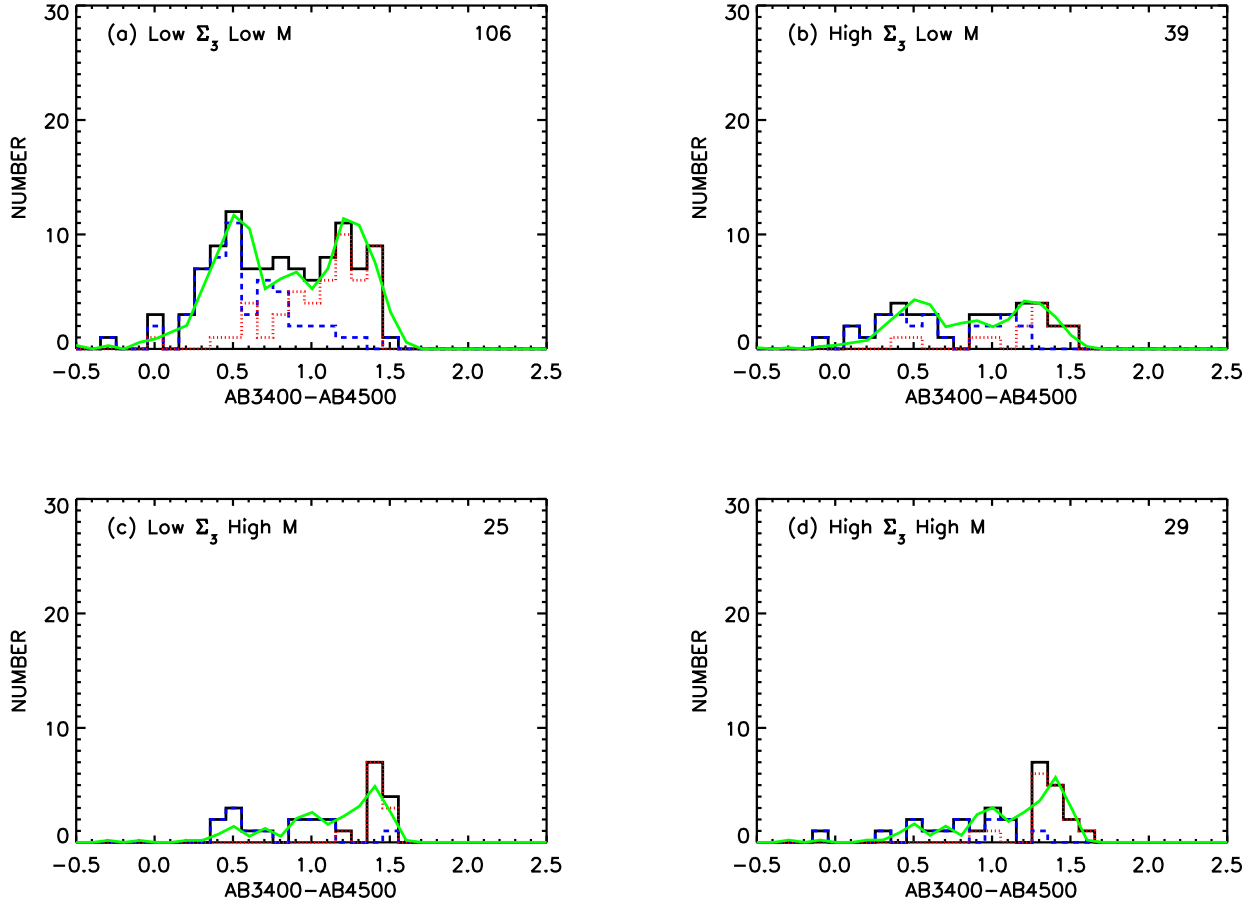


FIG. 62.— Distribution of the AB3400–AB4500 colors separated by both mass and environment for galaxies with $z = 0.6 - 1.2$ (*solid black histogram*). In (a) and (b) we show the distributions for the mass interval $2 \times 10^{10} - 10^{11} M_{\odot}$. In (c) and (d) we show the distributions for the mass interval $10^{11} - 10^{12} M_{\odot}$. (a) and (c) correspond to $\Sigma_3 < 1 \text{ Mpc}^{-2}$, and (b) and (d) correspond to Σ_3 greater than this value. The green curves show the distributions of all galaxies in the given mass interval normalized to the number of galaxies in that particular sample, which is shown in the upper right corner. The red (blue) histograms show the distribution of galaxies detected (undetected) at $24 \mu\text{m}$, respectively.

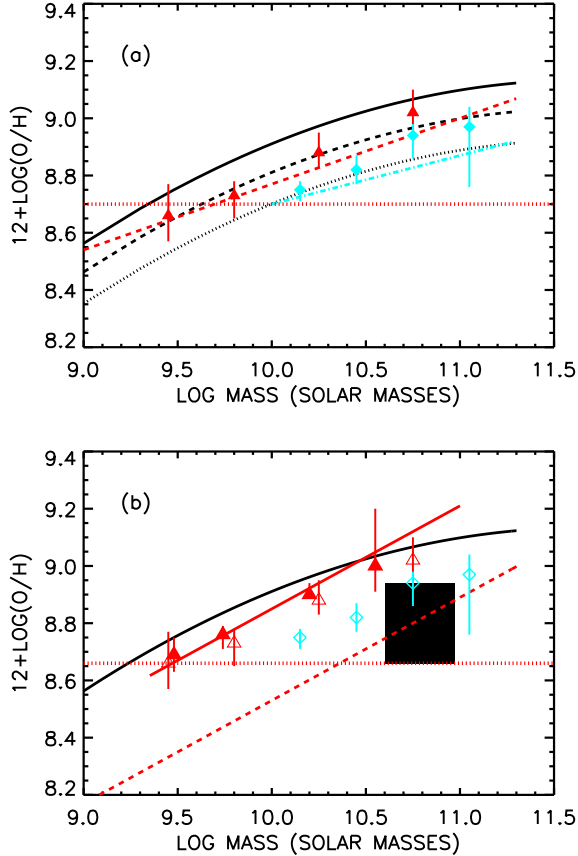


FIG. 63.— (a) Metallicity-mass relations in the $z = 0.05 - 0.475$ (red triangles) and $z = 0.475 - 0.9$ (cyan diamonds) redshift intervals derived from the R23 method using the Tremonti04 calibration and compared with Tremonti04’s local metallicity-mass relation (black curve). The colored lines show the polynomial fits to the individual data points. The solid symbols show the median values in the mass bins with 68% confidence limits. The medians lie slightly higher than the average values represented by the fits. The dotted red line shows the solar abundance. The black dashed (dotted) line shows the local relation reduced by 0.14 dex (0.22 dex) to match the data in the $z = 0.05 - 0.475$ ($z = 0.475 - 0.9$) interval. (b) Metallicity-mass relation in the $z = 0.05 - 0.475$ redshift interval (red solid line and solid triangles) computed using the $[\text{N II}]/\text{H}\alpha$ diagnostic and compared with the Shapley et al. (2004) measurements of the LBG sample computed using the same method (solid black region). The red dashed line shows the red solid line reduced by 0.32 dex to match the LBGs. The black curve, the red open triangles, and the cyan open diamonds are all taken from (a) and show the R23-based results.

We summarize the decrease in the metallicities with increasing redshift and decreasing mass in Table 3. In column 2 we give the average of the Tremonti04 values for galaxies in the given mass interval, and then in columns 3 and 4 we give the drop from Tremonti04 to each of our average values, respectively, for $z = 0.05 - 0.475$ and $z = 0.475 - 0.9$. The errors are 68% confidence limits.

The data are not adequate to determine if the shape of the local relation has changed with redshift. There are hints at the 2σ level that there is less evolution at the high-mass end, but within the accuracy that can be obtained with our data, the shape of the metallicity-mass relation over the observed mass range could be invariant from $z = 0.05 - 0.9$. However, if we normalize the local relation to our data at $z = 0.05 - 0.475$ (black dashed curve)

and at $z = 0.475 - 0.9$ (black dotted curve), then the best fits show that the metallicity in the $10^{10} - 10^{11} M_{\odot}$ interval is lower by 0.10 ± 0.04 dex than the local value at the median redshift of 0.44 (low-redshift interval) and lower by 0.21 ± 0.03 dex than the local value at the median redshift of 0.75 (high-redshift interval).

The conclusion that there is a decrease in the metallicity at a given mass with increasing redshift from $z = 0.05 - 0.9$ is consistent with previous work, though the precise values have varied considerably. The most recent work of Savaglio et al. (2005) gives a considerably larger change in the normalization and also finds a steeper slope at $z \sim 0.7$, namely $12 + \log(\text{O}/\text{H}) = 8.84 + (0.48 \pm 0.06) \log M_{10}$, which may be compared with our relation of $12 + \log(\text{O}/\text{H}) = 8.70 + (0.17 \pm 0.05) \log M_{10}$ (Eq. 16). The Savaglio et al. (2005) relation is fitted over a much wider mass range (down to masses below $10^9 M_{\odot}$) using a sample that is substantially incomplete and biased towards star formers at the lower masses. This weights the lower mass bins to lower metallicities and steepens the fit.

In Figure 63b we compare the median metallicities (red solid triangles) and the least-square polynomial fit (red solid line) computed from the $[\text{N II}]/\text{H}\alpha$ method in the $z = 0.05 - 0.475$ redshift interval with the $z \sim 2.1$ Lyman break galaxy (LBG) sample of Shapley et al. (2004), which was also computed using this diagnostic (black solid region). The R23-based measurements from Figure 63a are also shown (black curve and colored open symbols). The R23-based red open triangles for the same redshift interval are not significantly different than the $[\text{N II}]/\text{H}\alpha$ -based red solid triangles. The LBG galaxies lie about 0.32 dex lower (dashed red line) than the median $z = 0.44$ galaxies (red solid line) at the same mass and are similar in metallicity to local galaxies that are almost an order of magnitude lower in mass.

11.10. Gas Masses

In the simplest closed-box model for metal evolution, the metallicity $Z(\text{O})$ (the fraction by mass of O) in the gas is simply related to the oxygen yield $y(\text{O})$ by the well-known relation

$$Z(\text{O}) = y(\text{O}) \log(M_g/M_T), \quad (29)$$

where M_g is the gas mass and M_T is the sum of the gas mass and the stellar mass. The change in metallicity for a change in stellar mass is

$$\delta Z(\text{O}) = y(\text{O}) \delta M_{star}/M_g. \quad (30)$$

Thus, the derivative of $Z(\text{O})$ with respect to the stellar mass measures the quantity $y(\text{O})/M_g$, and, if we assume a value for the yield, we can derive the gas mass. Essentially we are measuring the gas reservoir required to dilute the metals returned from the known star formation to match the observed metal evolution.

The effective yields have been empirically measured for local galaxies and are found to be approximately independent of galaxy mass for masses above $10^{9.5} M_{\odot}$ (Garnett 2003). Tremonti04 find a weak dependence on mass in this mass range, but their results depend on using star formation as a proxy for gas mass. We will assume a time-independent and mass-independent value of $\log y(\text{O}) = -1.9$, which is probably a reasonable approximation given the uncertainties.

We roughly compute the gas reservoir mass densities using the mass change between $z = 0.05$ and $z = 0.77$ from the least-square fits of Equations 19–21 and the corresponding change in $Z(\text{O})$ from Table 1. For the lowest logarithmic mass interval $9.5 - 10 M_{\odot}$ we made the fit over $z = 0.05 - 0.44$, where the mass sample is complete. If the local mass density is lower than the Cole01 estimate this would reduce δM_{star} and hence the inferred gas mass. Deriving the values from the star formation instead gives broadly similar results, with the largest change being an increase by almost a factor of two in M_g in the logarithmic mass interval $10 - 10.5 M_{\odot}$.

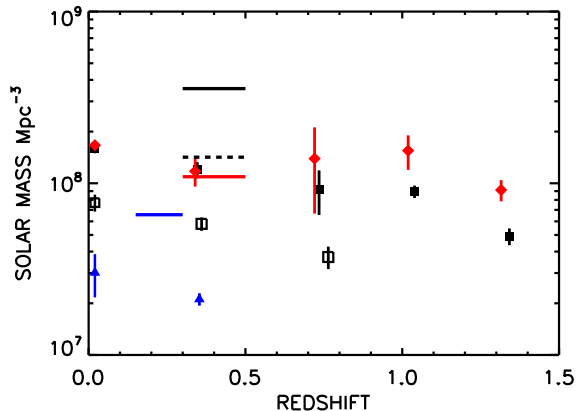


FIG. 64.— Mass density of the gas reservoirs inferred from the metal evolution compared with the stellar mass density history. The mass density of the gas reservoirs is shown with colored lines, and the stellar mass density history is shown with corresponding colored symbols in the mass intervals $10^{9.5} - 10^{10} M_{\odot}$ (blue line and triangles), $10^{10} - 10^{10.5} M_{\odot}$ (black dashed line and open squares), $10^{10.5} - 10^{11} M_{\odot}$ (black solid line and solid squares), and $10^{11} - 10^{11.5} M_{\odot}$ (red line and diamonds). The gas mass densities are computed over $z = 0.05 - 0.77$ for the higher mass intervals and over $z = 0.05 - 0.44$ for the lowest mass interval. The local mass densities for each of the mass intervals were obtained by integrating the Cole01 function.

We compare the gas mass densities (colored lines) with the stellar mass density history (corresponding colored symbols) for the mass intervals $10^{9.5} - 10^{10} M_{\odot}$ (blue line and triangles), $10^{10} - 10^{10.5} M_{\odot}$ (black dashed line and open squares), $10^{10.5} - 10^{11} M_{\odot}$ (black solid line and solid squares), and $10^{11} - 10^{11.5} M_{\odot}$ (red line and diamonds) in Figure 64. (The gas and stellar mass densities are derived using the Salpeter IMF and thus will change consistently if we use an alternate IMF.) In the highest mass interval (red) where the stellar mass is growing only slowly, the sum of the gas plus stellar mass densities at $z = 0.44$ is roughly comparable to the local stellar mass density obtained by integrating the Cole01 function. By contrast, the galaxies in the lower mass intervals where assembly is still progressing have much larger gas reservoirs. Thus, these results suggest that star formation is terminating as a consequence of gas depletion.

We estimate the total gas mass density over all galaxies larger than $10^{9.5} M_{\odot}$ at $z = 0.44$ to be $\sim 7 \times 10^8 M_{\odot} \text{ Mpc}^{-3}$. We can compare this with the current mass density in stars over the same mass range, namely $4.7 \times 10^8 M_{\odot} \text{ Mpc}^{-3}$ obtained by integrating Cole01. This suggests that there is still a significant amount of gas mass to be converted into stars. From Figure 64 we can see that

this principally lies in galaxies with masses below $10^{11} M_{\odot}$. We may very crudely infer that at the present time the highest mass galaxies will have very little gas mass remaining, while the lower mass galaxies will have comparable amounts of gas and stars. However, the uncertainties in this are very large, both from the observations and from the overly simple modeling.

12. SUMMARY

We have used a very large and highly spectroscopically complete galaxy sample selected by rest-frame NIR bolometric flux to conduct an integrated study of star formation and galactic stellar mass assembly from $z = 0.05 - 1.5$ and galactic metallicity evolution from $z = 0.05 - 0.9$. We summarize our results below.

- We constructed a rest-frame NIR ($0.8 - 2.4 \mu\text{m}$) bolometric flux sample in the GOODS-N field. We have spectroscopic redshifts and high-quality spectra for 77% of the galaxies in the sample, and we measured 13-band photometric redshifts for the remaining sources. Since most of the sources with only photometric redshifts lie outside of our two redshift ranges of interest, the spectroscopic completeness inside these ranges is extremely high ($> 91\%$ for $z = 0.05 - 0.9$ and $> 84\%$ for $z = 0.05 - 1.5$).

- We constructed four uniform NIR luminosity samples for our mass assembly analysis (two at lower redshifts, $z = 0.05 - 0.475$ and $z = 0.05 - 0.9$, which we also use for our metallicity analysis, and two at higher redshifts, $z = 0.9 - 1.2$ and $z = 1.2 - 1.5$) and fitted BC03 models (assuming a Salpeter IMF, a solar metallicity, and a Calzetti extinction law) to every galaxy to obtain galactic stellar masses and extinctions. We tested the extinctions by comparing the extinguished UV light, which is reradiated into the FIR, with the $24 \mu\text{m}$ light, which is a completely independent measure of the dust-reradiated light. We detected at $24 \mu\text{m}$ most of the sources with large reradiated fluxes, confirming the assignment of substantial extinctions. However, some of the $24 \mu\text{m}$ sources had low reradiated UV fluxes. To test whether we were failing to assign extinctions to these galaxies, we also measured, where possible, $f(\text{H}\alpha)/f(\text{H}\beta)$ for them. In all cases these Balmer ratio measurements were also consistent with little extinction.

- We adopted a maximum ratio of the stellar mass to the observed NIR luminosity of $10^{-33} M_{\odot}/\text{ergs s}^{-1}$. Multiplying the NIR luminosity limits of the four samples by this ratio, we found that the samples included all galaxies with masses above $2 \times 10^9 M_{\odot}$ ($z = 0.05 - 0.475$), $10^{10} M_{\odot}$ ($z = 0.05 - 0.9$), $2 \times 10^{10} M_{\odot}$ ($z = 0.9 - 1.2$), and $3 \times 10^{10} M_{\odot}$ ($z = 1.2 - 1.5$).

- For each galaxy spectrum we measured the equivalent widths of a standard set of lines. We found a strong trend to higher EWs at lower NIR luminosities. We also found a rapid drop in EWs at lower redshifts. We estimated a fixed offset of 1 \AA to correct the $\text{EW}(\text{H}\beta)$ for the effects of underlying stellar absorption, having found no strong dependence of the correction on galaxy type.

- We measured the line fluxes (calibrated by broadband fluxes) and the 4000 \AA break strengths in the galaxies. We measured the offsets between the rest-frame $3400 - 4500 \text{ \AA}$ magnitudes measured from the spectra and those measured from the photometry and found no dependence on

redshift. Thus, there are no relative errors in the photometric calibration of the UV and optical data.

- Although we can only measure Balmer ratio extinctions for our line fluxes using our lowest redshift sample, we found that when we compared these extinctions to the continuum extinctions that we obtained from our BC03 fits, the two were consistent, on average, within the errors. Thus, we can (and do) use the BC03 extinctions to deredden the line fluxes at higher redshifts.

- We calibrated the star formation diagnostics internally using our lowest redshift sample. We found that the UV flux had a somewhat tighter relation to the $H\alpha$ flux than the [O II] flux did and hence provided a better estimate of the SFR. We also saw this in the systematic dependence of the [O II] SFR on galaxy properties, such as the $H\alpha$ SFR of the galaxy and the galaxy mass. We adopted the UV SFR calibration as our primary calibration.

- Because it has become common in the literature to use 24 μm data to estimate SFRs, we also computed SFRs from our 24 μm fluxes and compared them with the reradiated SFRs that we determined from our UV luminosities. (The latter were obtained by taking the difference between the SFRs that we computed after correcting for extinction and the SFRs that we computed without making an extinction correction.) Although we found a substantial spread for the individual determinations, the two methods give good agreement when applied to the galaxy population as a whole.

- We constructed a number of emission line diagnostics for our $z = 0.05 - 0.475$ sample, since many of the spectra cover all of the emission lines from [O II] to [S II]. We dereddened all of the line fluxes using our BC03 extinctions. Adopting various calibrations from the literature, we derived metallicities from the N2O2, NH, and R23 diagnostic ratios, and we derived ionization parameters from the combination of O32, which has a dependence on q and metallicity, and N2O2 or R23. For $z = 0.475 - 0.9$ we could only compute R23 from the optical spectra. We compared the metallicity-mass relations that we derived from R23 for the two redshift intervals (restricting to masses above $10^{10} M_{\odot}$, where both samples are complete, and below $10^{11} M_{\odot}$) and found that, within the wide errors, the slopes were consistent. We also found that the median metallicity increased by 0.13 dex as the redshift decreased from median redshift 0.75 to median redshift 0.44.

- We determined that only about 20%–30% of the total galaxy mass density is included in our strong emission line metallicity analysis. We divided the remaining galaxies into an apparently passive category and a weakly active category. About 40% of the total galaxy mass density is contained in the passive population, and the majority of the massive galaxies ($> 10^{11} M_{\odot}$) fall into this category. Due to a lack of $H\beta$ and [O III] features in the stacked spectrum for the passive galaxies, there was no way we could use the gaseous emission to estimate metallicities. However, we were able to estimate metallicities from the stacked spectrum for the weakly active galaxies. As a check on how well we could do this, we also estimated metallicities from the stacked spectrum for the strong emission line galaxies. For $z = 0.05 - 0.475$ these estimates were in good agreement with the fit that we had made to the individual measurements, while for $z = 0.475 - 0.9$ they were about 0.1 dex higher on aver-

age. The metallicity estimates from the stacked spectrum for the weakly active galaxies showed substantial scatter but were in broad agreement with the strong emission line galaxies, so we subsequently assumed that they paralleled the evolution of the strong emission line galaxies.

- We constructed galactic stellar mass functions and compared them with the local mass function of Cole01. We found that the galaxy number densities at the low-mass end are still rising down to the lowest redshift interval, while the number densities at the high-mass end ($> 10^{11} M_{\odot}$) are changing much more slowly over $z = 0.05 - 1.5$. We provided parametric fits to the data by assuming a Schechter form for the mass functions. We found a significant evolution in the mean mass (a rise in either M_{*} or α with increasing redshift) due to the build-up of the low-mass region of the galactic stellar mass function relative to the high-mass region.

- We determined the mass density evolution by mass interval and compared them with the local mass densities obtained by integrating the Cole01 function over each mass interval. We found slow growth in the higher mass intervals and more rapid growth in the lower mass intervals. To quantify the results, we made least-square polynomial fits to the logarithmic stellar mass densities versus the logarithmic cosmic time. We found that the low-mass ranges ($< 10^{11} M_{\odot}$) are growing approximately linearly with time, while the high-mass ranges are growing more slowly.

- We computed the universal star formation history from $z = 0.05 - 1$ from our NIR sample. We calculated the SFRDs using our empirical calibrations and our extinction corrected $H\beta$ and UV luminosities. We found good agreement with the values derived from radio and submillimeter data. The SFRDs for the NIR sample drop steeply at lower redshifts, where most of the star formation is seen as direct UV emission from lower mass galaxies, which have very small extinctions. Thus, we also calculated the SFRDs from our extinction uncorrected data, which we found agreed well with rest-frame UV flux measurements of UV selected galaxies. Finally, to check our UV extinction corrections, we added the SFRDs that we computed from the 24 μm fluxes for the obscured star formation to the SFRDs that we computed from the extinction uncorrected [O II] luminosities for the unobscured star formation. This method has no dependence on the UV extinction corrections. Reassuringly, when we compared these SFRDs by mass interval with those calculated from the UV-based method, we found very similar results.

- We compared the expected formed stellar mass density growth rates produced by star formation (computed with the conservation equation using both the UV-based and the 24 μm + [O II]-based SFRDs) with those measured from the formed stellar mass functions. Here the formed stellar mass density is the total mass density formed into stars prior to stellar mass loss. We found amazing agreement over a wide range of redshifts and masses, though there is a slight normalization difference between the two measurements (the measurements based on the star formation are higher). We explored various possibilities to explain the offset, and we concluded that the most likely explanation is that we need an IMF which is more heavily weighted to mid-mass stars than the Salpeter, Kroupa, and Chabrier IMFs. Over the $1 - 100 M_{\odot}$ range, a bro-

ken power law with an index of -1.10 below $10 M_{\odot}$ and -1.60 above works well. This is well within the range of uncertainty in the high-mass IMF and may be favored for other reasons (Fardal et al. 2007).

- We obtained a quantitative description of the range of behaviors in the galaxies by computing the instantaneous SSFRs. There is a wide spread in the SSFRs at all redshifts and masses. However, from the mean SSFRs we found that, on average, only galaxies with masses $\lesssim 10^{11} M_{\odot}$ grow significantly in any of the redshift intervals. In the lowest redshift interval where we can measure the masses below $10^{10} M_{\odot}$, we finally saw the flattening of the SSFRs (at a high level). From the distribution functions of the SSFRs by mass interval, we concluded that what star formation is occurring in the galaxies in the $10^{11} - 10^{11.5} M_{\odot}$ interval is spread over many galaxies, and there are very few galaxies in this mass interval that are undergoing significant growth. In contrast, in the $10^{10} - 10^{10.5} M_{\odot}$ interval a substantial number of galaxies have SSFRs that, if maintained over the time frame, would change their mass significantly.

- We examined the rest-frame UV–blue (AB3400–AB4500) colors uncorrected for extinction for our NIR sample and found almost no evolution with redshift and a uniform spread of colors stretching from the blue cloud to the red sequence. Nearly all of the galaxies in the intermediate color range (sometimes referred to as the green valley) are $24 \mu\text{m}$ sources. After correcting for extinction, we found that the bulk of the $24 \mu\text{m}$ sources lie in the blue cloud. We also then saw a more clearly bimodal distribution in the total sample. Applying extinction corrections is critical when analyzing the galaxy colors, since many of the sources seen in the green valley and the red sequence prior to correcting for extinction are dusty sources with intrinsically blue colors. In contrast to literature results from optically-selected and extinction uncorrected data, we saw no change in the position of the red sequence with redshift in our extinction corrected data. Thus, the intrinsic colors of the reddest galaxies are not changing over $z = 0.05 - 1.5$.

- We approximately separated the red sequence from the blue cloud using a cut 0.25 mag below the red sequence. We also separated the red sequence from the blue cloud using the $\text{EW}([\text{O II}])$, which is independent of the extinction correction, and the 4000 \AA break strength, which is nearly independent. Although we found comparable amounts of mass in the red sequence and the blue cloud, the growth in the mass density is primarily occurring in the red sequence galaxies with masses $10^{10.5} - 10^{11} M_{\odot}$.

- We investigated how star formation is occurring us-

ing the extinction corrected rest-frame AB3400–AB8140 colors and the rest-frame $\text{EW}(\text{H}\beta)$. The $\text{EW}(\text{H}\beta)$ is produced by higher mass stars and thus fades more rapidly, providing a well-known age signature. We compared the data with some evolutionary tracks from the BC03 models and found consistency with episodic star formation in all but the lowest mass ($10^{10} - 10^{10.5} M_{\odot}$) galaxies, where there may be a mixture of smooth and episodic star formation. It appears that the burst process results in the dusty galaxies producing the $24 \mu\text{m}$ emission.

- We compared the morphological types with the spectral characteristics of the galaxies. We found no change in the distribution of the morphological types in the 4000 \AA break- $\text{EW}(\text{H}\beta)$ plane over $z = 0.05 - 0.9$. We confirmed a strong correlation between the galaxy morphology and the galaxy mass, with many of the most massive galaxies being E/S0 galaxies. We saw very little change in the mass function of the strong emitters and spiral galaxies. Instead we saw the mass build-up primarily occurring in the passive and weakly active E/S0 galaxies. We concluded that galaxies are moving from spiral galaxy types to E/S0 types with decreasing redshift and that the decrease in the mass of the blue cloud from this effect offsets the growth due to star formation.

- We found that massive galaxies ($> 10^{11} M_{\odot}$) preferentially occur in higher density environments, but below this mass we saw relatively little dependence on the environment. We also found relatively little evolution in this mass-density relation over the $z = 0.05 - 0.9$ redshift range.

- We found that the metallicities of galaxies are increasing with decreasing redshift at all galaxy masses over $z = 0 - 0.9$. The increase is 0.21 ± 0.03 dex between $z = 0.75$ and $z = 0$. We compared this with the metal release rate from star formation to make a crude estimate of the gas mass reservoirs in the galaxies using a simple closed box model. We found that for mass intervals below $10^{11} M_{\odot}$, where assembly is still progressing, the gas reservoirs are larger than are needed to assemble the present-day stellar mass densities.

We thank J. S. Gallagher for interesting conversations and a critical reading of the paper. We also thank the anonymous referee for an extremely helpful report with many useful suggestions for improving the paper. We gratefully acknowledge support from NSF grants AST 0407374 and AST 0709356 (L. L. C.) and AST 0239425 and AST 0708793 (A. J. B.), the University of Wisconsin Research Committee with funds granted by the Wisconsin Alumni Research Foundation (A. J. B.), and the David and Lucile Packard Foundation (A. J. B.).

REFERENCES

- Alexander, D. M., et al. 2003, *AJ*, 126, 539
 Asplund, M., Grevesse, N., Sauval, A. J., Allende Prieto, C., & Kiselman, D. 2004, *A&A*, 417, 751
 Baldry, I. K., & Glazebrook, K. 2003, *ApJ*, 593, 258
 Baldry, I. K., Balogh, M. L., Bower, R. G., Glazebrook, K., Nichol, R. C., Bamford, S. P., & Budavari, T. 2006, *MNRAS*, 373, 469
 Baldry, I. K., Glazebrook, K., Brinkmann, J., Ivezić, Z., Lupton, R. H., Nichol, R. C., & Szalay, A. S. 2004, *ApJ*, 600, 681
 Barbaro, G., & Poggianti, B. M. 1997, *A&A*, 324, 490
 Barger, A. J., Cowie, L. L., Mushotzky, R. F., Yang, Y., Wang, W.-H., Steffen, A. T., & Capak, P. 2005, *AJ*, 129, 578
 Barger, A. J., Cowie, L. L., & Richards, E. A. 2000, *AJ*, 119, 2092
 Barger, A. J., Cowie, L. L., & Wang, W.-H. 2007, *ApJ*, 654, 764
 Bauer, A., Drory, N., Hill, G. J., and Feulner, G. 2005, *ApJ*, 621, L89
 Bauer, F. E., et al. 2002, *AJ*, 123, 1163
 Bell, E. F., McIntosh, D. H., Katz, N., & Weinberg, M. D. 2003, *ApJS*, 149, 289
 Bell, E. F., et al. 2004, *ApJ*, 608, 752
 Bell, E. F., et al. 2005, *ApJ*, 625, 23
 Bell, E. F., Zheng, X. Z., Papovich, C., Borch, A., Wolf, C., & Meisenheimer, K. 2007, *ApJ*, 663, 834
 Borch, A., et al. 2006, *A&A*, 453, 869
 Brinchmann, J., & Ellis, R. S. 2000, *ApJ*, 536, L77
 Brinchmann, J., et al. 2004, *MNRAS*, 351, 1151
 Bruzual, G., & Charlot, S. 2003, *MNRAS*, 344, 1000 (BC03)

- Bruzual, G. 2007, in Proc. IAU Symposium No. 241, Eds. A. Vazdekis and R. Peletier, (Cambridge: CUP) arXiv:astro-ph/0703052
- Bundy, K., Ellis, R. S., & Conselice, C. J. 2005, ApJ, 625, 621
- Bundy, K., et al. 2006, ApJ, 651, 120
- Calzetti, D., Armus, L., Bohlin, R. C., Kinney, A. L., Koornneef, J., & Storchi-Bergmann, T. 2000, ApJ, 533, 682
- Capak, P., et al. 2004, AJ, 127, 180
- Chabrier, G. 2003, ApJ, 586, L133
- Chapman, S. C., Blain, A. W., Smail, I., & Ivison, R. J. 2005, ApJ, 622, 772
- Chapman, S. C., Smail, I., Blain, A. W., & Ivison, R. J. 2004, ApJ, 614, 671
- Cohen, J. G., Cowie, L. L., Hogg, D. W., Songaila, A., Blandford, R., Hu, E. M., & Shopbell, P. 1996, ApJ, 471, L5
- Cohen, J. G., Hogg, D. W., Blandford, R., Cowie, L. L., Hu, E., Songaila, A., Shopbell, P., & Richberg, K. 2000, ApJ, 538, 29
- Cole, S., et al. 2001, MNRAS, 326, 255 (Cole01)
- Conselice, C. J., Blackburne, J. A., & Papovich, C. 2005, ApJ, 620, 564
- Conselice, C. J., et al. 2007, MNRAS, 381, 962 (Conselice07)
- Cooper, M. C., Newman, J. A., Madgwick, D. S., Gerke, B. F., Yan, R., & Davis, M. 2005, ApJ, 634, 833
- Cooper, M. C., et al. 2007, MNRAS, 376, 1445
- Cooper, M. C., et al. 2008, MNRAS, 383, 1058
- Cowie, L. L., Barger, A. J., Hu, E. M., Capak, P., & Songaila, A. 2004, AJ, 127, 3137
- Cowie, L. L., Hu, E. M., & Songaila, A. 1995, Nature, 377, 603
- Cowie, L. L., Songaila, A., Hu, E. M., & Cohen, J. G. 1996, AJ, 112, 839
- Croton, D. J., et al. 2005, MNRAS, 356, 1155
- Dale, D. A., & Helou, G. 2002, ApJ, 576, 159
- Dale, D. A., et al. 2005, ApJ, 633, 857
- Davis, M., et al. 2003, Proc. SPIE, 4834, 161
- Dickinson, M., Papovich, C., Ferguson, H. C., & Budavári, T. 2003, ApJ, 587, 25
- Dressler, A. 1980, ApJ, 236, 351
- Drory, N., Bender, R., Feulner, G., Hopp, U., Maraston, C., Snigula, J., & Hill, G. J. 2004, ApJ, 608, 742
- Drory, N., Salvato, M., Gabasch, A., Bender, R., Hopp, U., Feulner, G., & Pannella, M. 2005, ApJ, 619, L131
- Eke, V. R., Baugh, C. M., Cole, S., Frenk, C. S., King, H. M., & Peacock, J. A. 2005, MNRAS, 362, 1233
- Elsner, F., Feulner, G., & Hopp, U. 2008, A&A, 477, 503
- Faber, S. M., et al. 2003, Proc. SPIE, 4841, 1657
- Fardal, M. A., Katz, N., Weinberg, D. H., & Davé, R. 2007, MNRAS, 379, 985
- Felten, J. 1976, ApJ, 207, 700
- Fontana, A., et al. 2003, ApJ, 594, L9
- Fontana, A., et al. 2004, A&A, 424, 23
- Fontana, A., et al. 2006, A&A, 459, 745 (Fontana06)
- Giallongo, E., Salimbeni, S., Menci, N., Zamorani, G., Fontana, A., Dickinson, M., Cristiani, S., & Pozzetti, L. 2005, ApJ, 622, 116
- Giavalisco, M., et al. 2004, ApJ, 600, L93
- Haarsma, D. B., Partridge, R. B., Windhorst, R. A., & Richards, E. A. 2000, ApJ, 544, 641
- Hopkins, A. M., & Beacom 2006, ApJ, 651, 142
- Hopkins, A. M., et al. 2003, ApJ, 599, 971
- Hoyle, F., Rojas, R. R., Vogeley, M. S., & Brinkmann, J. 2005, ApJ, 620, 618
- Kannappan, S. J., & Gawiser, E. 2007, ApJ, 657, L5
- Kauffmann, G., White, S. D. M., Heckman, T. M., Ménard, B., Brinchmann, J., Charlot, S., Tremonti, C., & Brinkmann, J. 2004, MNRAS, 353, 713
- Kauffmann, G., et al. 2003a, MNRAS, 341, 33
- Kauffmann, G., et al. 2003b, MNRAS, 341, 54
- Kennicutt, R. C., Jr. 1998, ARA&A, 36, 189
- Kewley, L. J., & Dopita, M. A. 2002, ApJS, 142, 35 (KD02)
- Kewley, L. J., Geller, M. J., & Jansen, R. A. 2004, AJ, 127, 2002
- Kinney, A. L., Calzetti, D., Bica, E., & Storchi-Bergmann, T. 1994, ApJ, 429, 172
- Kobulnicky, H. A., Kennicutt, R. C., Pizagno, J. L. 1999, ApJ, 514, 544
- Kobulnicky, H. A., & Kewley, L. J. 2004, ApJ, 617, 240 (KK04)
- Kobulnicky, H. A., & Phillips, A. C. 2003, ApJ, 599, 1031
- Kobulnicky, H. A., et al. 2003, ApJ, 599, 1006
- Kroupa, P. 2001, MNRAS, 323, 331
- Le Floch, Emeric, et al. 2005, ApJ, 632, 169
- Liang, Y. C., Hammer, F., & Flores, H. 2006, A&A, 447, 113
- Lilly, S. J., Carollo, C. M., & Stockton, A. N. 2003, ApJ, 597, 730
- Lilly, S. J., Le Fèvre, O., Hammer, F., & Crampton, D. 1996, ApJ, 460, L1
- Madau, P., Ferguson, H. C., Dickinson, M. E., Giavalisco, M., Steidel, C. C., & Fruchter, A. 1996, MNRAS, 283, 1388
- Maraston, C. 2005, MNRAS, 362, 799
- Marcillac, D., Elbaz, D., Chary, R. R., Dickinson, M., Galliano, F., & Morrison, G. 2006, A&A, 451, 57
- McGaugh, S. 1991, ApJ, 380, 140
- Mouhcine, M., Lewis, I., Jones, B., Lamareille, F., Maddox, S. J., & Contini, T. 2005, MNRAS, 362, 1143
- Moustakas, J., Kennicutt, R. C., Jr., & Tremonti, C. A. 2006, ApJ, 642, 775
- Noeske, K. G., et al. 2007, ApJ, 660, L43
- Oke, J. B., et al. 1995, PASP, 107, 375
- Osterbrock, D. E. 1989, Astrophysics of Gaseous Nebulae and Active Galactic Nuclei (Mill Valley, CA: Univ. Sci. Books)
- Pagel, B. E. J., Edmunds, M. G., Blackwell, D. E., Chun, M. S., & Smith, G. 1979, MNRAS, 189, 95
- Pannella, M., Hopp, U., Saglia, R. P., Bender, R., Drory, N., Salvato, M., Gabasch, A., & Feulner, G. 2006, ApJ, 639, L1
- Papovich, C., et al. 2006, ApJ, 640, 92
- Pérez-González, P. G., Gallego, J., Zamorano, J., Alonso-Herrero, A., Gil de Paz, A., & Aragón-Salamanca, A. 2003, ApJ, 587, L27
- Pérez-González, P. G., et al. 2005, ApJ, 630, 82
- Pérez-González, P. G., et al. 2008, ApJ, 675, 234
- Reddy, N. A., Steidel, C. C., Erb, D. K., Shapley, A. E., & Pettini, M. 2006, ApJ, 653, 1004
- Reddy, N. A., Steidel, C. C., Pettini, M., Adelberger, K. L., Shapley, A. E., Erb, D. K., & Dickinson, M. 2008, ApJS, 175, 48
- Richards, E. A. 2000, ApJ, 633, 611
- Rosa-González, D., Terlevich, E., & Terlevich, R. 2002, MNRAS, 332, 283
- Rudnick, G., et al. 2003, ApJ, 599, 847
- Rudnick, G., et al. 2006, ApJ, 650, 624
- Salpeter, E., 1955, ApJ, 121, 161
- Savaglio, S., et al. 2005, ApJ, 635, 260
- Sandage, A., Tammann, G. A., & Yahil, A. 1979, ApJ, 172, 253 (STY)
- Schechter, P. 1976, ApJ, 203, 297
- Schiminovich, D., et al. 2005, ApJ, 619, L47
- Shapley, A. E., Erb, D. K., Pettini, M., Steidel, C. C., & Adelberger, K. L. 2004, ApJ, 612, 108
- Silva, L., Granato, G. L., Bressan, A., & Danese, L. 1998, ApJ, 509, 103
- Somerville, R. S., Lee, K., Ferguson, H. C., Gardner, J. P., Moustakas, L. A., & Giavalisco, M. 2004, ApJ, 600, 171
- Steidel, C. C., Adelberger, K. L., Giavalisco, M., Dickinson, M., & Pettini, M. 1999, ApJ, 519, 1
- Strateva, I., et al. 2001, AJ, 122, 1861
- Swinbank, A. M., Smail, I., Chapman, S. C., Blain, A. W., Ivison, R. J., & Keel, W. C. 2004, ApJ, 617, 64
- Tremonti, C. A., et al. 2004, ApJ, 613, 898 (Tremonti04)
- Treu, T., et al. 2005, ApJ, 633, 174 (Treu05)
- van der Wel, A., et al. 2007, ApJ, 670, 206
- van Dokkum, P. G., Franx, M., Fabricant, D., Illingworth, G. D., & Kelson, D. D. 2000, ApJ, 541, 95
- Wang, W.-H., Cowie, L. L., & Barger, A. J. 2006, ApJ, 647, 74
- Weiner, B. J., et al. 2005, ApJ, 620, 595
- Willmer, C. N. A., et al. (2006), ApJ, 647, 853
- Wilson, G., Cowie, L. L., Barger, A. J., & Burke, D. J. 2002, AJ, 124, 1258
- Wirth, G. D., et al. 2004, AJ, 127, 3121
- Wyder, T. K., et al. 2005, ApJ, 619, L15

TABLE 1
SCHECHTER FUNCTION FITS

Redshift Interval	$\alpha(z)$	$\text{Log } M_*(z)$ (M_\odot)	$\text{Log } \phi_*(z)$ (Mpc^{-3})	$\text{Log } M_*(z)$ ($\alpha = -1.18$) (M_\odot)
Local ^a	-1.18 ± 0.03	11.16 ± 0.01	-2.51 ± 0.06	11.16 ± 0.1
0.05 – 0.475	$-1.10(-0.88, -1.30)$	10.93(10.71, 11.25)	-2.63 ± 0.08	11.02(10.85, 11.21)
0.475 – 0.9	$-0.94(-0.70, -1.16)$	11.08(10.93, 11.26)	-2.60 ± 0.10	11.24(11.14, 11.35)
0.9 – 1.5	$-0.56(-0.08, -0.98)$	11.02(10.87, 11.20)	-2.63 ± 0.04	11.28(11.19, 11.38)

^aCole et al. (2001)

TABLE 2
PERCENTAGES OF STRONG STAR FORMERS

Logarithmic Mass Interval (M_\odot)	Per Redshift Interval (%)		
	$z = 0.9 - 1.5$	$z = 0.475 - 0.9$	$z = 0.05 - 0.475$
10 – 10.5	...	55 ± 5	67 ± 11
10.5 – 11	41 ± 4	29 ± 4	32 ± 12
11 – 11.5	15 ± 4	$8(4 - 12)^a$	$10(0 - 33)^a$

^aParentheses show the 68% confidence limits.

TABLE 3
R23 METALLICITY EVOLUTION

Logarithmic Mass Interval	Tremonti04	$z = 0.05 - 0.475$	$z = 0.475 - 0.9$
9.30 – 9.75	8.77	-0.10 ± 0.08	...
9.75 – 10.25	8.91	-0.10 ± 0.07	-0.21 ± 0.04
10.25 – 10.75	9.02	-0.07 ± 0.10	-0.20 ± 0.04
10.75 – 11.25	9.10	...	-0.12 ± 0.05